Tracing Physicochemical and Structural Changes in Drug Delivery Systems and Human Cells by Confocal Raman Microscopy

Dissertation

zur Erlangung des Grades
des Doktors der Naturwissenschaften
der Naturwissenschaftlich-Technischen Fakultät
der Universität des Saarlandes

von

Branko Vukosavljević

Saarbrücken

2018

Tag des Kolloquiums: 24. April 2018

Dekan: Prof. Dr. Guido Kickelbick

Berichterstatter: Prof. Dr. Maike Windbergs

     Prof. Dr. Gregor Jung

Vorsitz: Prof. Dr. Claus-Michael Lehr

Akademischer Mitarbeiter: Dr. Stefan Böttcher

Мом драгом Тати,

уз вечну захвалност што је веровао у мене
и научио ме како да се радујем

Table of Contents

I   Summary

The advances in drug delivery research regarding formulation strategies and technologies, and at the same time high regulatory demands for novel therapeutics, in turn require advanced analytical methods for their investigation. In this work, confocal Raman microscopy is successfully applied as a label-free, chemically selective and non-destructive method for in-depth analysis to gain insight into complex drug carrier systems, to understand cellular and non-cellular barriers in the human body, as well as to visualize drug and carrier uptake. The studies include examination of pellets and tablets, designed for controlled drug release, elucidation of mass transport mechanisms and in situ drug recrystallization upon drug release. Furthermore, the polymer distribution within bio-inspired polymeric fiber mats was visualized and successfully correlated to interactions of the fibers with human cells. Moreover, confocal Raman microscopy was used for investigation of human airway mucus microstructure, and for tracing molecular and structural changes upon chemical mucolysis. Further, the alveolar surfactant, was examined upon differentiation of primary epithelial lung cells utilizing both, linear and coherent Raman techniques. Finally, particle uptake into cells with different membrane properties was investigated by label-free intracellular trafficking of bioinspired therapeutics for targeted drug delivery. Altogether, this newly gained knowledge will help further advancement in drug delivery research beyond the current state-of-the-art.

II   Zusammenfassung

Die Fortschritte in der Entwicklung von Wirkstofftransporter-Systemen, insbesondere bezüglich neuerer Formulierungsstrategien und -technologien, und die hohen regulatorischen Anforderungen für neue Therapeutika erfordern hochentwickelte analytische Methoden für deren Untersuchungen. Im Rahmen dieser Arbeit wurde konfokale Raman Mikroskopie erfolgreich als eine markierungsfreie, chemisch selektive und nicht-destruktive Methode für eine detaillierte Analyse verwendet, um einen Einblick in komplexe Wirkstoffträgersysteme zu gewinnen, zelluläre und nicht-zelluläre menschliche Barrieren im menschlichen Körper zu verstehen, sowie Arzneistoffe und Partikel zu visualisieren. Die Studien umfassen Untersuchungen von Pellets und Tabletten für die kontrollierte Wirkstofffreigabe, erklären den Massentransportmechanismus und die *in situ* Wirkstoffrekristallisation nach Wirkstofffreisetzung. Darüber hinaus konnte die Polymerverteilungen innerhalb bio-inspirierter, elektrogesponnener Vliese visualisiert und deren Interaktion mit den menschlichen Zellen korreliert werden. Außerdem konnte die konfokale Raman-Mikroskopie für die Untersuchung der Mikrostruktur von Mukus aus den humanen Atemwegen und zur Verfolgung molekularer und struktureller Veränderungen nach chemischer Mukolyse eingesetzt werden. Mit Hilfe linearer und kohärenter Ramantechniken konnte zudem das alveolare Surfactant während der Differenzierung primärer epithelialer Lungenzellen untersucht werden. Letztlich wurde die Aufnahme von Partikeln in Zellen mit unterschiedlichen Membraneigenschaften mittels markierungsfreier, intrazellulärer Nachverfolgung von bio-inspirierten Therapeutika für die zielgerichtete Arzneistoffapplikation analysiert. Das hier neugewonnene Wissen erlaubt somit weitere Fortschritte in der Forschung des Wirkstofftransports jenseits des aktuellen Wissensstandes.

III   Abbreviations

AFM	atomic force microscopy
API	active pharmaceutical ingredient
CARS	coherent anti-Stokes Raman scattering
CRM	confocal Raman microscopy
DPI	dry powder for inhalation
ERL	Eudragit RL
FU	fluorouracil
IR	infrared
MCC	microcrystalline cellulose
MIR	mid infrared
NIR	near infrared
PAT	process analytical technology
PCL	poly(ε-caprolactone)
PLGA	poly(lactic-co-glycolic acid)
PVP	polyvinylpyrrolidone
PVP-VA	polyvinylpyrrolidone/vinyl acetate
QbD	Quality by Design
SEDDS	self-emulsifying drug delivery systems
SEM	scanning electron microscopy
SERS	surface enhanced Raman scattering
SRS	stimulated Raman scattering
TERS	tip-enhanced Raman scattering
UV	ultraviolet

1   Introduction

The constant advancement in formulation strategies and technologies applied in drug delivery research regularly necessitates cutting-edge analytical tools for versatile and comprehensive investigation of component distribution, drug release and/or degradation of novel therapeutics, as well their interaction with cells and tissues. In this context, confocal Raman microscopy represents a sophisticated analytical approach since it allows for label-free, chemically selective and non-destructive analysis.

1.1   Raman Effect

Upon interaction of light with matter, three characteristic phenomena may occur: transmission, absorption, and scattering, the latter being the most infrequent among the other effects, since it is a result of an inelastic collision of a photon with a molecule (Fig. 1A). This effect is described as Stokes scattering if the scattered photons loose energy, and anti-Stokes scattering if, in the rare case, the scattered photons gain energy. More precisely, Stokes scattering is detected at lower frequency (lower energy) and anti-Stokes scattering at higher frequency (higher energy) compared to the incoming photons. In the case of elastic scattering however, the scattered photons stay at the original vibrational level, retaining the same energy (so called Rayleigh scattering). Raman scattering is an inelastic scattering process in which vibrational modes in molecules are excited by the interaction with the incident light (1). A schematic illustration of the energy levels of incoming and outgoing photons for the different scattering effects is depicted in Fig. 1B. In this thesis, we used both, Stokes and anti-Stokes scattering phenomena for analytical investigation and they will be compared in the following chapters.
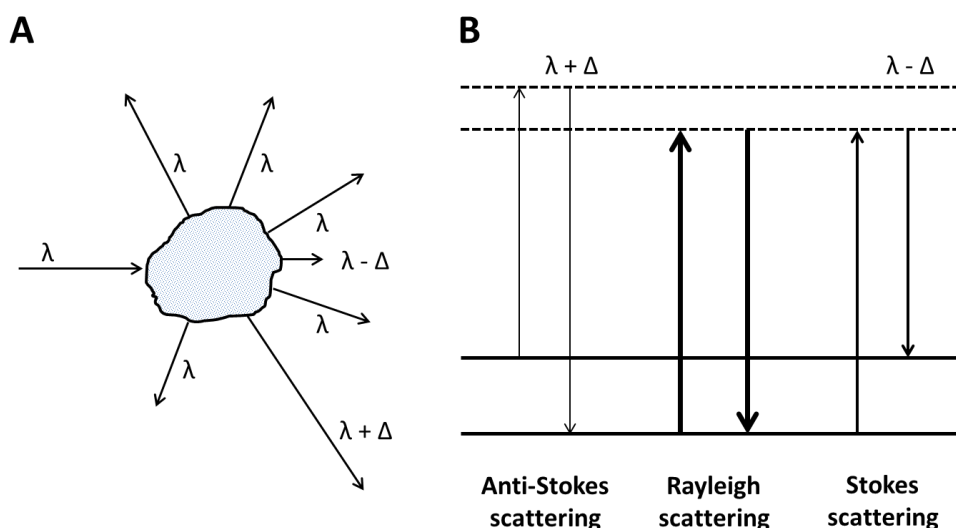
Figure 1. A. Schematic illustration of light scattering occurring upon interaction of light and matter. The major fraction of incident light is scattered elastically (λ). A small portion of the incident light however, is scattered inelastically ($\lambda \pm \Delta$); B. Energy level diagram illustrating anti-Stokes, Rayleigh and Stokes scattering; line thickness corresponds with the probability of appearance.

When the excitation frequency changes, the frequency of Raman scattered light is also changing. In order to track those wavelength changes between incident and scattered light, monochromatic laser

light is used to obtain a Raman scattering signal from a sample. The energy difference between the excitation frequency and the frequency of the Raman scattered light is a constant attribute for a given Raman band. Consequently, a Raman spectrum (Fig. 2) represents a plot of the scattered intensity versus the energy difference between the incident and scattered photons ("Raman shift").
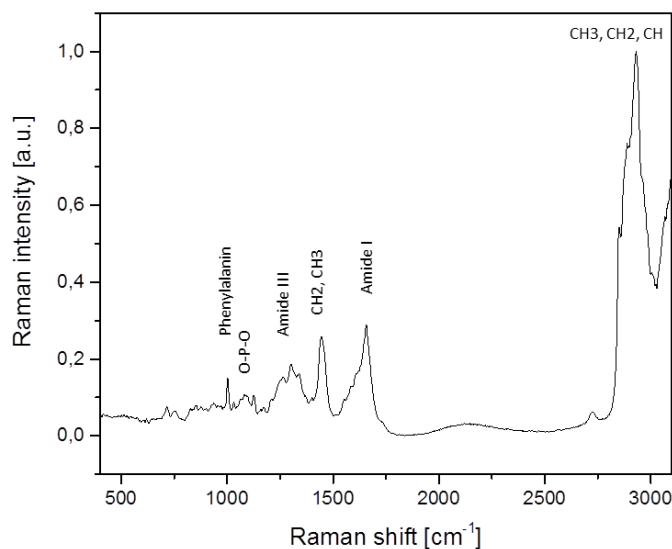
Figure 2. A Raman spectrum of a human cell composed of spectral contributions from proteins, nucleic acids and lipids.

The Raman shift is characteristic for molecular vibrations representing specific molecular functional groups. Consequently, the Raman scattering pattern is specific for a particular chemical structure and resembles a specific "molecular fingerprint". Based on their composition, Raman spectra of cells for example (Fig. 2), usually consist of spectral contributions from proteins (phenylalanine, amide I, amide II, CH, CH_2 and CH_3 vibrations), nucleic acids (O-P-O vibrations) and lipids (CH, CH_2 and CH_3 vibrations) (2). Furthermore, the count of scattered photons at a defined Raman shift and therefore the signal intensity linearly correlates with the quantity of the represented molecule.

The position of a line in the Raman spectrum corresponds to the energy that is required to excite a molecule to a certain vibrational energy level. A molecule can have up to 3N-6 independent vibrational modes (3N-5 for linear molecules), where N is the number of atoms in the molecule. Molecular vibrations are often classified into groups that are intuitively descriptive of the vibrational motion. An oscillation in bond length is called a "stretch", an oscillation in bond angle is called a "deformation" or "bend", etc.

Raman scattering measures vibrational transition energies from about 17 to 4000 cm^{-1}, which is nearly equivalent to the entire spectral ranges covered by far- and mid-infrared spectroscopy together. In contrast to other vibrational spectroscopy methods, Raman excitation frequencies can range from the ultraviolet (UV) to the near-infrared region (NIR), thus making the technique very flexible.

1.2   Spontaneous Raman Scattering

The quantum mechanical model for Raman scattering was first described by Placzek (3). He discusses several aspects of Raman scattering that are of practical importance for chemical imaging. First of all, the intensity of Raman scattering is proportional to the excitation intensity. However, there is a practical limitation for this phenomenon, since strong monochromatic lasers can overheat and damage the sample. Furthermore, the intensity of Raman scattering is proportional to the number of scattering molecules and to the fourth power of the Raman photon frequency. Moreover, Raman sensitivity increases quickly with increasing excitation frequency (decreasing wavelength) because the Raman photon frequency increases along with it. Placzek's complicated quantum mechanical model can be rewritten in an analytically useful form similar to Beer's law:

$$I_R = (I_L \, \sigma_R \, X)PC \qquad\qquad \text{(Equation 1)}$$

where I_R is the measured Raman intensity, I_L is the laser intensity, σ_R is the absolute Raman cross section, X is the experimental constant, P is the sample path length, and C is the concentration.

Here, characteristics of detectors and optics properties are represented by the experimental constant X, and the strength of a Raman band by the Raman cross section.

The sensitivity of spontaneous Raman scattering represents one of the biggest obstacles for Raman spectroscopy as an analytical tool, especially when analyzing cells, tissues, or biological samples in general. Furthermore, for simultaneous detection of cells and a drug to investigate their interactions, a significant spectral contrast is required for identification. When dealing with small concentrations of the drug or bioinspired chemical entities, such as peptide drugs or nucleoside analogues, this is in many cases hardly possible. Thus, chemical structures such as alkyne or isotopes deuterium have gained considerable attention as their scattering can be detected in the spectral "silent region" (between 1800 – 2800 cm^{-1}), in which no significant spectral contributions of other biomacromolecules are observed. In contrast to often bulky fluorescence marker molecules, deuterium can be introduced into a molecule without significantly changing its physicochemical characteristics (4-8).

Another obstacle often happening upon detection of Raman scattering and quantitative analysis is sample noise. Noise is any detected signal which can hinder the detection of the measured analyte. The most serious noise source in Raman spectroscopy is fluorescence, which (due to emitted longer wavelength) overshines scattered photons. Many experimental and mathematical approaches have been used to reduce the impact of fluorescence on Raman analysis, but there is still room for improvement. Another noise source can be a sample matrix in which the analyte of interest is distributed. A solvent or excipient, for example, present at high concentration, may obscure the spectrum of an analyte present at much lower concentration.

In order to obtain spatially resolved Raman information, nowadays a Raman spectroscope is usually combined with a confocal microscope. A single Raman spectrum of the random spot on the sample surface provides chemical information about the sample composition. Furthermore, when analyzing the area of interest, Raman spectra can give an insight into chemical composition and its changes as a function of spatial position. Raman spectra can also be collected along a lateral or axial line/surface. When Raman spectra are acquired along an axial line/surface, the measurement is called a depth profile. Two dimensional spectral data sets can be transformed into spectral maps or images, after

single spectra are collected from each pixel. The spectral information can be later transformed into false color images to visualize the different components. Three-dimensional measurements include the assembly of multiple maps to a picture stack, similar to confocal fluorescence imaging.

Every Raman mapping or imaging must be at least semiquantitative, since the relative Raman intensity among pixels is proportional to concentration. Semiquantitative Raman imaging may approximate relative analyte concentration with or without knowledge of the absolute concentration. Another semiquantitative approach is to classify each pixel into groups representing all components of the system, and then to report analyte concentration as the fraction of pixels classified as that analyte (9). If the samples are exhibiting minimal diffuse reflection, quantitative analysis can be more promising. The basis for quantitative analysis using Raman scattering can be explained by Equation 1, which describes a direct proportion between Raman intensity and analyte concentration. However, the Raman cross section, the instrument detection efficiency, and the path length are usually unknown. An image based on uncorrected Raman intensity may provide a qualitative description of analyte distribution, but that distribution may be distorted by many controlled variables, such as focusing errors due to an uneven sample surface or path length variation (10).

One way to improve focusing on the sample surface, which can drastically impede further Raman investigation, is to combine Raman microscopy with optical profilometry. This is a method based on white light which enables three-dimensional mapping of the area of interest (11). By acquiring a topography profile prior to Raman spectroscopy, the profile height information allows for leveling the focal plane to the sample surface for each spectrum acquisition.

In addition to spontaneous Raman scattering, there are several other types of Raman spectroscopy, such as resonance Raman scattering spectroscopy (12, 13), coherent anti-Stokes Raman spectroscopy (CARS), stimulated Raman spectroscopy (SRS), surface-enhanced Raman spectroscopy (SERS) (14), and tip-enhanced Raman spectroscopy (TERS) (15). Each of them has its own capabilities and limitations. Here, we will briefly introduce non-linear Raman techniques, CARS and SRS microscopy, as they are particularly useful for chemical imaging.

1.3 Non-linear Raman Scattering

The major drawback of spontaneous Raman microscopy is the low Raman scattering signal, which as a consequence results in long integration times. In addition, many samples display autofluorescence, which often prevents the detection of a Raman signal. In order to increase the Raman sensitivity by as much as ten orders of magnitude and overcome these limitations, non-linear optical Raman techniques, namely coherent anti-Stokes Raman scattering (CARS) and stimulated Raman scattering (SRS) microscopy have been developed in the last two decades (16-20).

For both approaches, two laser beams with intensities I_{pump} and I_{Stokes} are irradiating the sample. Their signal intensities do not linearly depend on the excitation intensity (non-linear principle), but quadratically (SRS) or cubically (CARS), which as a consequence, enhances the probability of light scattering and reduces the time for analysis:

$$I_{SRS} \propto N\, \sigma_{Raman}\, I_{pump}\, I_{Stokes} \qquad \text{(Equation 2)}$$

and

$$I_{CARS} \propto |\chi^{(3)}|^2 \, I^2_{pump} \, I_{Stokes} \qquad \text{(Equation 3)}$$

Here, σ_{Raman} is the Raman scattering cross section and $\chi^{(3)}$ is the third order non-linear optical susceptibility.

The third-order susceptibility consists of the sum of a resonant part that is enhanced by molecular vibrations and a nonresonant part (background signal) due to the electronic response of the material that is not enhanced by molecular vibrations. Since $\chi^{(3)}$ is proportional to the number of molecules, the two equations can explain an important difference between SRS and CARS. SRS has a linear dependence on the concentration of probed molecules, whereas CARS has a quadratic dependence. Detection of CARS signals ($\omega_{CARS} = 2\,\omega_{pump} - \omega_{Stokes}$) is easier compared to SRS, as they have the frequency different from that of the excitation light and, in addition, allow for simultaneous detection with two-photon excited fluorescence emission and/or second (third) harmonic generation signals. SRS signals, on contrary, are detected as a loss or gain in energy compared to the incident light, which in turn allows for simpler quantitative interpretation.

However, both qualitative and quantitative analyses of spectra are more difficult for CARS than for spontaneous Raman spectroscopy. Numerous approaches have been proposed to reduce the background signal (nonresonant background) and improve the CARS signal. One of them is demonstrated by collecting of the backscattered anti-Stokes signals from thin samples (epi-CARS) which in a great extent reduced the nonresonant intensity from the matrix. A second approach is to use near-infrared pump wavelengths. The nonresonance anti-Stokes intensity can be enhanced if the pump wavelength is near a two-photon absorption band of the sample. Further distortion of CARS spectra can occur from interferences between resonances. For example, one band height can influence the height of a neighboring band. The quadratic dependence of CARS intensity on analyte concentration complicates the resolution of overlapping bands from different materials, as well as the use of standard multivariate analysis algorithms.

All in all, the autofluorescence, different integration times and the spectral latitude are the three main differences between spontaneous Raman microscopy and nonlinear Raman techniques. Non-linear Raman imaging is insensitive against an autofluorescent background, because the Raman and the fluorescence signal are not coinciding. Further, non-linear Raman imaging is several orders of magnitudes faster, with video-rate imaging being achievable (21-23). However, most non-linear Raman microscopy instruments probe only one vibrational resonance at a time which as a result has reduced spectral information compared to spontaneous Raman microscopy. Nevertheless, a broadband CARS has been recognized as a very promising approach to circumvent the last obstacle (24-29). With this method, it is possible to measure multiple anti-Stokes CARS wavelengths simultaneously by using a spectrally broad source for the Stokes beam. Acquisition times per pixel are increased for several reasons including distribution of Stokes beam intensity over many spectral resolution elements, but still much faster than those of spontaneous equivalent. Further development of the broadband CARS and SRS, as well as their growing application in the pharmaceutical field can be expected.

1.4 Pharmaceutical and Biomedical Applications of Raman Spectroscopy

Almost a century after discovery of the Raman effect (1), advanced analytics based on this effect are gaining increasing attention for a wide range of different pharmaceutical and biomedical applications. In contrast to established analytical techniques, Raman spectroscopy provides label-free, non-destructive, chemically selective and spatially resolved analysis. Advanced technical development in

the last decades allowed Raman spectroscopy for implementation into diverse setups ranging from confocal microscopes for acquisition of three-dimensional spectral information up to fiber devices for the application in clinical diagnostics. Furthermore, recent progress in the field of multivariate data analysis used for processing complex spectral data sets significantly facilitated data interpretation.

Raman techniques are implemented in different stages of pharmaceutical development ranging from drug discovery up to the development of drug-loaded carrier systems (30). An important part of the preformulation phase is solid-form screening which can help avoiding problems during later stages of drug development (31-33). The rapid and non-invasive analysis of powders allowed Raman spectroscopy for implementing into different high-throughput and low quantity screening platforms of active pharmaceutical ingredients (APIs) including polymorph and cocrystal screening (34-36). Moreover, Raman spectroscopy has been used for studying phase transformations such as polymorphic changes, anhydrate-hydrate transitions and amorphization (37-40), as well as for identifying the mechanisms of co-crystal formation (41, 42).

Raman spectroscopy can be also applied for microstructural characterization of drug delivery systems, as well as for studying drug-excipient interactions in the formulation. It has been used to control the size distribution of API microparticles and to determine the API distribution homogeneity in tablets (43, 44). Furthermore, Raman spectroscopy is widely applied for characterization of amorphous solid dispersions, formulated to improve the solubility of the poorly soluble actives (45). The nature of water molecules in hygroscopic amorphous polymer matrices such as polyvinylpyrrolidone (PVP) and polyvinylpyrrolidone/vinyl acetate (PVP-VA) copolymers was determined using FT-Raman spectroscopic analysis as a function of moisture content (46).

Confocal Raman microscopy is also being used to characterize printed drug delivery systems (47, 48), and three-layered tablets (49). In combination with optical topography (11), in one of the studies, Raman revealed the reason for different erosion indexes in two formulations. Water soluble mannitol was not present on the tablet surface after soaking in the nanocapsule suspension. Microcrystalline cellulose (MCC), however, was visualized on the surface (Fig. 3B, MCC depicted in blue) (48).
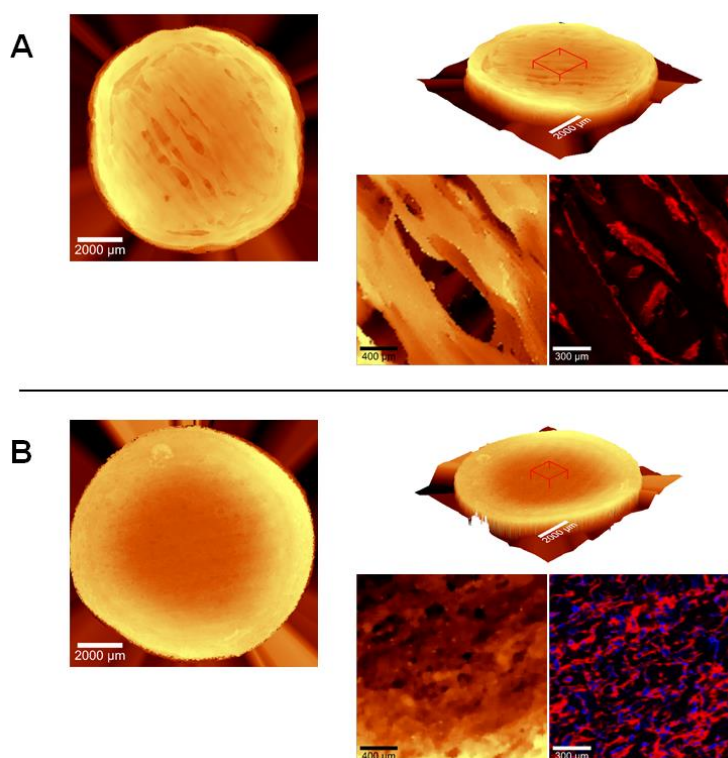
Figure 3. False color Raman images of 3D printed tablets: (A) T-ERL-M and (B) T-ERL-A. Eudragit RL (ERL) is depicted in red, while mannitol (M, figure A) or microcrystalline cellulose (A, figure B) are depicted in blue in the respective image. Reproduced with permission from (48).

Besides, Raman imaging has been used to better understand drug migration during dissolution, and obtain a mechanistic insight into the drug release from the complex matrix systems (50). *In situ* Raman imaging during dissolution has been also reported (45), however non-linear Raman technologies represent a more reliable solution for these purposes, due to much faster acquisition times (51-53).

Raman spectroscopy can be also useful for characterization of stents and implants. The microstructure of drug eluting stents is difficult to investigate using conventional analytics because of the distribution of the formulation as a thin coat over the wire. In this context, Raman was used to analyze rapamycin/ poly(lactic-co-glycolic acid) - PLGA coatings on stents, from the surface through the bulk of the coatings (54). For these purposes Raman is often combined with atomic force microscopy (AFM) which gives the best topographical overview. In combination, these two methods allowed for a comprehensive study on sirolimus-eluting coronary stent and explained the correlation between drug release and device microstructure and pore networks (55).

Raman spectroscopy and imaging have been also successfully employed for the characterization of lipid-based drug delivery systems (56). Here, Raman was used to investigate the homogeneity of semi-solid self-emulsifying drug delivery systems (SEDDS) (57). Moreover, it was applied to investigate the release from liposome formulations (58). Furthermore, Raman spectroscopy can be applied to monitor *in vitro* drug dispersion, lipolysis and supersaturation of lipid-based formulations (59).

The spatial drug distribution on the carrier surface is challenging but very important when testing the aerodynamics and API lung deposition from dry powder for inhalation (DPI). Here, confocal Raman microscopy is used for fast analysis of content uniformity, homogeneity and the polymorphic form of

a drug distributed within a spray-dried inhalable powder (60). Moreover, Raman spectroscopy was shown to exhibit an excellent ability to distinguish the amorphous and crystalline form from a small mass fractions of API (<3% w/w) (61). One more study proved the advantage of two component system in a single inhalation device compared to using separate inhalers (62). Recently, CARS imaging was applied as a useful tool to identify drug particle clusters on the carrier surface of a DPI formulation (63).

With respect to process monitoring, Raman spectroscopy is considered as a feasible process analytical technology (PAT) tool in pharmaceutical industry. Thanks to the ability to obtain a real-time information on a molecular level during pharmaceutically relevant unit operations, Raman is applied for following various processes during production (64). For example, Raman spectroscopy is very reliable for monitoring batch crystallization which is performed in aqueous environment. Here, Raman represents a good alternative to infrared (IR), since water exhibits a strong absorption in the IR region. Thus, the process control and monitoring the polymorphic change upon crystallization can be followed by Raman spectroscopy (65-67). Raman has been applied to monitor synthesis and fermentation of antibiotics (68, 69). Furthermore, Raman was applied as a PAT tool for testing the desired intermediate product in several other unit operations (70), such as blending (71), granulation (72, 73), and coating (74-76). Moreover, Raman spectroscopy has also been applied for inline and real-time monitoring of the hot melt extrusion (77, 78) and freeze-drying process (79-81).

Besides the early phase chemical screening during preformulation, as well as formulation in late phase pharmaceutical development, Raman is also used in product performance testing and quality control of the final product upon market entry. Most of pharmaceutical actives are good scatterers; however this is often not the case with excipients. Although not wide-ranging and comprehensive like IR, Raman databases are also available (82). A Raman device is useful for content uniformity determination in solid oral dosage forms such as tablets (83, 84). For example, Raman imaging was applied to track the degradation of acetaminophen in a tablet (85), or for the material identification through the blister or vial, without sample preparation (86, 87). *In situ* Raman spectroscopy was used to quantify intermediate to final solid forms generated during the dehydration of hydrate forms of piroxicam and carbamazepine (88). Fiber optic Raman probes are often used nowadays for *in situ* monitoring of drug release testing in different *in vitro* dissolution apparatuses and flow-through devices (89). In addition to conventional Raman systems, CARS microscopy has also been increasingly used to study *in vitro* drug dissolution from different solid dosage forms (90, 91).

Even though fluorescence microscopy is still the most commonly applied technique for physiological investigations, Raman microscopy is paving its way as a suitable alternative without the necessity for bulky labelling (92). However, visualizing the API within a dosage form is much easier compared to locating it in more demanding biological samples such as cells or tissues. Here, a brief summary is given of a quite complex approach to apply Raman for biomedical investigations.

One of the first single cell studies using micro-Raman spectroscopy were performed in order to study DNA-protein complexes within cellular microenvironment (93). Since then, Raman spectroscopy has been applied to study the physiology of a broad range of cell types: prokaryotic, eukaryotic, and plant cells (2, 94). Further on, the aim was shifted towards comparing Raman scattering patterns of cells to differentiate between healthy and neoplastic cells (95, 96), or to follow differentiation process of stem cells (97, 98). Moreover, Raman spectroscopy can be combined with microfluidic systems which allows for cellular investigations and cell sorting in a flow (99, 100).

Raman investigation of individual sperm cells helped assessing DNA packaging efficiency in the sperm heads, suggesting that selecting viable sperm cells for *in vitro* fertilization solely based on morphology may not be sufficient (101). Single cell Raman spectroscopy is also used to monitor the deoxygenation and oxygenation of hemoglobin inside human erythrocytes for a duration of 30 minutes (102, 103), as well as for the analysis of erythrocyte disorders characterized by heme aggregation, such as sickle cell disease and malaria (104). Moreover, in combination with optical tweezers, Raman is used to monitor the intracellular ethanol accumulation in yeast cells (105).

As mentioned in the second chapter, Raman-active labelling of small molecules or proteins, carrying stable isotopes (deuterium, for example), facilitates and sometimes enables the detection and imaging of these molecules by spontaneous Raman spectroscopy (6-8). The similar benefit was shown by visualizing molecules carrying alkyne groups inside of the cell (106, 107).

Due to the label-free principle, vibrational spectroscopy techniques have received increased attention in cell-based drug screening studies (108, 109). Allowing for monitoring cellular kinetics in real-time, Raman chemical imaging enables testing the effect of drug, and drug combinations at different time points, in order to determine optimal concentrations and treatment conditions. Raman spectroscopy is particularly attractive for small molecules investigations, when molecular size of fluorescent dyes exceeds the size of the molecule of interest. Cellular biomacromolecules used as biochemical markers and introduced synthetic drugs, both with individual Raman scattering patterns, can be examined simultaneously in order to investigate the effects and interactions between cells and drugs without external labels. This smart principle was applied for studying the response of cancer cells to drugs (substance cleavage or cell apoptosis) (110). As an example, the treatment of gastric carcinoma cells with fluorouracil (5-FU) was followed by the reduction in vibrational band intensities of cellular biomacromolecules, signifying apoptosis (111). The mechanism of action of the anticancer drug etoposide was proved by decreasing DNA and RNA concentrations upon treatment of human pneumocyte-like cells (A549) (112). Real-time measurements of living human cancer cells undergoing apoptosis has been also reported (113).

Raman microscopy has also been used to reveal the mechanism and efficacy of anticancer agents. Spectral changes in cell membrane and different cytoplasmic regions of A549 adenocarcinoma cells were characterized after treatment with cisplatin (114). Advanced multivariate methods in this case could enable to predict the viability according to exposure dose.

Although very promising, spontaneous Raman spectroscopy is still a relatively slow technique, requiring at least an acquisition time of 1s per cell, in the best possible case. Because of this, high throughput measurements on the order of hundreds or thousands of cells are still a missing gap. To overcome this, some research groups work on compressed sensing, by using micro-mirror devices which can lower the data acquisition time per spectrum by 1-2 orders of magnitude (115, 116). For even faster approaches, it is possible to apply the multiplexed coherent Raman spectroscopy, as well as the combination with microfluidic chips, to truly achieve rapid Raman-assisted cell sorting (117).

Besides biochemical changes occurring intracellularly upon drug exposure, Raman can serve for studying drug delivery systems distribution within the cell. So far, Raman microscopy was used to image the intracellular distribution of cationic liposomes in HeLa cells (118), and polystyrene nanoparticles internalized by A549 cells (119). Furthermore, Raman spectroscopy could potentially be used to provide insights into drug targeting mechanisms (120).

Raman spectroscopy is also successfully applied for analyzing even smaller organisms, bacterial cells. Together with optical trapping, Raman spectroscopy could rapidly identify individual endospores in suspension and discriminate them from particles (121). Besides, it is possible to distinguish the bacterial spores from cells in vegetative state (122, 123). Furthermore, subtle differences in Raman spectra of different bacterial species make possible the identification of many microorganisms of clinical relevance (124, 125). The high spatial resolution of confocal Raman microscopy allows for tracking the physiological dynamics in individual bacterial cells, for example overexpression of proteins in genetically modified bacteria (126). Finally, bacterial cells can be tested after exposure to antibiotic drugs by following the evolution of Raman bands associated with DNA, RNA and proteins (127, 128).

The application of methods based on Raman spectroscopy in the pharmaceutical and biomedical field is very broad. This is partly due to the very fast development of instrumentation which ranges from self-built systems with high scientific performance abilities, up to low resolution portable instruments, altogether allowing for multi-stage pharmaceutical research. This includes early phase chemical screening and solid form characterization during preformulation as well as formulation analytics in late phase development. Furthermore, innovative fiber optics-based Raman probe seem to have a versatile application for PAT analysis. The anticipated future trend of continuous manufacturing in the Quality by Design (QbD) framework started including Raman instrumentation adaptable to a wide variety of unit operations. Also, the current development of super-resolution optical microscopy techniques, awarded with the Nobel Prize in Chemistry in 2014, started influencing the other fluorescence-free imaging techniques. Raman imaging, both for *in vitro* and *in vivo* application, is offering a great future potential, but still leaving space for further improvement of the methods based on Raman scattering.

2 Aims

The main goal of this thesis is to apply confocal Raman microscopy for in depth analysis of complex drug delivery systems, investigation of cellular and non-cellular lung barrier and alveolar surfactant secretion, as well as for visualization of cellular interaction with bio-inspired nanocarrier systems. In addition, this involves a critical evaluation of the advantages as well as the limitations of this technique for pharmaceutical applications. In this context, three major aims were followed:

1. To elucidate drug release mechanisms and identify correlations between drug distribution and excipients` properties on drug release from the respective delivery systems.

2. To analyze the microstructure of the human airway mucus and secretion of alveolar surfactant associated with alveolar epithelial cell differentiation in order to investigate the non-cellular human lung barrier.

3. To investigate bioinspired particle uptake by cultured human cells on the subcellular level after applying deuterization as an approach for increasing Raman sensitivity of the molecule of interest.

3   Results and Discussion

3.1   Influence of Component Distribution on Drug Release from Solid Dosage Forms by Confocal Raman Microscopy

This chapter refers to the following publications:

B. Vukosavljevic, L. De Kinder, J. Siepmann, S. Muschert, M. Windbergs; Novel insights into controlled drug release from coated pellets by confocal Raman microscopy. *J. Raman Spectrosc.* 2016, 47:757-762.

K. Puncochova*, **B. Vukosavljevic***, J. Hanus, J. Beranek, M. Windbergs, F. Stepanek; Non-invasive insight into the release mechanisms of a poorly soluble drug from amorphous solid dispersions by confocal Raman microscopy. *Eur. J. Pharm. Biopharm.* 2016, 101:119-25.
* These authors contributed equally to this work.

V. Planz, S. Seif, J.C. Atchison, **B. Vukosavljevic**, L. Sparenberg, E. Kroner, M. Windbergs; Three-dimensional hierarchical cultivation of human skin cells on bio-adaptive hybrid fibers. *Integr. Biol.* 2016, 8(7):775-84.

Due to increasing complexity of novel chemical entities and their corresponding therapy schemes, the development of advanced therapeutics often requires sophisticated approaches, formulations and technologies for the final design of drug delivery systems. In turn, those systems regularly necessitate advanced methods for their comprehensive analytical investigation.

There is broad range of complementary visualization techniques used in the pharmaceutical field. One common method is scanning electron microscopy (SEM). SEM is a valuable tool for imaging drug delivery systems with high spatial resolution however SEM lacks chemical selectivity, operates under vacuum and bares the risk of sample destruction. Furthermore, confocal fluorescence microscopy is a powerful technique allowing for chemically selective and spatially resolved analysis, however staining and fixation used for sample preparation can often influence component distribution as well as tracing of distribution changes upon the contact with different fluids. Additionally, vibrational spectroscopy methods, such as infrared (IR), near infrared (NIR) and Raman spectroscopy represent upcoming analytical tools, as they allow for label-free and chemically selective analysis. However, water exhibits a strong absorption in the IR region, thus hindering analysis during release testing in aqueous medium. In addition to this drawback, visualization of delicate changes within the system often requires high spatial resolution, which can also be a limitation for IR and NIR microscopy.

In contrast, confocal Raman microscopy (CRM) represents a non-invasive, spatially resolved and chemically selective method, allowing for sample investigation in its unperturbed state, thus overcoming some of the previously mentioned obstacles. In the last two decades CRM was applied for microstructural characterization and better understanding of interactions between different components within diverse dosage forms (129) as for instance solid dispersions (130-133), drug-eluting coatings (134-136), polymeric microparticles (137-139), tablets (140-142), etc.

In this thesis, we applied CRM for systematic characterization of three different drug delivery systems: coated pellets, tablets based on amorphous solid dispersions and electrospun fiber mats, in order to analyze component distribution, elucidate mechanisms of degradation and drug release, as well as to better understand the influence of formulation approaches on the final product characteristics. CRM

not only allowed for spatially resolved analysis of drug(s) and excipients (matrix components, coating agents, etc.), but also their changes in the distribution upon degradation and drug release testing, as well as for elucidation of the drug release mechanisms from advanced drug delivery systems.

Nevertheless, like all the other confocal microscopy techniques, CRM investigates one focal plane at a time, thus preventing investigation of highly structured sample surfaces. In order to avoid invasive methods for sample preparation, as for example polishing, whenever it was necessary, we applied optical topography prior to Raman spectroscopy, as a complementary analytical approach (11). Optical topography analysis is based on white light and enables three-dimensional mapping of topographic height differences. Subsequently, acquisition of Raman spectra is directed by the topographic information of the sample, so the microscope focus at each pixel is individually adjusted according to the sample topography. The recorded Raman spectral data set is finally converted into a false color image, using diverse multivariate data methods. In the presented studies, we applied hierarchical cluster and basis analysis as two different multivariate statistical methods for data post-processing. Hierarchical cluster analysis encompasses a binary approach which results into "Boolean" images. Each pixel is assigned to one of the clusters, which represent Raman spectra of different chemical compounds. In contrast, basis analysis comprises acquiring the Raman spectra of individual compounds from the sample as references. Subsequently, the false color images illustrate the relative congruence of the spectra with the predefined reference spectra for each pixel. This is a non-binary approach which allows for a simultaneous display of multiple components in one single pixel, visualized by color intensity differences. This sophisticated multivariate methodology provides a more detailed visualization of the compound distribution.

Coated pellets

Multi-particulate carrier systems such as pellets, in comparison with single-unit delivery systems like tablets and capsules, offer certain therapeutic advantages allowing for simplified and individual dosing and improved patient compliance. The release of active pharmaceutical ingredient/s (API) integrated into pellets can be controlled by convective and/or diffusive mass transport within the pellet matrix. Moreover, in order to protect embedded actives and/or control their release, pellets can be coated with a polymeric film which modify and control drug release properties and associated mass transport mechanisms. Here, we applied CRM for non-destructive and chemically selective analytical investigation of coated drug-loaded pellets in order to visualize compound distribution before and after dissolution testing and elucidate drug release mechanisms.

Pellet cores were prepared by extrusion-spheronization based on a mixture of lactose monohydrate and microcrystalline cellulose as matrix formers, and verapamil hydrochloride as a weak base model drug (10% w/w drug loading). In the subsequent step, pellet cores were coated in a fluidized bed setup with a polymer mixture consisting of Kollicoat® SR 30D - aqueous polyvinyl acetate dispersion, and Kollicoat® IR – polyvinyl alcohol-polyethylene glycol graft copolymer (90:10 w/w), to control drug release from the pellet core. In this study, we applied three complementary approaches for pellet investigation: 1. cross sections analysis after bisectioning (xy); 2. non-invasive whole pellet visualization (xy); and 3. non-invasive virtual cross sectioning - depth profiles (xz), all of them guided by an optical topography profile.

As a first step, spectral investigation of individual pellet compounds was necessary in order to determine suitable peaks for their later identification and visualization within the drug delivery system. After analysis of the pellet cross sections, we could successfully visualize drug, pellet matrix as well as film coating compounds based on their individual Raman peak patterns, with high spatial

resolution. Prior to dissolution testing (Fig. 4A, left), coating film (depicted in yellow) was intact and verapamil hydrochloride (depicted in red) was rather homogeneously distributed within the pellet matrix (depicted in blue). After 45 minutes dissolution testing in acetic buffer pH 3.5 (Fig. 4B, left), we could visualize complete drug release from the pellet matrix and partly film coating disruption.

However, pellet bisectioning can dramatically affect the original sample state, due to involved mechanical stress, and sometimes it was unfeasible to differentiate between defects occurred upon fabrication or upon sample preparation. Consequently, non-invasive methods became necessary for investigation of coating integrity. The Raman investigation of the whole pellet (second visualization approach) demonstrated the intactness and coherence of the coating film before release testing. However, after release testing, some parts of the film were indeed no longer intact. In those areas the Raman signal of the pellet matrix was detectable, leading to assumption that immediate release polymer from the coating film (Kollicoat® IR) was dissolving in the dissolution medium, leaving pores in the coating film.

Despite the usefulness of the whole pellet visualization, this approach does not allow for tracing the changes in the pellet core upon dissolution testing. Therefore, we applied virtual cross sectioning in x-z direction (depth profiles), as a third experimental approach. The penetration depth of the laser through non-transparent media such as pellet is of course limited. Here, the challenge was to successfully optimize the laser power, in order to reach the maximum penetration depth without sample damage. Before dissolution testing, depth profiles enabled detection and visualization of an intact coating layer, as well as the matrix and the drug beneath it, up to the depth of around 100 µm (Fig. 4A, right). After 45 minutes dissolution testing in acetic buffer pH 3.5 (Fig. 4B, right), however, we non-invasively visualized the pore formation (Fig. 4B, marked with an arrow) within the coating layer as well as drug depletion from the matrix due to contact with the release medium.
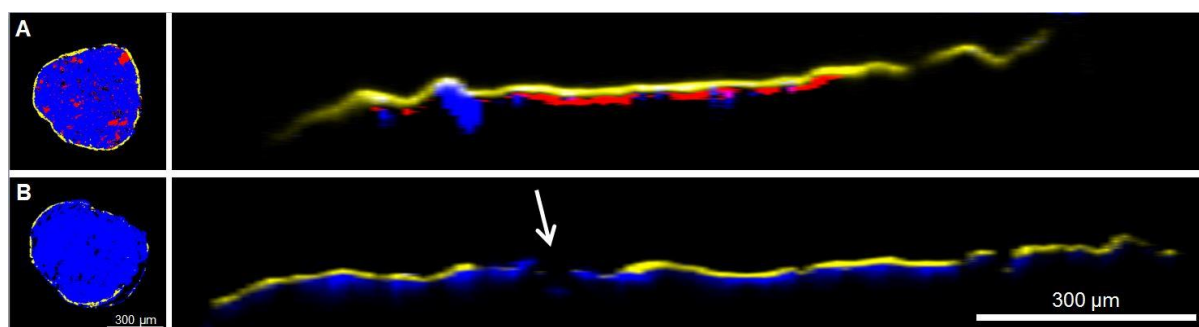
Figure 4. Cross sections and virtual cross sections of pellets before (A) and after release testing (B). False colors depict the matrix in blue, film coating in yellow and the drug in red, respectively.
Reprinted from B. Vukosavljevic, L. De Kinder, J. Siepmann, S. Muschert, M. Windbergs; Novel insights into controlled drug release from coated pellets by confocal Raman microscopy. J. Raman Spectrosc. 2016, 47:757-762, Copyright (2016), with permission from John Wiley & Sons, Ltd. (50)

Pore formation within the coating film is most likely playing the key role in controlling drug release from the pellet core, as it allows for more rapid drug transport upon contact with the release medium. Furthermore, close to the visualized pores there was no drug detectable close to the coating film, illustrating complete drug release.

Altogether, non-invasive pellet surface visualization and virtual cross sectioning, represent a good complementary approach to bisectioning for comprehensive investigation of coated drug delivery systems, ranging from compound distribution and its changes upon release testing, up to elucidation of complex drug release mechanisms.

Tablets based on amorphous solid dispersion

The formation of amorphous solid dispersions via hot-melt extrusion or solvent evaporation (i.e. spray drying) represent one of the most successful approaches for increasing solubility and dissolution rate of poorly soluble APIs. However, despite better wettability properties and particle size reduction, solid dispersions are susceptible to thermodynamic instabilities resulting in recrystallization of the API upon storage or dissolution. In this respect, the crucial factor in the development of stable amorphous solid dispersion is the complexation effect of the polymer and the ability of the matrix to incorporate and stabilize a homogenously dispersed amorphous API. At the same time, *in vitro* dissolution profiles represent a very critical parameter of every formulation, as only a stable and reproducible API release from the delivery system enables a safe and effective drug therapy. In this study, our aim was to investigate *in situ* drug release and recrystallization mechanisms of a poorly water soluble model drug from amorphous solid dispersions and to elucidate the influence of polymer properties on stability and release behavior of API from those systems.

Solid dispersions based on either Soluplus® (polyvinyl caprolactam-polyvinyl acetate-polyethihylene glycol graft copolymer) - an amphiphilic copolymer and solubilizer, or polyvinylpyrrolidone K30 (PVP) - a hydrophilic polymer, and aprepitant, a poorly water soluble model drug, were in the first step successfully prepared by spray drying (drug:polymer 1:3, w/w). The formation of amorphous solid dispersions in both formulations was confirmed by differential scanning calorimetry (DSC) which showed one glass transition temperature with a significant decrease compared to the pure polymers. In the next step, the spray-dried particles were compressed to 7mm tablets, as a final dosage form.

Although aprepitant in both cases exhibited its amorphous form, the cumulative release profiles of the two formulations were significantly different (Fig.5). The release from the Soluplus® matrix was slow but steady, and followed a linear kinetic. Visually, tablets based on Soluplus® swelled without observation of erosion, thus forming a diffusion barrier for aprepitant. The release from the PVP matrix, however, was different. Due to the good PVP solubility in water, in the first 60 min. drug release was faster, but between 60 and 480 min., the slopes of the release curves from both matrices were similar. However, after 480 min. aprepitant precipitated and its bulk concentration dramatically decreased. Unlike Soluplus®, the swollen PVP matrix was susceptible to erosion.
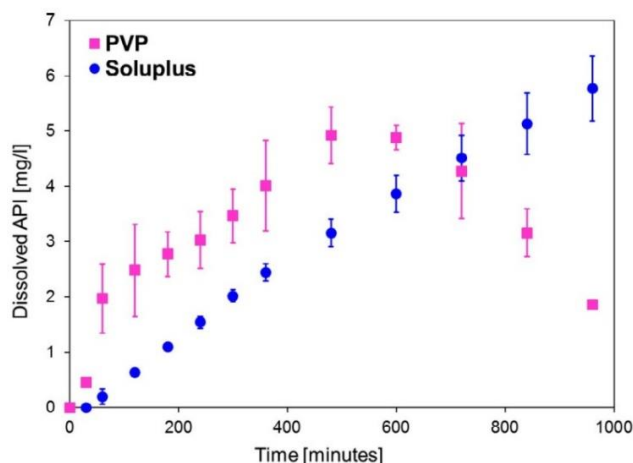
Figure 5. Cumulative release profiles of aprepitant from tablets compressed of spray-dried particles of amorphous solid dispersions of aprepitant in Soluplus and PVP.

Reprinted from K. Puncochova, B. Vukosavljevic, J. Hanus, J. Beranek, M. Windbergs, F. Stepanek; Non-invasive insight into the release mechanisms of a poorly soluble drug from amorphous solid dispersions by confocal Raman microscopy. Eur. J. Pharm. Biopharm. 2016, 101:119-25, Copyright (2016), with permission from Elsevier. (45)

In order to understand those differences in release behavior from two matrix systems, we applied CRM for non-invasive *in situ* investigation of the release and recrystallization processes directly in dissolution medium in static conditions. Due to swelling and gel formation during dissolution, the challenging task was to preserve the intactness of the diffusion barrier and follow the spatial distribution changes within the matrix. We applied virtual cross section imaging in x-z direction based on individual Raman spectra of tablet components.

For each measurement, we initially focused on the tablet surface and let the laser penetrate into the sample down to the depth of around 20 μm. Tablets compressed from spray-dried Soluplus:aprepitant particles did not indicate any recrystallization or phase separation during dissolution testing (Fig. 6A). In contrast, the PVP:aprepitant matrix showed very fast phase separation (pure PVP depicted in light blue in Fig.6B) followed by drug recrystallization on the tablet surface (drug crystals depicted in pink in Fig.6B).
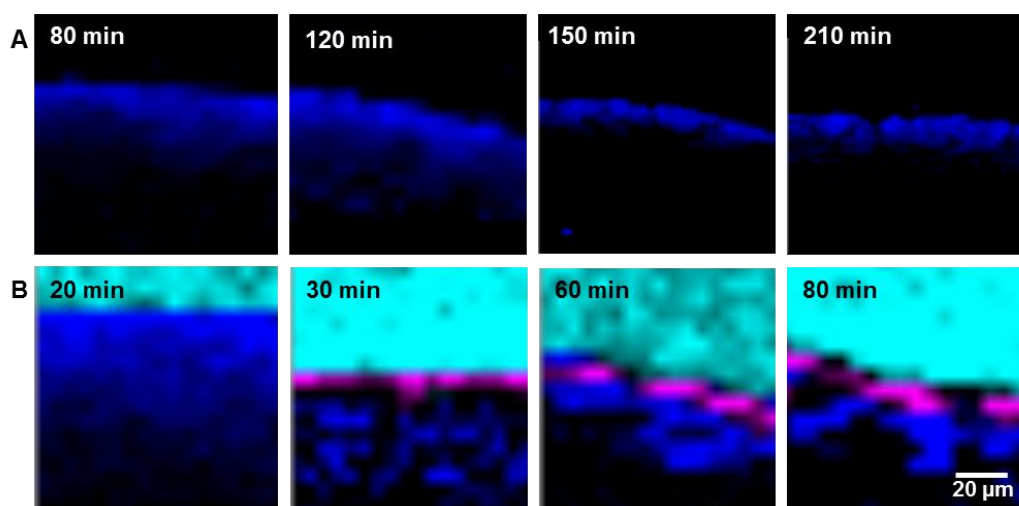
Figure 6. Raman imaging of compound distribution changes during dissolution. (A) Tablet (Soluplus:aprepitant) and (B) tablet (PVP:aprepitant). False colors depict the solid dispersion in dark blue, pure PVP in light blue, and pure drug crystals in pink, respectively.
Reprinted from K. Puncochova, B. Vukosavljevic, J. Hanus, J. Beranek, M. Windbergs, F. Stepanek; Non-invasive insight into the release mechanisms of a poorly soluble drug from amorphous solid dispersions by confocal Raman microscopy. Eur. J. Pharm. Biopharm. 2016, 101:119-25, Copyright (2016), with permission from Elsevier. (45)

The potential reason for the occurrence of this interesting phenomenon can be the difference in the chemical structures between two polymers. Soluplus® contains many hydrogen donors and acceptors responsible for interactions with the drug and solvent resulting in continuous release without any recrystallization of the poorly soluble API. PVP, on the contrary, has a hydrophilic character and exhibits fewer functional groups, thus leading to clear instabilities.

This study elucidates that the combination of Soluplus® and PVP polymers in one matrix might improve slow drug release from the Soluplus® matrix, and at the same time inhibit precipitation of the API from the PVP matrix. Moreover, CRM represents an upcoming tool for non-invasive investigation of amorphous solid dispersions, as well as the influence of polymer properties on drug release kinetics from those drug delivery systems.

Electrospun fiber mats as bio-inspired functional materials

The rational development of bio-inspired functional materials is a very challenging task which involves examination of the complex interactions of human cells with material surfaces. In this study, we designed three different types of electrospun fiber mats with individual biomechanical characteristics and analyzed their component distribution and degradation kinetics using confocal Raman microscopy in order to finally correlate their physicochemical characteristics with their interactions with human cells.

First, we electrospun one component fiber mats based on polycaprolactone (PCL), a FDA-approved, biocompatible polymer, which provided a mechanically stable and flexible fiber matrix. Further, in order to increase the wettability of the fiber surface and thus optimize cell attachment, we electrospun blend fibers based on PCL and gelatin (natural, water soluble polymer) mixture. As a third approach, we developed ''hybrid'' fibers by combining pure gelatin fibers with blend fibers (PCL/gelatin) into one scaffold (co-electrospinning) which intended to provide a dense fiber network for the initial cell attachment, but further upon slow degradation of gelatin, increasing porosity and more space for scaffold infiltration.

As the spatial distribution of fiber compounds strongly affects the biomechanical properties of the material, we applied CRM to localize PCL and gelatin in blend fibers. Visualization of the electrospun fiber mats is, however, very challenging due to the three-dimensional orientation of the overall network and at the same time the very thin and delicate structure of the individual fibers. Based on z-stack analysis, virtual slices of the fibers in different focal planes enabled spatially resolved and three-dimensional visualization of the fiber composition. Interestingly, gelatin was mainly detected on the fiber surface, whereas the cores of the fibers consisted of PCL. These results were in good correlation with contact angle measurements which demonstrated a rather hydrophobic surface of PCL fibers, whereas blend and hybrid fibers, which contained water soluble gelatin, demonstrated improved hydrophilicity and excellent wettability.

Furthermore, we used SEM and CRM to examine the degradation kinetics of gelatin in "hybrid" fibers which compared to the other two fiber mats exhibited the best biomechanical properties. The degradation studies were performed in PBS buffer solution at 37 ℃ during four months. Before degradation, two fiber types with different diameters were identified within the hybrid fiber mats using SEM. Nevertheless, chemically selective investigation using CRM was needed in order to differentiate between those fiber types. As shown in Fig. 7A, the thinner fibers were composed of gelatin (depicted in green) and the thicker ones of both PCL (depicted in red) and gelatin, representing blend fibers. During and after the degradation study, pure gelatin fibers were completely degraded, indicated by the absence of thin green fibers in the false color Raman image (Fig. 7B). At a higher magnification, the degradation of gelatin was also identified on the surface of the blend fibers. Before degradation, the fibers exhibited a smooth surface, mainly based on gelatin (Fig. 7C). After degradation, the dissolved gelatin leaves the small voids in the surface (Fig. 7D).
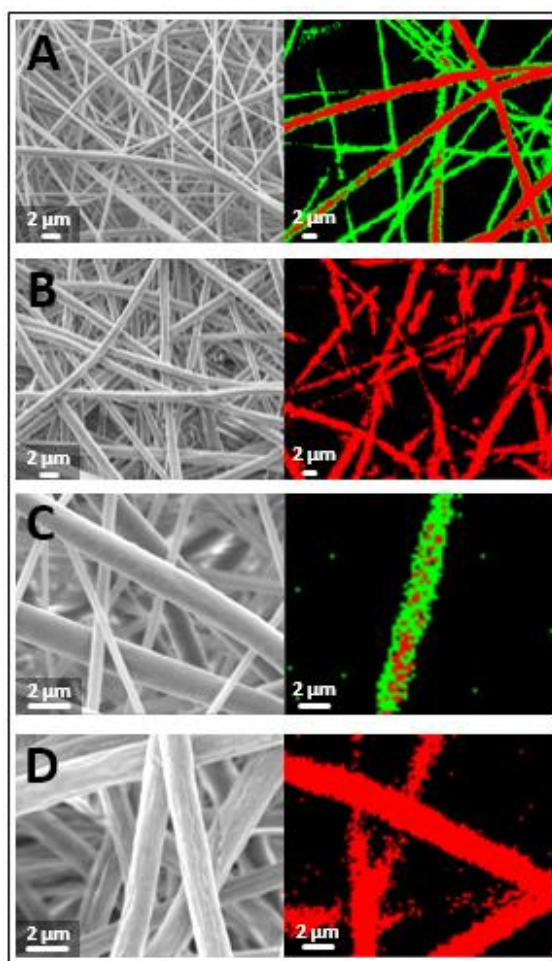
Figure 7. Evaluation of degradation kinetics of gelatin from hybrid fiber mats using SEM and Raman analysis (PCL – red, gelatin – green); (A) before degradation; (B) after degradation; (C) before degradation at higher magnification exhibiting a smooth surface; (D) after degradation at higher magnification exhibiting a structured surface.

Adapted from V. Planz, S. Seif, J.C. Atchison, B. Vukosavljevic, L. Sparenberg, E. Kroner, M. Windbergs; Three-dimensional hierarchical cultivation of human skin cells on bio-adaptive hybrid fibers. Integr. Biol. 2016, 8(7):775-84, Copyright (2016), with permission from the Royal Society of Chemistry. (143)

The degradation kinetics of the hybrid fiber mats matched the requirements for cell cultivation, by providing a dense gelatin-rich structure at the beginning, but subsequently high porosity of the fiber mat, leaving more space for cell infiltration and migration into the remaining part of the blend fibers. Here, CRM allowed for advanced visualization of bio-inspired functional materials, such as fiber mats, without any labeling.

In summary, various solid drug delivery systems have successfully been visualized using confocal Raman microscopy in combination with optical profilometry, when necessary. Using different imaging approaches, it is possible to investigate component distribution as well as the underlying mass transport mechanisms of the drug from the matrix and to better understand the changes of the system upon contact with the dissolution medium. Overall, CRM enabled to fill the missing analytical gap between component distribution and *in vitro* dissolution testing, as well as the change of the dissolution rates from different dosage forms happening upon small differences in the formulation process or excipients. This corroborates that non-invasive Raman investigation represents a versatile technique for analytical characterization of carrier systems, thus supporting rational development of novel therapeutics and improved product safety.

3.2   Chemically Selective Investigation of the Non-Cellular Human Lung Barrier

This chapter refers to the following publications:

B. Vukosavljevic*, X. Murgia*, K. Schwarzkopf, U.F. Schaefer, C.M. Lehr, M. Windbergs; Tracing molecular and structural changes upon mucolysis with N-acetyl cysteine in human airway mucus. *Int. J. Pharm.* 2017, 533: 373–376.
* *These authors contributed equally to this work.*

B. Vukosavljevic, M. Hittinger, H. Hachmeister, C. Pilger, X. Murgia, M. Gepp, L. Gentile, H. Huwer, N. Schneider-Daum, T. Huser, C.M. Lehr, M. Windbergs; Vibrational spectroscopic imaging and live cell video microscopy for studying differentiation of primary human alveolar epithelial cells, submitted.

The airway mucus of the conducting airways and the pulmonary surfactant secreted by alveolar epithelium represent a major non-cellular pulmonary barrier against external airborne threats. Therefore, insight into the biochemical mucus structure and surfactant secretion from alveolar epithelial cells upon their differentiation is of high interest for elucidating the course of lung diseases as well as for rational development of effective therapeutics for lung application.

Applying confocal Raman microscopy (CRM) for biological investigation faces a challenge, as the Raman scattering of biological samples is inherently weak in comparison to chemical compounds. Nevertheless, the technique is sensitive enough to detect spectral differences for the differentiation of subcellular compartments. Here, very important prerequisite is the right substrate compatible with Raman imaging. In this context, we used calcium fluoride glass slides which are superior to standard plastic dishes, as their Raman bands do not interfere with signals originating from the sample and can easily be subtracted from the data set.

In the presented studies, we applied CRM for label-free and chemically selective investigation of the human mucus microstructure and its changes upon chemical mucolysis, as well as for visualization of the gradual metamorphosis of alveolar type II (ATII) lung cells, in order to comprehensively investigate the non-cellular human lung barrier. Human airway mucus (144) and lung tissue samples (145) were collected from patients undergoing elective surgery, both after informed consent from all participants and/or their legal guardians and in compliance with a protocol approved by the Ethics Commission of the "Ärztkammer des Saarlandes" (file numbers 19/15 and 136/13).
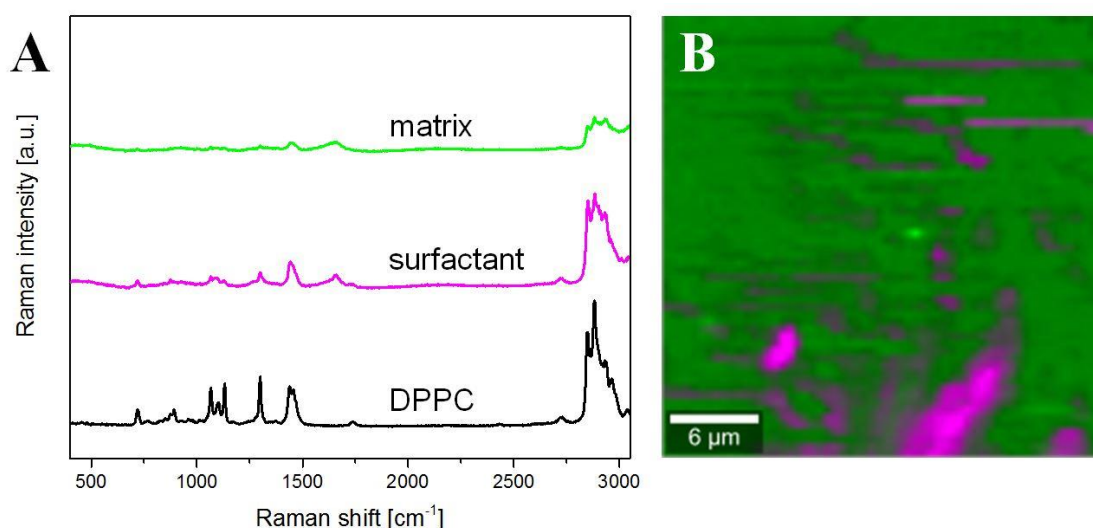
Human airway mucus

As mucus lines the surface of the airways, its molecular and structural properties can affect pathophysiological processes as well as absorption of actives administered via the pulmonary route. Therefore, insight into the biomechanical mucus structure and better understanding of its composition and interactions is of major interest. In this study, the aim was to analyze structure and composition of the human airway mucus in its native state and after freeze drying using CRM as a label-free technique.

Airway mucus is a complex hydrogel mainly consisting of water (95% w/w) with incorporated glycoproteins (mucins, 2-5% w/w), non-mucin proteins, lipids, salts, DNA, enzymes, cellular debris,

and pulmonary surfactant. Systematic analysis in its native state is very challenging, as it requires conserving the hydration state of the hydrogel to avoid collapsing of the gel mesh. In this context, CRM is an upcoming tool as it enables chemically selective investigation without sample manipulation (e.g. staining, fixation), which are usual requirements for well-established techniques.

Upon investigation of different human airway mucus samples, we successfully differentiated individual signal contributions of pulmonary surfactant (depicted in pink, consisting of phospholipids associated with surfactant proteins) and mucus matrix (depicted in green, consisting of glycoproteins and lipids) and resolved their spatial distribution, as shown in representative false color Raman image in Fig. 8. The surfactant spectrum was very distinctive and comparable to dipalmitoyl phosphatidylcholine (DPPC, Figure 8A), which is a major constituent of the pulmonary surfactant (146). The most important spectral assignments of DPPC (reference spectrum presented in Fig. 8A) and surfactant-like spectra were: choline head group at 717 cm^{-1}, three distinct peaks at 1066 cm^{-1}, 1102 cm^{-1} and 1128 cm^{-1} representing the carbon backbone vibrations, and aliphatic ester at 1740 cm^{-1}.


Figure 8. Analysis of the native human airway mucus: (A) Single Raman spectra assigned to the mucus matrix, to pulmonary surfactant and to dipalmitoyl phosphatidylcholine (DPPC) as a reference, respectively; (B) False color Raman image representing the spatial distribution of the pulmonary surfactant in the mucus matrix (xy-scan). False colors depict the mucus matrix in green, and the pulmonary surfactant in pink, respectively.
Reprinted from B. Vukosavljevic, X. Murgia, K. Schwarzkopf, U.F. Schaefer, C.M. Lehr, M. Windbergs; Tracing molecular and structural changes upon mucolysis with N-acetyl cysteine in human airway mucus. Int. J. Pharm. 2017, 533: 373–376, Copyright (2017), with permission from Elsevier. (147)

As Raman imaging of the spatially resolved compound distribution within the mucus mesh was exacerbated by the samples` gel-like structure and the high water content, in the next step we investigated freeze-dried mucus samples using SEM and CRM. SEM revealed the typical mesh-like structure with a highly heterogeneous pore size, ranging from pores in the nanoscale up to pores in the range of 1-10 μm (Fig. 9A).

Furthermore, we applied Raman imaging for chemically selective and label-free visualization. Two Raman spectra, one consisting of all prominent glycoprotein and lipid related peaks, representing the

mucus matrix, and the other one consisting of peaks corresponding to disulfide bonds (-S-S-) at 492 cm^{-1} and the surfactant related choline head group (-N+) at 717 cm^{-1} were successfully identified (Fig. 9B). After conversion of the Raman spectra into false-color images, areas in which mucins interact by disulfide binding could be visualized (Fig. 9C). These areas, depicted in blue, were located in the edges of thin mucin fibers, thus most likely stabilizing the fragile macrostructure of human airway mucus.
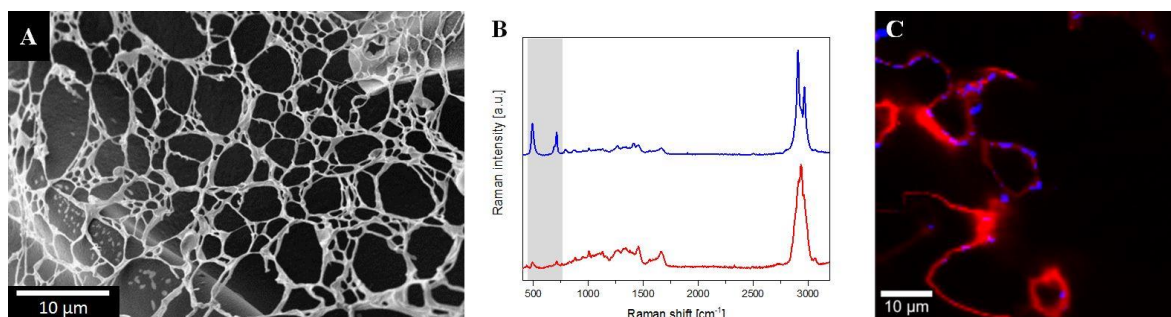
Figure 9. Analysis of the freeze-dried mucus: (A) SEM image; (B) two individual single Raman spectra corresponding to the mucus matrix (red) and cysteine-rich domains (blue) with the spectral region of interest highlighted; (C) false color Raman image (same color coding like in 3B).
Reprinted from B. Vukosavljevic, X. Murgia, K. Schwarzkopf, U.F. Schaefer, C.M. Lehr, M. Windbergs; Tracing molecular and structural changes upon mucolysis with N-acetyl cysteine in human airway mucus. Int. J. Pharm. 2017, 533: 373–376, Copyright (2017), with permission from Elsevier. (147)

Moreover, in order to investigate potential changes in the mucus microstructure upon mucolytic treatment, we incubated the human airway mucus with N-acetylcysteine (NAC, 10% w/w), as an established therapeutic mucolytic agent. Here, SEM images of NAC-treated samples showed a partially collapsed mesh structure contrasting the structure of non-treated mucus. Additionally, Raman spectra of freeze dried mucus samples after mucolysis revealed the presence of free thiol (-SH) groups at 2560-2590 cm^{-1}, thus proving the reduction of the disulfide bonds within the mucus matrix upon mucolytic treatment.

Our approach for label-free investigation of human airway mucus provides new insights into its microstructure and brings Raman microscopy in focus as an upcoming tool for elucidation of the interaction mechanisms between the mucus and airborne threats.

Differentiation of primary human alveolar epithelial cells

In order to thoroughly investigate alveolar surfactant production and secretion, we further studied differentiation of primary human alveolar epithelial cells. The alveolar epithelium in the peripheral lung is mainly composed of barrier forming alveolar type I (ATI) and surfactant producing alveolar type II (ATII) cells. As ATII cells act as progenitors for the ATI phenotype, upon differentiation, they extracellularly secret alveolar surfactant and significantly grow and flatten in order to form the air-blood barrier. Here, we applied a combination of confocal fluorescence microscopy and spontaneous Raman as well as coherent anti-Stokes Raman scattering (CARS) microscopy to study the differentiation of human ATII cells.

We isolated primary human alveolar epithelial cells from lung tissue of patients undergoing lung resection and cultivated them for seven days (145). In order to visualize surfactant rich vesicular structures, which are typically considered as an indicator for ATII cells, and their gradual disappearance over time during cell differentiation, in the first step we used laurdan as a reference fluorescence marker for our study. Laurdan detects time and temperature dependent changes in membrane phase properties and allowed for visualization of individual lipid vesicles.

In the next step, we applied label-free Raman microscopy techniques to investigate the cell differentiation process based on the spectral information comprising content, distribution, and concentration of cellular biopolymers (such as DNA, RNA, proteins, lipids, and carbohydrates) on the molecular level. After spectral assignment of the Raman peak patterns, we were able to distinguish the signal contributions of nucleus, cytoplasm, membrane, and lipid vesicles (phospholipid vibrations) characteristic of the ATII phenotype (Fig. 10A). The Raman spectrum of lipid vesicles (depicted in pink) was very distinctive, with major contributions by spectral patterns of dipalmitoyl phosphatidylcholine (DPPC), a major constituent of the pulmonary surfactant. Upon differentiation, these vesicles fuse with the cell membrane and secrete the alveolar surfactant into the extracellular environment. ATI-like cells, however, yielded spectra with significantly less lipid content and absence of vesicular structures (Fig.10B).
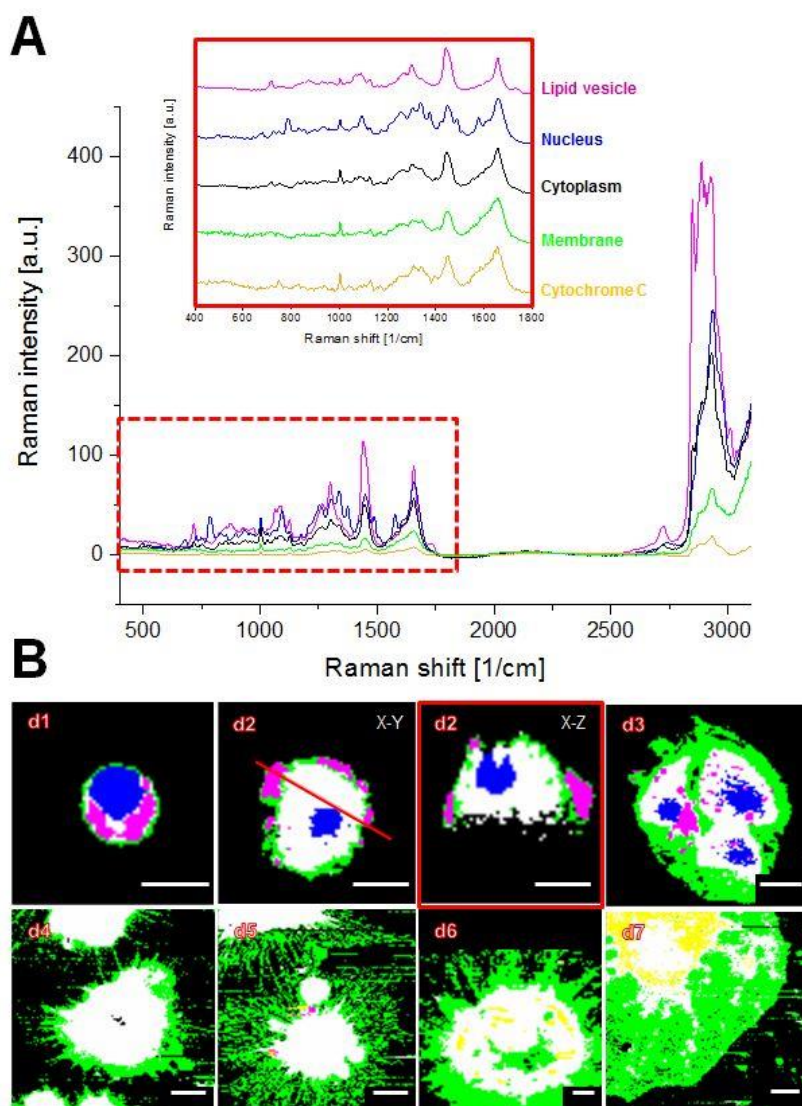
Figure 10. Differentiation of alveolar epithelial cells in primary culture visualized by confocal Raman microscopy. A. Raman spectra (full, raw spectra and normalized fingerprint region) of different cellular compartments: lipid vesicles (pink), nucleus (blue), cytoplasm (black), cellular membrane (green), and cytochrome c (yellow), respectively; B. Representative Raman images for days 1-7 (d1-d7), respectively. The red line at d2 depicts the focal plane of the X-Z cross section presented next to the X-Y scan (scale bars 10 μm).

B. Vukosavljevic, M. Hittinger, H. Hachmeister, C. Pilger, X. Murgia, M. Gepp, L. Gentile, H. Huwer, N. Schneider-Daum, T. Huser, C.M. Lehr, M. Windbergs; Vibrational spectroscopic imaging and live cell video microscopy for studying differentiation of primary human alveolar epithelial cells, submitted.

Upon differentiation, alveolar epithelial cells dramatically grow and flatten, making their visualization with CRM very challenging. Therefore, we additionally applied CARS microcopy which allowed for a 3D visualization of alveolar surfactant rich vesicles within ATII cells and their secretion. Finally, as an additional investigational approach, we applied hyperspectral (HS) CARS imaging. After scanning the samples in the spectral range from 2700 to 3050 cm⁻¹, we were able to spectrally differentiate lipid rich vesicles (2845 cm⁻¹) from cellular proteins (2930 cm⁻¹) according to their vibrational signature, and thus to further corroborate the confocal Raman microscopy experiments (Fig. 11).
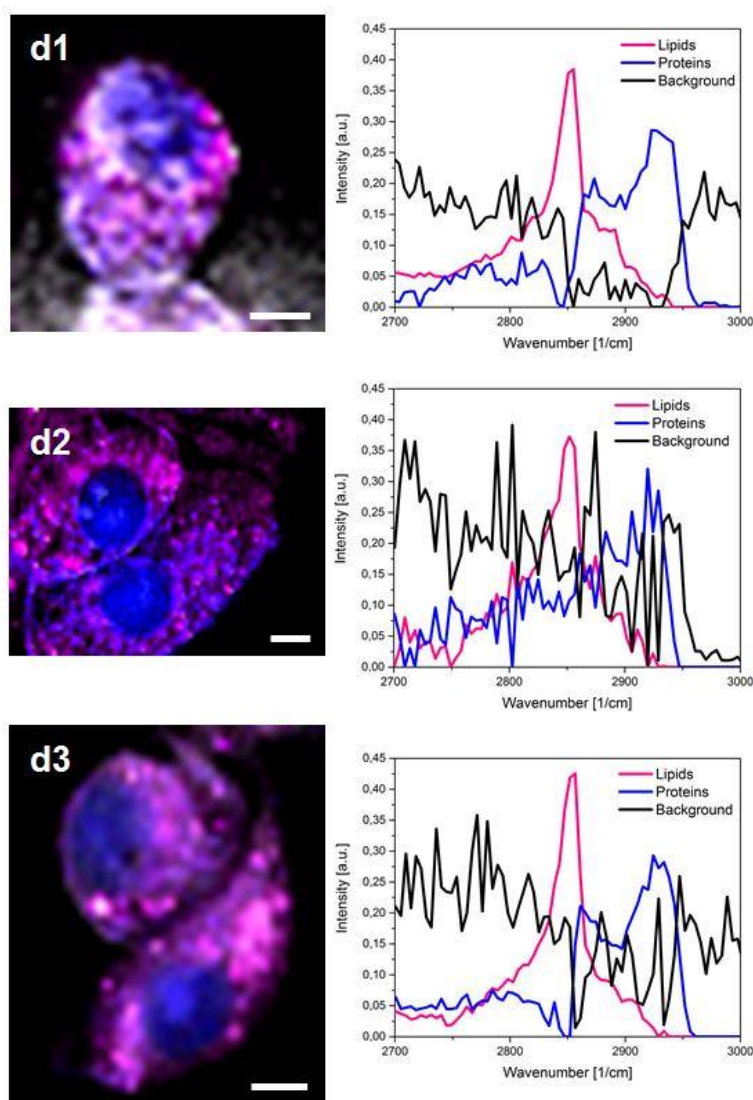
Figure 11. Hyperspectral (HS) CARS overlay images of ATII cells at day 1, 2 and 3. Three individual channels representing the lipid rich environment depicted in pink; nuclei depicted in blue; background depicted in grey, respectively (scale bars 1 μm).
B. Vukosavljevic, M. Hittinger, H. Hachmeister, C. Pilger, X. Murgia, M. Gepp, L. Gentile, H. Huwer, N. Schneider-Daum, T. Huser, C.M. Lehr, M. Windbergs; Vibrational spectroscopic imaging and live cell video microscopy for studying differentiation of primary human alveolar epithelial cells, submitted.

In this section, it is shown that confocal Raman microscopy is well suited for the analysis of complex human samples, primary lung cells as well as the airway mucus. As a complementary method for cellular investigations coherent anti-Stokes Raman scattering (CARS) microscopy contributed to a better understanding of complex biochemical changes happening upon cellular differentiation. These results do not only enrich the knowledge about the mucus microstructure and human alveolar epithelial cells differentiation, but also, pave the path to further label-free pulmonary surfactant corona investigation and rational development of future lung therapeutics.

3.3 Non-Invasive *In Vitro* Uptake Visualization of Squalenoylated Nanoparticles into Breast Cancer Cells with Different LDLR Expression

This chapter refers to the following publications:

Buchy, B. Vukosavljevic, M. Windbergs, D. Sobot, C. Dejean, S. Mura, P. Couvreur, D. Desmaele; Synthesis of a deuterated probe for the confocal Raman microscopy imaging of squalenoyl nanomedicines. Beilstein J. Org. Chem. 2016, 12:1127-1135.

D. Sobot, S. Mura, M. Rouquette, B. Vukosavljevic, F. Cayre, E. Buchy, G. Pieters, M. Windbergs, D. Desmaele, P. Couvreur; Circulating lipoprotein: a Trojan horse guiding squalenoylated drugs to LDL-accumulating cancer cells. Mol. Ther. 2017; 25(7):1596-1605.

In the last few decades, nanomedicines were widely investigated as an approach for treatment of severe diseases such as cancer, intracellular infections, neurodegenerative diseases, etc. Nanocarrier systems designed for these purposes often exhibited a significant improvement in pharmacokinetics, biodistribution, stability, specificity, therapeutic efficacy and toxicity compared to the free active compounds, thus increasing potential for prudent application of those systems. Due to an emerging understanding of the complex comorbidities as well as of potential toxicological effects of nanotherapeutics on the subcellular level, their interaction and potential uptake into cells represent one of the first steps to study their fate in the human body. In this context, there is a strong need for advanced analytical methods for investigation of pure nanomaterials, cells and their interactions.

Hence, confocal Raman microscopy (CRM) represents an upcoming analytical tool. As described in the previous chapter, this method does not only allow for spectral differentiation of subcellular compartments, but also for intracellular visualization of nanocarrier systems. However, for the simultaneous detection and visualization of both, cellular compartments and the drug/carrier system, significant spectral contrast is usually an obstacle. This is especially the case when dealing with low drug concentrations or biological structures such as peptide drugs or nucleoside analogues.

This chapter refers to the application of CRM for studying bioinspired nanocarriers, the obstacles occurring upon simultaneous detection of those systems and biological material, as well as the potential solution to overcome insignificant spectral contrast. We investigated the cellular uptake and intracellular localization of squalenoylated nanoparticles, as bioinspired nanocarrier systems. The chemical conjugation of the anticancer drug gemcitabine (Gem) to squalene (SQ) - a natural and biocompatible triterpene, led to the formation of the prodrug (GemSQ) which spontaneously self-assembles in water, forming nanoparticles (GemSQ NPs) (148). Recently, it has been revealed that GemSQ NPs interact with lipoproteins (especially low density lipoproteins-LDL) in the blood, thus allowing for indirect cancer cell targeting, due to their high lipoprotein receptors expression (149). In order to prove this on the subcellular level, we used CRM for label-free analysis of GemSQ NPs, their internalization and interaction with MDA-MB-231 and MCF-7, two breast cancer cell lines with different LDL receptors expression levels.

First attempts to detect and locate lipid based GemSQ NPs within the cell were unsuccessful because each cellular compartment (i.e. nucleus, cytoplasm, and intracellular lipid droplets) contained certain lipids which contributed to the overall Raman spectrum of the cell. In this particular case, Raman detection of the GemSQ NPs was not possible due to intracellular lipid droplets which are omnipresent

in highly metabolically active cancer cells. For circumventing this problem, we repeated the same experiments using deuterized NPs (GemSQ-d_6), an approach applied for increasing the Raman sensitivity of the molecules of interest (8).

Inclusion of specific functional groups such as alkyne, or compound deuterization gained attention as potential markers to increase the Raman scattering activity and specifity as they display Raman peaks in the silent region (1800-2800 cm^{-1}), a part of the spectrum where natural molecular vibrations of cells rarely occur, and thus not perturbe with the analysis of live cells (4-7).

The synthesis of deuterated squalenic acid was achieved from natural squalene through the Shapiro reaction (150) (0.6% yield). The synthesized deuterated squalenic acid was further coupled to gemcitabine to provide the deuterated analogue of squalenoyl gemcitabine (GemSQ-d_6). The GemSQ and GemSQ-d_6 NPs suspensions were prepared in a single step by nanoprecipitation of an ethanolic solution in milli-Q water (148). After spontaneous formation of the NPs, the organic solvent was evaporated under vacuum (Fig. 12A). The individual Raman spectra of the raw substances as well as of the particles were recorded (Fig. 12B). As depicted in Fig. 12C and Fig. 12D, the Raman spectra of the deuterated and non-deuterated compounds revealed no differences in their scattering patterns except from the unique spectral bands of the deuterium isotope generated in the silent spectral region (around 2200 cm^{-1}). In addition, both analogues showed the same self-assembling properties (120).
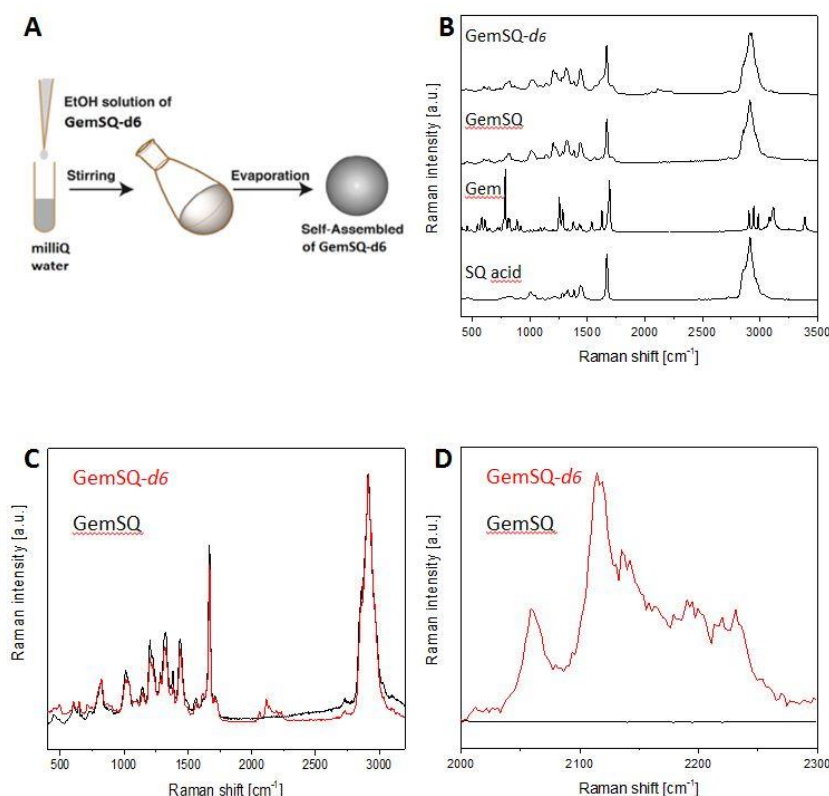

Figure 12. (A) Sketch depicting the procedure of preparing the NPs; (B) Single Raman spectra of GemSQ-d6 NPs, GemSQ NPs, gemcitabine and squalenic acid, respectively; (C) Single Raman spectra of deuterated GemSQ-d6 NPs (red) and GemSQ NPs (black); (D) Close-up showing the difference between deuterated and non-deuterated compounds.
Reprinted from E. Buchy, B. Vukosavljevic, M. Windbergs, D. Sobot, C. Dejean, S. Mura, P. Couvreur, D. Desmaele; Synthesis of a deuterated probe for the confocal Raman microscopy imaging

of squalenoyl nanomedicines. Beilstein J. Org. Chem. 2016, 12:1127-1135, Copyright (2016), with permission of the Beilstein Journal of Organic Chemistry (open access). (150)

In the next step, we aimed for label-free visualization of cancer cells and their interaction with deuterated nanoparticles. Control experiments (cell imaging prior to NP incubation) revealed that MDA-MB-231 cells were much more abundant in intracellular lipid droplets (depicted in cyan blue) than MCF-7 cells, thus indicating a difference in the lipid metabolism between the two cell lines (Fig. 13A and 13B). Furthermore, the use of GemSQ-d_6 NPs allowed for their detection and visualization even in the lipid-rich intracellular environment, based on the unique spectral bands of the deuterium isotope. After 2 hours incubation with GemSQ-d_6 NPs, a significant intracellular accumulation was observed in MDA-MB-231 cells (Fig. 13C), whereas no NPs were detected in MCF-7 cells under the same conditions (Fig. 13D), most likely due to their lower LDLR expression.
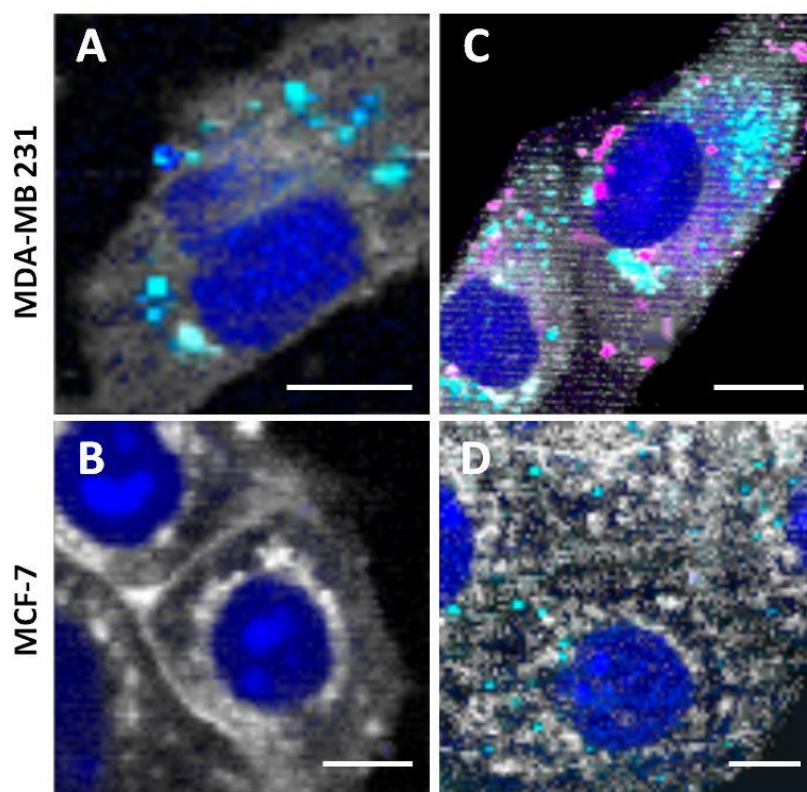
Figure 13. Confocal Raman images of MDA-MB-231 and MCF-7 breast cancer cell lines showing a comparison of ^{2}H-SQGem NPs uptake: (A, B) Representative images of non-treated MDA-MB-231 (A) and MCF-7 (B) cells (control). (C and D) MDA-MB-231 (C) and MCF-7 (D) cells incubated with NPs (77 mM) for 2 hours at 37°C. False-color Raman images were generated based on different scattering patterns of different cellular compartments. False colors visualize nucleus in dark blue, cytoplasm in white, lipid vesicles in cyan, and ^{2}H-SQGem in pink. Scale bars, 10 μm.
Reprinted from D. Sobot, S. Mura, M. Rouquette, B. Vukosavljevic, F. Cayre, E. Buchy, G. Pieters, M. Windbergs, D. Desmaele, P. Couvreur; Circulating lipoprotein: a Trojan horse guiding squalenoylated drugs to LDL-accumulating cancer cells. Mol. Ther. 2017; 25(7):1596-1605, Copyright (2017) American Society of Gene & Cell Therapy (ASGCT), with permission from ASGCT. (120)

Altogether, this chapter describes the *in vitro* uptake of bioinspired squalenoylated nanoparticles into two breast cancer cell lines with different LDL receptors expression levels. In order to detect and visualize the lipid-based nanocarrier systems within the lipid-rich intracellular environment, we applied compound deuterization, to detect the lipid-based carrier within the endogeneous cellular lipids Different particle uptake in two cell lines confirmed the assumption of the LDLR mediated cellular uptake and paved the way for label-free intracellular trafficking of bioinspired advanced therapeutics for selective drug delivery by confocal Raman microscopy.

4   Conclusions and Outlook

This thesis describes the successful application of confocal Raman microscopy (CRM) for label-free and chemically selective characterization and advanced visualization of a large variety of pharmaceutical samples ranging from solid dosage forms, primary cells and their differentiation, up to the cellular interactions with deuterated nanocarrier systems.

The first chapter describes Raman microscopy as a valuable tool for chemical imaging of different classic solid dosage forms, i.e. tablets and pellets, but also electrospun fiber mats as bioinspired functional materials, for investigating the effect of release and degradation on final properties of drug delivery systems. Chemical imaging of component distribution within a pellet, for example, was necessary to understand the drug release mechanism from a coated drug delivery system without any labeling, and to correlate it to drug release profiles in two different media. In the case of in situ drug release investigation from the tablet based on amorphous solid dispersions, CRM allowed for the elucidation of the influence of the polymer properties on the drug form and dissolution mechanisms. Overall, based on Raman analysis, we investigated not only component distribution, but also the underlying mass transport mechanisms upon contact with the dissolution or degradation medium and correlated the dissolution profiles with excipients properties and fabrication processes.

The subsequent chapter introduced CRM for studying the non-cellular pulmonary barrier represented by the human airway mucus in the peripheral lung and alveolar surfactant secreted by the primary human alveolar epithelium. In the first study, we were successfully able to chemically resolve the pulmonary surfactant from the human mucus matrix and show its spatial distribution. In addition, we visualized cysteine-rich domains (-S-S-) within the mucus mesh prior to mucolysis and the reduction of disulfide bonds after incubation with a thiol-based mucolytic agent, N-acetyl cysteine. In the next study, we used the knowledge about the prominent spectral pattern of alveolar surfactant for identification and gradual metamorphosis of primary human alveolar epithelial cells by applying spontaneous Raman and coherent anti-Stokes Raman scattering (CARS) microscopy. Here, gradual morphological and molecular changes during differentiation of alveolar type II (ATII) towards ATI-like cells were correlated to chemically selective Raman spectra. The ATII phenotype was identified based on strong and localized phospholipid vibrations (specifically phosphatidyl choline); however, the ATI-like phenotype yielded spectra with significantly less lipid content and absence of vesicular structures. As the intracellular lipid vesicles generate a strong CARS signal, we applied CARS microscopy for complementary 3D visualization of alveolar surfactant rich vesicles within ATII cells and their secretion upon cell differentiation. Finally, hyperspectral CARS imaging enabled the distinction between cellular proteins and lipids according to their vibrational signatures. Despite the low scattering intensities of the cells, especially flattened ATI-like cells, label-free analysis was pursued effectively without sacrificing chemical selective detection as comparative fluorescence microscopy studies proved.

In the final chapter, we describe the *in vitro* uptake of squalenoylated nanoparticles into two breast cancer cell lines with different LDL receptors expression. Firstly, in order to visualize the lipid-based nanocarrier systems inside of the lipid-rich intracellular environment, we applied deuterization as an approach for increasing the Raman sensitivity of the molecule of interest. Further, the contribution of the LDLR in the cellular uptake of SQGem nanoparticles was investigated on MDA-MB-231 and MCF-7 breast cancer cells, displaying respectively high and low levels of LDLR expression. The use of nanoparticles resulting from the self-assembly of a deuterated SQGem bioconjugates enabled differentiation of the endogenously similar Raman spectra of SQ-based nanoparticles and intracellular lipid droplets due to the unique spectral bands of the deuterium isotope generated in the so called

"silent region" (around 2200 cm^{-1}) in which no significant spectral contributions of other biomacromolecules are observed. After 2h incubation with ^{2}H-SQGem NPs, a significant intracellular accumulation was observed in MDA-MB-231 cells, whereas no NPs were detected in MCF-7 cells under the same conditions. However, after longer incubation times (72 h), both cell lines exhibited a significant uptake of ^{2}H-SQGem NPs, thus confirming the theory of the LDLR mediated uptake.

Although versatile and very promising, confocal Raman microscopy is a challenging analytical tool which requires a complex study design, data post-processing and thorough interpretation. In addition to significant contribution to the formulation design and production of advanced drug delivery systems, the method looks very promising for label-free intracellular trafficking of advanced therapeutics for selective drug delivery.For these purposes, sophisticated multivariate data methods used for spectral post-processing are continuously explored in the field as they enable clarification of delicate spectral changes, especially in a biological system. Moreover, the long acquisition times required for analyzing biological samples due to their low Raman scattering intensity was overcome by applying a non-linear coherent Raman technique.

Altogether, chemical imaging undoubtedly provided important analytical results and enabled a comprehensive investigation of drug delivery systems, complex biological samples, as well the interaction of cells and bioinspired nanocarriers. CRM is successfully proven as a tool for elucidation of complex drug release mechanisms, investigation of the non-cellular lung barrier, as well as for visualization of the particle uptake. As shown in this thesis, confocal Raman microscopy is well-suited for profound analysis of pharmaceutical samples and can support more rational development of novel therapeutics and improved product safety. The application of this versatile method is expected to grow further in the future.

5   Original Publications

5.1   Novel Insights into Controlled Drug Release from Coated Pellets by Confocal Raman Microscopy

Novel insights into controlled drug release from coated pellets by confocal Raman microscopy

B. Vukosavljevic, L. De Kinder, J. Siepmann, S. Muschert, M. Windbergs
J. Raman Spectrosc. **2016**, 47:757-762.

Research article

Novel insights into controlled drug release from coated pellets by confocal Raman microscopy

B. Vukosavljevic,[a,b] L. De Kinder,[c,d] J. Siepmann,[c,d] S. Muschert[c,d] and M. Windbergs[a,b]*

The development of novel therapeutics with improved efficacy implies increasing complexity of drug delivery systems, which in turn require advanced methods for their analytical characterization. Among these systems, pellets represent upcoming carrier systems, which show several advantages like simplified dosing and improved compliance among children and the aged population. However, rational development of such systems is hampered by the lack of non-destructive, chemically selective analytical insight into compound distribution and drug release mechanisms. The aim of this study was to evaluate confocal Raman microscopy (CRM) for investigation of coated drug-loaded pellets based on visualization of compound distribution and elucidation of drug release mechanisms. Three complementary approaches were applied for pellet characterization: analysis of cross sections after bisectioning, non-invasive visualization of the pellet surface, and virtual cross sectioning in x–z direction. As the surface of such pellets is structured, a complementary approach of optical topography and CRM was applied for three-dimensional analysis. Based on the individual Raman peak patterns, the drug and excipients forming the matrix of the pellets and the film coating were successfully visualized with high spatial resolution, verifying homogeneous drug distribution and intact polymer coating of the pellet. Further, analysis of the pellets after certain time intervals during drug release testing revealed pore formation in the polymer coating facilitating drug release and preceding drug depletion in the pellets matrix. CRM represents an upcoming technique for analytical characterization of carrier systems and elucidation of their complex drug release mechanisms, thus supporting rational development of novel therapeutics. Copyright © 2016 John Wiley & Sons, Ltd.

Keywords: Raman imaging; drug delivery systems; pellets; controlled drug release; film coating

Introduction

Because of increasing complexity of pharmaceutical actives coming from the research pipeline and their corresponding therapy schemes, recent development of novel therapeutics requires sophisticated drug delivery systems. Among them, multi-particulate spheres called pellets gain increasing interest for oral delivery via the gastrointestinal tract. In comparison with single-unit delivery systems like tablets or capsules, pellets offer therapeutic advantages allowing for simplified and individual dosing and improved patient compliance, especially for children and elderly.[1] Release of actives incorporated into pellets might be controlled by convective and/or diffusive mass transport throughout the pellet matrix.[2] In addition, pellets can be coated with a polymeric film to create an additional layer for protection and delivery control of the embedded actives.

Even though film coating is an established technology for drug delivery systems providing controlled drug release, detailed mechanistic understanding of drug release processes is not straight forward. Numerous influencing factors have successfully been identified like material of pellet matrix and coating, coating thickness, and so on, which form a complex interplay governing the drug release process. For the elucidation and a better mechanistic understanding of such processes, the application of adequate analytical techniques is very important.

Systematic characterization of drug delivery systems involves spatially resolved analysis of component distribution including the drug(s) and the excipients like matrix formers, coating agents,

and so on, and their changes during drug release. One common analytical method used for physical characterization of drug delivery systems is scanning electron microscopy; however, the technique is operating in vacuum and lacks chemical selectivity. Furthermore, confocal laser scanning microscopy is a powerful technique allowing for spatially resolved and chemically selective analysis; however, because of the required sample manipulation by staining and fixation, the informative value in some cases is questionable, and complementary analytical approaches are needed.[3] In this context, techniques based on vibrational spectroscopy like infrared and near infrared are upcoming analytical tools.[4–9] They provide label-free and chemically selective analysis, but because of the low spatial resolution, visualization of delicate changes, such as

* Correspondence to: Maike Windbergs, Department of Biopharmaceutics and Pharmaceutical Technology, Saarland University, Campus A 4.1, 66123 Saarbruecken, Germany.
  E-mail: m.windbergs@mx.uni-saarland.de

a Helmholtz Centre for Infection Research (HZI) and Helmholtz Institute for Pharmaceutical Research Saarland (HIPS), Department of Drug Delivery, Saarbruecken, Germany

b Department of Biopharmaceutics and Pharmaceutical Technology, Saarland University, Saarbruecken, Germany

c College of Pharmacy, University of Lille, Lille, France

d Controlled Drug Delivery Systems and Biomaterials, INSERM U 1008, Lille, France

depletion of a thin-film coating, is often impossible. An additional problem is that water exhibits a strong absorption in the infrared region, thus hindering analysis during release testing in aqueous medium.

In contrast, confocal Raman microscopy (CRM), as a non-invasive, chemically selective, and spatially resolved analytical technique overcomes some of the aforementioned obstacles thus gaining increasing interest for advanced characterization of drug delivery systems.[10] This method has already been described as a valuable tool for analysis of a broad range of diverse pharmaceutical samples: solid dispersions,[11–14] drug-eluting coatings,[15–17] polymeric microparticles,[18–20] and tablets.[21–23] CRM is utilized for microstructural characterization of drug delivery systems and for better understanding of interactions between different components in formulations. Further, chemical imaging based on Raman spectra has been applied to determine the size distribution of drug microparticles and the drug distribution homogeneity in tablets.[24,25] As a recent example, CRM has revealed that bulk dispersity plays an important role in increased drug release from a coground solid dispersion in a hydrophilic carrier illustrating that the release profile of the drug could greatly be influenced by the spatial distribution of each compound of the formulation.[26] Therefore, Raman microscopy represents an efficient tool for elucidating drug release mechanisms from various dosage forms.[16,27–29] However, samples with highly structured surfaces are challenging for analysis with confocal microscopy techniques, as only one focal plane can be analyzed at a time. As a complementary analytical approach, the combination of CRM and optical topography has already been described as a strategy to overcome this drawback.[30] Optical topography prior to Raman spectroscopy analysis allows three-dimensional mapping of the topographic height differences (topography profile), thus enabling to level the focal plane to the sample surface for acquisition of Raman spectra.

In this study, we evaluated CRM for investigation of coated drug-loaded pellets based on visualization of compound distribution and elucidation of drug release mechanisms. We applied three different sampling approaches: cross sections analysis after bisectioning (*xy*), non-invasive whole pellet visualization (*xy*), and virtual cross sectioning (*xz*). Based on the individual Raman peak patterns, we followed changes in component distribution in the pellet core and changes in the film coating, which occur upon release testing.

Materials and methods

Materials

Verapamil hydrochloride [2-(3,4-dimethoxyphenyl)-5-[2-(3,4-dimethoxyphenyl)ethyl-methylamino]-2-propan-2-ylpentanenitrile;hydrochloride] was obtained from Safic Alcan (Puteaux, France). Lactose monohydrate (Lactochem Fine Powder) was kindly provided by DFE Pharma (Goch, Germant); microcrystalline cellulose (Avicel PH 101) was donated by FMC Biopolymer (Brussels, Belgium). Kollicoat SR 30D (aqueous polyvinyl acetate dispersion) and Kollicoat IR (polyvinyl alcohol-polyethylene glycol graft copolymer) were kind gifts from BASF (Ludwigshafen, Germany).

Preparation of pellets

Pellet starter cores, consisting of 10% verapamil HCl, 45% lactose, 45% microcrystalline cellulose, were prepared by extrusion and subsequent spheronization as follows: The powders were blended in a high shear mixer (Loedige M20; Loedige Paderborn, Germany),

and purified water (approximately 50% w/w, referred to the dry powder mass) was added until a homogeneous mass was obtained. The wetted mixture was passed through a cylinder extruder (Alexanderwerk SK M/R, orifices: 1 mm diameter, rotation speed: 32 rpm; Alexanderwerk, Remscheid, Germany). The extrudates were cut into small cylinders, 3 mm in length. The latter were spheronized at 765 rpm for 30 s (Spheronizer Model 15; Calveva, Dorset, UK) and dried in a fluidized bed (ST 15; Aeromatic LTD, Muttenz, Switzerland) at 30 °C for 30 min. After sieving (keeping the size fraction 710–1250 μm), 500 g of the starter cores were coated in a fluidized bed (Strea 1; Aeromatic-Fielder, Bubendorf, Switzerland), equipped with a Wurster insert. 5 g Kollicoat IR powder was dissolved in 183 g purified water and blended with 150 g of the aqueous dispersion Kollicoat SR 30 D. The blend was stirred for 30 min prior to coating. Gentle stirring was continued throughout the coating process. The process parameters were as follows: inlet temperature 38 ± 2 °C, product temperature 35 ± 4 °C, average spray rate 1.5 g/min, atomization pressure 1.2 bar, and nozzle diameter 1.2 mm. After coating, the pellets were further fluidized for 10 min (but without spraying any formulation) and subsequently cured in an oven for 48 h at 60 °C. The verapamil HCl-loaded starter cores were coated until a weight gain of 10 % (w/w) was achieved.

Confocal Raman microscopy and optical topography

Confocal Raman microscopy and optical topography measurements were performed with a WITec alpha 300R+ (WITec GmbH, Ulm, Germany). The excitation source was a diode laser with a wavelength of 532 nm adjusted to a power of 10 mW for cross sections (*xy*) and 40 mW for virtual cross sections (*xz*). Objectives with 10× (N.A. 0.25) and 50× (N.A. 0.55) magnification (Epiplan Neofluar, Zeiss, Germany) were applied. The lateral resolution was 1.1 μm for the 10× and 0.5 μm for the 50× objective, respectively. The axial resolution was 3.1 μm when using the 50× objective. A confocal pinhole of 50 μm rejected signals from out-of-focus regions. Raman spectra of the pure compounds were acquired with an integration time of 0.5 s and ten accumulations. Image scans of the samples were recorded with integration times from 0.1 to 0.5 s every 2–10 μm along the *x*-axis and *y*-axis and 0.5 s every 1 μm along *z*-axis. All spectra were background subtracted, normalized to the most intense peak, and converted into false color images using WITec PROJECT PLUS software (WITec GmbH, Ulm, Germany). Image pixels assigned to verapamil hydrochloride spectra are depicted in red, microcrystalline cellulose and lactose in blue (matrix), whereas pixels assigned to Kollicoat IR® and Kollicoat SR® appear in yellow.

Results and discussions

Pellets were fabricated with verapamil hydrochloride, a calcium channel blocker frequently used in the therapy of hypertension, angina pectoris, cardiac arrhythmia, and in preventive medication for migraine.[31] Verapamil hydrochloride was used as a model drug as it exhibits a pH-dependent release behavior from drug delivery systems because of its weak base characteristics.

Pellets were prepared by extrusion–spheronization based on a mixture of verapamil hydrochloride with cellulose and lactose; the latter ones form a matrix in which the drug (10% w/w loading) is embedded. The core was subsequently coated in a fluidized bed setup with a Kollicoat SR®/Kollicoat IR® 90:10 (w/w) mixture to control drug release from the pellet core. A schematic illustration of a

single pellet, where the drug is depicted in red, the matrix in blue and the film coating in yellow is presented in Fig. 1(A). Pellets analyzed in this study were around 1 mm in diameter (Fig. 1(B)). Initially, we were aiming for determination of suitable peaks for identification of individual pellet compounds. We successfully differentiated between excipients in the pellet matrix, drug, and film coating based on their Raman spectra as depicted in Fig. 1(C). Figure 1(D) represents raw Raman spectra of three different spots of a pellet cross section based on which the individual compounds can be identified in a spatially resolved manner. Spectrum 1 represents the coating, spectrum 2 verapamil hydrochloride, and spectrum 3 a mixture of lactose and cellulose, respectively.

The structured surface of the pellet, for the intact pellet and for the cross section, impedes all-encompassing analysis with a confocal microscope. In this context, some invasive methods of sample preparation, for example polishing, could be employed prior to Raman analysis in order to create a smooth sample surface. As this could severely change the original compound distribution, we avoided this invasive approach by combining CRM with optical topography. This complementary procedure has been proven to be beneficial for imaging of drug delivery systems with structured surfaces.[30] It involves optical topography analysis of a certain area of interest prior to Raman microcopy investigation. Subsequently, acquisition of the Raman spectra is guided by the profilometry information, so the microscope focus is individually adjusted according to the sample topography. Therefore, the focal plane is positioned at the sample surface at each measurement point, which is needed for chemically selective characterization. The topography map of the pellet cross section confirms the structured surface of the pellet after cutting (Fig. 2(A)). Guided by the topography map, a Raman spectral data set is recorded and subsequently converted into a false color image, where each component is represented by a different color. Localization of drug, excipients forming the matrix, and film coating compounds of the pellet cross section were successfully visualized with high spatial resolution (10 μm step size). Image pixels assigned to verapamil (drug) are depicted as red, the matrix excipients (cellulose and lactose) as blue, whereas pixels assigned to the coating film composed of two polymers (Kollicoat SR® and Kollicoat IR®) are represented by yellow.

We applied hierarchical cluster analysis and basis analysis as two different multivariate methods for data processing. The image of the cross section, after applying cluster analysis, illustrates homogeneous drug distribution within the pellet matrix (10% drug loading) and the polymer film coating (Fig. 2(B)). Raman images of the marked area in Fig. 2(A) with a higher spatial resolution (3 μm step size) are created with applying either hierarchical cluster analysis (Fig. 2(C)) or basis analysis (Fig. 2(D)) as a comparison. Cluster analysis involves a binary approach resulting into Boolean images. Each pixel is explicitly assigned to one of the clusters, which represent the different chemical compounds of the pellet visualized by different colors (Fig. 2(C)).

In contrast, basis analysis involves Raman spectra of the individual compounds acquired from the sample as references. The false color image depicts the relative congruence of the spectra with the predefined reference spectra for each pixel. This approach is not binary and allows for a simultaneous weighted display of multiple components in one single pixel as visualized by color intensity differences (Fig. 2(D)). This sophisticated multivariate methodology provides a more detailed visualization of the compound distribution, as can be demonstrated by comparing Figs 2(C and D). After basis analysis, even individual particles can be differentiated within the pellet. CRM can also be used as a valid approach for particle size
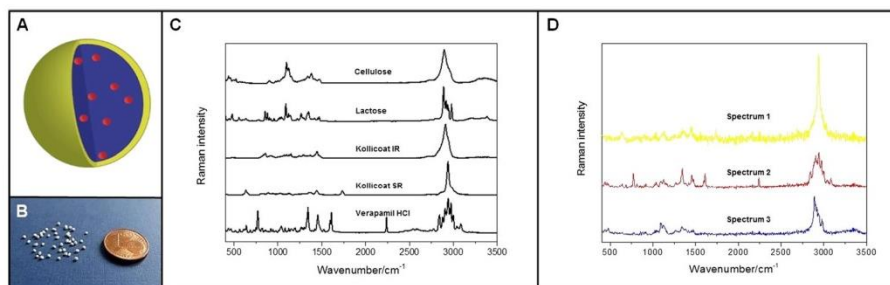
Figure 1. (A) Schematic illustration of a single pellet; (B) Photograph of pellets; (C) Raman spectra of individual compounds: cellulose and lactose (matrix – blue), Kollicoat IR® and Kollicoat SR® (film coating – yellow), and verapamil hydrochloride (drug – red); (D) Raman spectra of three different spots of a pellet (according to the color coding in (A)).
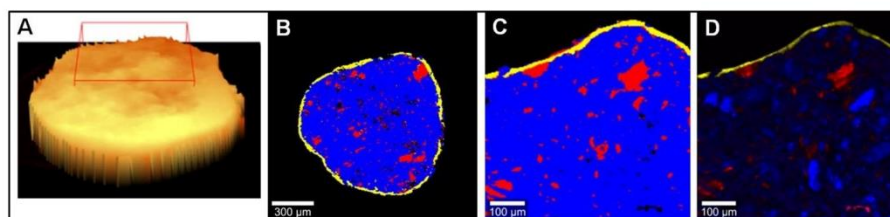

Figure 2. (A) Surface topography of a pellet cross section (after bisectioning) with marked area chosen for Raman imaging; (B) Raman image of the pellet cross section; (C) and (D) Raman images of the small area of the pellet with higher resolution, after application of hierarchical cluster (C) and basis (D) analysis. False colors depict the matrix excipients in blue, the film coating in yellow, and the drug in red, respectively.

analysis[26,32]; however, in this study, particle size distribution was not in the focus of interest.

However, upon bisectioning, pellets were exposed to mechanical stress, which can dramatically affect the original sample state and influenced the analytical results. Potential bisectioning-related challenges include partial dislocation and disruption as well as defects of the coating layer. Figure 3 shows examples for defects and dislocation, which might be the result of bisectioning. As it is unfeasible to differentiate between defects occurred upon fabrication and sample preparation, film coating thickness measurements and elucidation of the drug release mechanisms could be affected. Consequently, non-invasive methods became necessary for investigation of the coating integrity.

Release testing of pellets serves to evaluate the release of the incorporated drug from the matrix. Release occurs upon contact with the release medium, which simulates gastric and intestinal fluids in the human body. Depending on the pH value of the release medium, the environment of the stomach or different parts of the intestine can be simulated. The pH value might influence the drug release and the degradation of the film coating because of the pH-dependent solubility of certain drugs and excipients.

Based on topography analysis, the pellet surface could be visualized, and guided by such a topography profile, it is possible to focus on the pellet surface upon Raman scanning (Fig. 4(A)). Peak patterns of the film coating were converted into false color images and different intensities of the yellow color originated from differ-
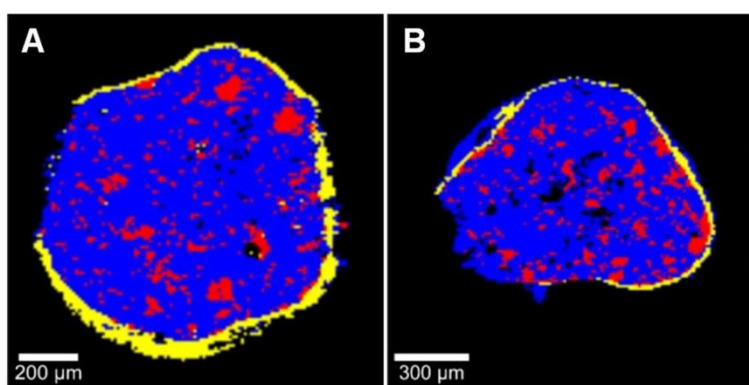
Figure 3. Raman images of cross sections with defect (A) and dislocation (B) of the coating, which might result from the cutting during sample preparation. False colors depict the matrix excipients in blue, film coating in yellow, and the drug in red, respectively.
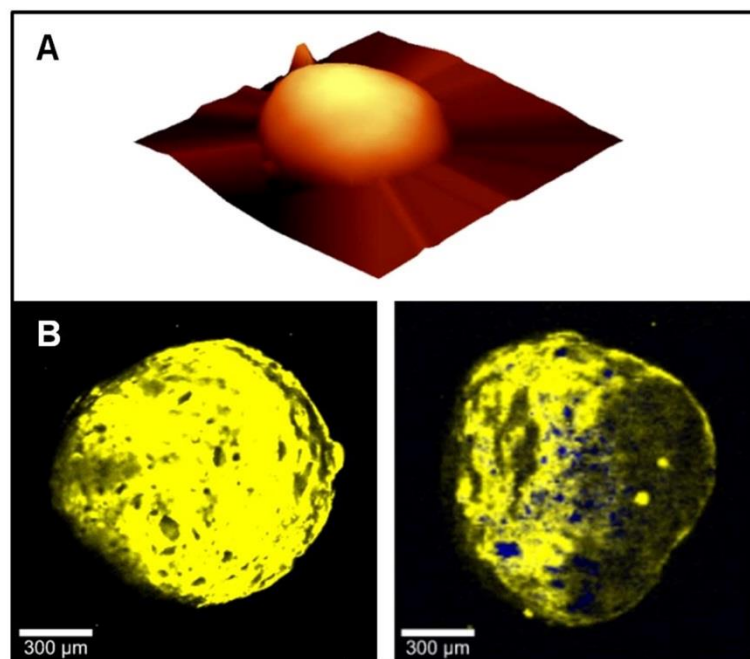
Figure 4. (A) Optical topography of an intact pellet; (B) Raman images of pellets before and after release testing. False colors depict the matrix excipients in blue and film coating in yellow.

Novel insights into drug release from coated pellets by confocal Raman microscopy
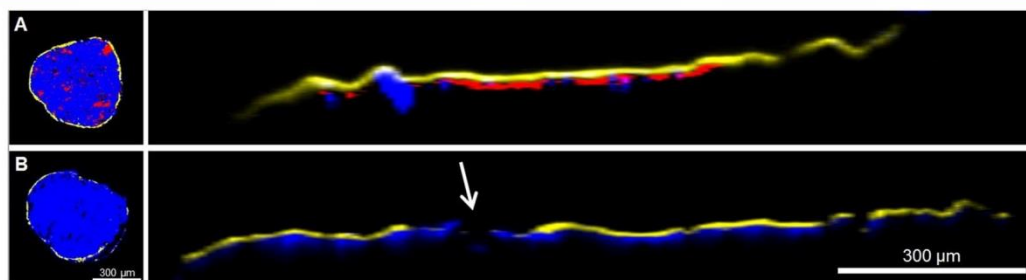
Figure 5. Cross sections and virtual cross sections of pellets before (A) and after release testing (B). False colors depict the matrix excipients in blue, film coating in yellow, and the drug in red, respectively.

ent Raman signal intensities allowing for three-dimensional visualization of the pellet surface. The Raman image demonstrates the intactness and coherence of the coating layer before release testing (Fig. 4(B)). However, after the release testing, certain parts of the film coating were no longer intact, and the Raman signal of the pellet core (matrix excipients depicted in blue) was detectable.

This could be explained by leaching of the immediate release polymer (Kollicoat IR®) from the coating film upon contact with the release medium, thus leaving pores in the coating layer based on the remaining Kollicoat SR®, which was not soluble in the release medium. Despite its usefulness for non-invasive visualization of the pellet surface, this approach does not allow for tracking the changes in the pellet core upon release testing.

Therefore, we applied virtual cross sectioning in x–z direction (depth scans) for non-invasive visualization of all pellet compounds as a third approach. The penetration depth of the laser through slightly transparent media (as the pellet) is nevertheless limited. Increasing the laser power allows for higher penetration depth; however, the applied laser power is limited by potential sample damage. In the present study, virtual cross sections were successfully acquired with an argon green laser (532 nm excitation wavelength); the laser power was up to 40 mW, reaching a penetration depth of up to 200 μm within the pellet. Depending on the depth of the scan, the film coating and the matrix with embedded drug particles could successfully be visualized. We again analyzed pellets before and after release testing to gain deeper and spatially resolved insight into release processes and changes within the film coating and the pellet core upon contact with the release medium. Both, virtual cross sections and cross sections after bisectioning, allowed for visualization of the film coating, matrix excipients, and the drug. Before release testing, we detected an intact coating layer as well as the matrix excipients and the drug beneath it, as depicted in Fig. 5(A). Clearly, virtual cross sections confirmed pore formation within the film coating upon release testing, probably because of the dissolving Kollicoat IR®. We were able to non-invasively visualize the pore formation (marked with an arrow) within the coating layer and drug depletion from the matrix because of contact with the release medium, as shown in Fig. 5(B).

These pores allow for more rapid drug transport from the inner core of the pellet upon contact with a fluid, thus likely playing a crucial role in controlling drug release from the coated pellet. In addition, there was no drug detectable close to the pellet surface any more, illustrating complete drug release from these regions. This corroborates that non-invasive analysis, virtual cross sections and visualization of the pellet surface, is a good complementary approach to bisectioning for comprehensive analysis of pharmaceutical solid dosage forms like the investigated pellets.

Conclusions

Confocal Raman microscopy is an upcoming analytical tool for comprehensive characterization of complex drug delivery systems like coated pellets ranging from analysis of compound distribution and film coating thickness up to elucidation of complicated drug release mechanisms. Using three different imaging approaches, it was possible to investigate the underlying mass transport mechanisms of the drug from the pellet matrix and to visualize the pore formation within the film coating after contact with the release medium. These pores are likely important for the control of drug release from the investigated pellets coated with the polymer mixture. Consequently, confocal Raman microscopy was successfully proven as a versatile technique for analytical characterization of carrier systems and better understanding of their complex drug release mechanisms, thus supporting rational development of novel therapeutics and improve product safety.

References

[1] M. Brunner, R. Greinwald, K. Kletter, H. Kvaternik, M. E. Corrado, H. G. Eichler, M. Müller, *Aliment. Pharmacol. Ther.* **2003**, *17*, 1163.
[2] B. Dekyndt, J. Verin, C. Neut, F. Siepmann, J. Siepmann, *Int. J. Pharm.* **2015**, *478*, 31.
[3] S. R. Pygall, J. Whetstone, P. Timmins, C. D. Melia, *Adv. Drug Deliv. Rev.* **2007**, *59*, 1434.
[4] R. Lyon, D. Lester, E. N. Lewis, E. Lee, L. Yu, E. Jefferson, A. Hussain, *AAPS PharmSciTech* **2002**, *3*, 1.
[5] J. Cruz, M. Bautista, J. M. Amigo, M. Blanco, *Talanta* **2009**, *80*, 473.
[6] P. S. Wray, G. S. Clarke, S. G. Kazarian, *J. Pharm. Sci.* **2011**, *100*, 4745.
[7] A. Heinz, C. J. Strachan, K. C. Gordon, T. Rades, *J. Pharm. Pharmacol.* **2009**, *61*, 971.
[8] P. Avalle, S. R. Pygall, N. Gower, A. Midwinter, *Eur. J. Pharm. Sci.* **2011**, *43*, 400.
[9] S. Sasic, Y. Ozaki, *Raman, infrared, and near-infrared chemical imaging*, John Wiley & Sons, Inc., Hoboken, New Jersey, **2011**.
[10] G. P. Smith, C. M. McGoverin, S. J. Fraser, K. C. Gordon, *Adv Drug Deliv Rev*, **2015**, *89*, 21.
[11] J. Breitenbach, W. Schrof, J. Neumann, *Pharm. Res.* **1999**, *16*, 1109.
[12] B. Vajna, H. Pataki, Z. Nagy, I. Farkas, G. Marosi, *Int. J. Pharm.* **2011**, *419*, 107.
[13] Z. K. Nagy, A. Balogh, B. Vajna, A. Farkas, G. Patyi, A. Kramarics, G. Marosi, *J. Pharm. Sci.* **2012**, *101*, 322.
[14] F. Tres, K. Treacher, J. Booth, L. P. Hughes, S. A. C. Wren, J. W. Aylott, J. C. Burley, *J. Control. Release* **2014**, *188*, 53.
[15] K. M. Balss, F. H. Long, V. Veselov, A. Orana, E. Akerman-Revis, G. Papandreou, C. A. Maryanoff, *Anal. Chem.* **2008**, *80*, 4853.
[16] J. Dong, J. D. Foley, C. D. Frethem, R. A. Hoerr, M. J. Matuszewski, J. E. Puskas, G. Haugstad, *Langmuir* **2009**, *25*, 5442.
[17] K. B. Biggs, K. M. Balss, C. A. Maryanoff, *Langmuir* **2012**, *28*, 8238.
[18] W. Doub, W. Adams, J. Spencer, L. Buhse, M. Nelson, P. Treado, *Pharm. Res.* **2007**, *24*, 934.
[19] E. Widjaja, W. L. Lee, S. C. J. Loo, *Anal. Chem.* **2010**, *82*, 1277.

B. Vukosavljevic *et al.*

[20] K. Rizi, R. J. Green, O. Khutoryanskaya, M. Donaldson, A. C. Williams, *J. Pharm. Pharmacol.* **2011**, *63*, 1141.

[21] M. J. Henson, L. Zhang, *Appl. Spectrosc.* **2006**, *60*, 1247.

[22] Slobodan, *Appl. Spectrosc.* **2007**, *61*, 239.

[23] M. N. Slipchenko, H. Chen, D. R. Ely, Y. Jung, M. T. Carvajal, J. X. Cheng, *Analyst* **2010**, *135*, 2613.

[24] P. -Y. Sacré, P. Lebrun, P. -F. Chavez, C. D. Bleye, L. Netchacovitch, E. Rozet, R. Klinkenberg, B. Streel, P. Hubert, E. Ziemons, *Anal. Chim. Acta* **2014**, *818*, 7.

[25] A. Kuriyama, Y. Ozaki, *AAPS PharmSciTech* **2014**, *15*, 375.

[26] C. Muehlenfeld, B. Kann, M. Windbergs, M. Thommes, *J. Pharm. Sci.* **2013**, *102*, 4132.

[27] E. Kang, H. Wang, I. K. Kwon, J. Robinson, K. Park, J. -X. Cheng, *Anal. Chem.* **2006**, *78*, 8036.

[28] M. Windbergs, M. Haaser, C. M. McGoverin, K. C. Gordon, P. Kleinebudde, C. J. Strachan, *J. Pharm. Sci.* **2010**, *99*, 1464.

[29] D. H. Choi, K. H. Kim, J. S. Park, S. H. Jeong, K. Park, *J. Control. Release* **2013**, *172*, 763.

[30] B. Kann, M. Windbergs, *AAPS J.* **2013**, *15*, 505.

[31] M. A. Koda-Kimble, B. K. Alldredge, R. L. Corelli, M. E. Ernst, *Koda-Kimble and Young's applied therapeutics: the clinical use of drugs*, Lippincott Williams & Wilkins, Philadelphia, **2012**.

[32] S. Schrank, B. Kann, M. Windbergs, B. J. Glasser, A. Zimmer, J. Khinast, E. Roblegg, *J. Pharm. Sci.* **2013**, *102*, 3987.

Copyright © 2016 John Wiley & Sons, Ltd.

5.2   Non-Invasive Insight into the Release Mechanisms of a Poorly Soluble Drug from Amorphous Solid Dispersions by Confocal Raman Microscopy

Non-invasive insight into the release mechanisms of a poorly soluble drug from amorphous solid dispersions by confocal Raman microscopy

K. Puncochova*, B. Vukosavljevic*, J. Hanus, J. Beranek, M. Windbergs, F. Stepanek

* These authors contributed equally to this work.

Research Paper

Non-invasive insight into the release mechanisms of a poorly soluble drug from amorphous solid dispersions by confocal Raman microscopy

Kateřina Punčochová [a,d,1], Branko Vukosavljevic [b,c,1], Jaroslav Hanuš [a], Josef Beránek [d], Maike Windbergs [b,c,*], František Štěpánek [a,*]

[a] Department of Chemical Engineering, University of Chemistry and Technology Prague, Prague 6, Czech Republic
[b] Department of Biopharmaceutics and Pharmaceutical Technology, Saarland University, Saarbruecken, Germany
[c] Helmholtz Centre for Infection Research (HZI) and Helmholtz-Institute for Pharmaceutical Research Saarland (HIPS), Department of Drug Delivery, Saarbruecken, Germany
[d] Zentiva, k.s., U Kabelovny 130, Prague 10, Czech Republic

ABSTRACT

In this study, we investigated the release mechanism of the poorly water soluble drug aprepitant from different amorphous solid dispersions using confocal Raman microscopy (CRM). Solid dispersions were fabricated based on either Soluplus®, as an amphiphilic copolymer and solubilizer, or on polyvinylpyrrolidone, as a hydrophilic polymer, in order to elucidate the influence of the polymer characteristics on the drug form and dissolution mechanisms. Aprepitant exhibited its amorphous form in both solid dispersions. However, the release differed depending on the polymer. The high complexation effect of Soluplus was shown to be a crucial factor for stabilization of the amorphous drug, resulting in continuous release without any recrystallization of aprepitant. In contrast, solid dispersions based on polyvinylpyrrolidone showed a different mechanism of dissolution; due to the good affinity of PVP and water, the polymer is dissolving fast, leading to phase separation and local recrystallization of the drug. The study highlights the complexity of release processes from solid dispersions and elucidates the influence of the polymer on drug release kinetics.

© 2016 Elsevier B.V. All rights reserved.

1. Introduction

As many novel drugs emerging from the research pipeline exhibit low aqueous solubility, formulation development is frequently challenged with finding effective approaches to increase drug release and absorption via the oral application route. In this context, there are several possibilities that rely either on crystalline (e.g. co-crystals [1]) or on stabilized amorphous form of drug. Amorphization approaches include the formation of solid dispersions [2], sorption on mesoporous carriers [3,4], lipid formulations [5], or co-amorphous systems [6]. The formation of an amorphous solid dispersion is one of the most popular and successful approaches, based on the incorporation of a poorly soluble amorphous drug in a glassy polymer matrix using hot melt extrusion or solvent evaporation (spray drying) [7–11]. In such systems, particle size reduction on the one hand [12] and improved wettability

of the poorly soluble drug on the other hand facilitate the release as well as the dissolution process [13,14]. However, despite such obvious advantages, solid dispersions are susceptible to thermodynamical instabilities, resulting in recrystallization (nucleation and crystal growth) of the drug during storage or dissolution [16]. In amorphous solid dispersions, crystallization of the drug is generally preceded by phase separation and formation of a drug enriched amorphous phase. Thus, for the development of stable amorphous solid dispersions, the ability of the polymer matrix to incorporate and stabilize a homogeneously dispersed amorphous drug at different concentrations is crucial [17].

For release processes of drugs embedded in solid polymer dispersions which can form hydrogels, the drug is released into a highly viscous polymer matrix and can form a locally supersaturated solution during the intestinal transit time. Drug recrystallization in such a system is influenced by multiple factors like the degree of supersaturation and the interfacial energy between crystal nuclei and solvent [15]. However, the exact release mechanisms are in most cases still poorly understood. Pharmaceutical approaches to prevent precipitation include increasing the viscosity of the system, improving solvation of the dissolved drug molecules and decreasing the cluster-liquid interfacial energy [18]. Also,

anti-plasticizing effects of polymers and surfactants are used for the prevention of precipitation and aggregation [19]. From a pharmaceutical perspective, the selection of suitable excipients with the potential to inhibit any tendencies for recrystallization is extremely important [20,21].

Our aim was to understand drug release and recrystallization mechanisms of aprepitant as a poorly soluble drug from amorphous solid dispersions. We used two different types of polymer matrices, Soluplus, an amphiphilic copolymer and solubilizer, and polyvinylpyrrolidone, a hydrophilic polymer, and studied their effect on dissolution mechanisms and recrystallization from amorphous solid dispersions. Raman spectroscopy has been shown to be a useful tool for investigating the dissolution mechanism, crystallization, and phase transformation of drug in real time [22]. Raman spectroscopy for solid form identification is usually performed as surface mapping. The molecular state changes of the solid dispersion during the dissolution test can be measured with *in situ* Raman imaging from the surface of tablet [23,24]. In our study, a confocal Raman microscope was used for the investigation of the phase behavior, separation of phases and recrystallization on a molecular level using depth profiling for visualizing the changes through the gel layer. Moreover, the nucleation and crystal growth of crystalline drug after recrystallization during dissolution were investigated.

2. Materials and methods

2.1. Materials

The drug aprepitant (3-{[[(2R,3S)-2-[(1R)-1-[3,5-bis(trifluoromethyl)phenyl] ethoxy]-3-(4-fluoro-phenyl)morpholin-4-yl]methyl}-4,5-dihydro-1H-1,2,4-triazol-5-one) was kindly provided by Zentiva, k.s. (Prague, Czech Republic). Aprepitant is a poorly soluble drug (II category) according to the Biopharmaceutics Classification System (BCS) criteria; two different polymers were used as matrix materials for the amorphous solid dispersions. Polyvinylpyrrolidone K30 (PVP), obtained from BASF (Germany), is a water soluble polymer with a molecular weight of 30,000 g/mol. Soluplus (polyvinyl caprolactam–polyvinyl acetate–polyethylene glycol graft copolymer), obtained from BASF (Germany), is an amphiphilic, solubility enhancing excipient with an average molecular weight of 118,000. The chemical structures are illustrated in Fig. 1.

2.2. Preparation of solid dispersions

Solid dispersions were prepared by spray drying. Aprepitant (0.5–1.0 g) was dissolved in ethanol (150 ml), the solution was mixed at 40 °C for about 15 min, and the required amount of polymer was then added to achieve a drug:polymer ratio of 1:3 w/w on a dry basis. The solution was spray dried using the Mini Spray Dryer B-290 (Büchi, Switzerland) with an inert nitrogen loop. The temperature inside the drying chamber was kept at 87–88 °C. The spray-dried particles were subsequently compressed to tablets (140 mg) at a compression force 8 kN with a round flat shape and with 7 mm in diameter.

2.3. Differential scanning calorimetry

Glass transition temperatures were measured by modulated temperature differential scanning calorimetry (MTDSC) immediately after preparation. DSC measurements were performed on a TA Instruments, Discovery DSC. The samples were weighed in aluminum pans and covered (40 μl) and measured in a nitrogen flow. Investigations were performed in a temperature range of 0–300 °C with a heating rate of 5 °C/min (Amplitude = 0.8 °C a Period = 60 s). The weight sample was about 4–5 mg.

2.4. Scanning electron microscopy

The particle shape and surface characteristics of the solid dispersions were examined by scanning electron microscopy (SEM) (JMC-5700, Jeol, Japan) operating at 20 kV after sputter-coating with gold (Emitech K550X).

2.5. Dissolution testing

In vitro dissolution testing was performed according to the United States Pharmacopeia (USP) type I. The dissolution profile was measured with baskets at 100 rpm in 150 ml of distilled water at room temperature, using 140 mg tablets compacted at 6.30 kN from the spray-dried powder. The concentration of aprepitant in the solution was determined using HPLC at sampling intervals ranging from 30 min to 120 min for a period of up to 960 min.

2.6. Confocal Raman microscopy

Confocal Raman microscopy (CRM) studies were performed using a WITec alpha 300R$^+$ microscope (WITec GmbH, Ulm, Germany) at an excitation wavelength of 785 nm (operated at laser power of 50 mW) with an integration time of 0.5 s. Surface area scans were performed with a 0.5 μm step size using a 100× objective. Optical topography analysis was applied prior to Raman measurements.

2.7. Dissolution imaging

In situ dissolution behavior of aprepitant from amorphous solid dispersions in a liquid medium was investigated using confocal Raman microscopy. Virtual cross section images (*x–z*) were recorded with a 63× objective to investigate dissolution behavior and distribution of drug and polymer upon dissolution with the following parameters: *x–z* scans (100 μm × 100 μm), step size of 2 and 5 μm along the *x-* and *z*-axes, respectively, and an integration time of 0.5 s. Subsequently, the spectral data sets were corrected for background and cosmic ray signals and processed by multivariate data analysis (cluster and basis analysis) and converted into false-color images using WITec Project Plus software (WITec GmbH, Ulm, Germany).

2.8. Visualization of precipitated crystals

The crystals arising from the recrystallization process were characterized by means of an inverted optical microscope (Olympus CK40) and a laser scanning confocal laser scanning microscope – CLSM (Olympus Fluoview FV1000). The top layer of the gel was removed from the tablet after 100 min of dissolution when aprepitant had precipitated and the presence of crystals was ensured. The removed gel was suspended in water containing diethylaminocoumarin (DEAC) fluorescence dye, incubated for a few minutes and then several drops of the sample were observed by CLSM. Raman imaging of the tablet surface was applied to observe drug precipitation and crystal growth during dissolution. By focusing on the exact surface of the tablet (tablet swells upon dissolution), *x–y* surface area scans (10 × 10 μm), with 0.5 μm step size using 63 × immersion objective were performed.

3. Results and discussion

3.1. Solid state characterization of the solid dispersions

Solid dispersions based on aprepitant with either Soluplus or PVP as polymers were successfully prepared exhibiting homoge-
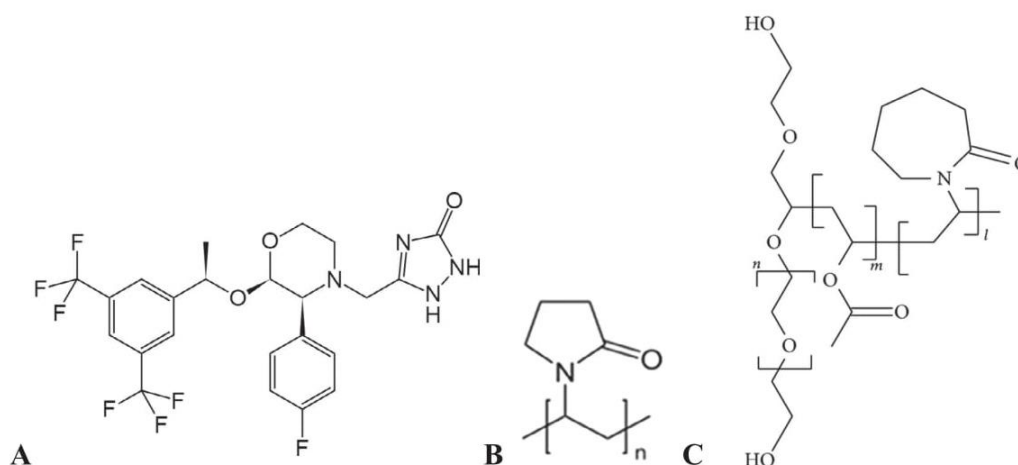
Fig. 1. Chemical structures of (A) Aprepitant, (B) PVP, and (C) Soluplus®.

neous optical appearance. The formation of solid solutions with the drug molecularly dispersed in the polymer matrix was confirmed by DSC analysis. The glass transition temperature of pure Soluplus was 68.2 °C, whereas the solid dispersion with aprepitant resulted in a significant decrease of the glass transition temperature to 57.8 °C. Similarly, the combination of aprepitant with PVP resulted in a glass transition temperature of 159.5 °C for the pure polymer and 142.9 °C for the solid solution with aprepitant. For comparison, the glass transition temperature of pure spray-dried aprepitant was 93.3 °C. In a previous study [25], the amorphous nature of the solid dispersions was confirmed by X-ray powder diffraction (XRPD) and the water vapor sorption was investigated for the powdered polymer as well as for the solid dispersions. PVP exhibited a mass increase of 87.7% at 95% RH for the pure polymer, which was significantly reduced to a 56.6% mass increase for the solid solution due to the hydrophobic nature of aprepitant. For Soluplus, the same effect could be detected at a lower level (37.6% mass increase for the polymer and 20.9 % mass increase for the solid dispersion, respectively) [25].

For morphological characterization, scanning electron microscopy analysis was performed on the multi-particulate solid solutions. Both samples consisted of spherical particles with a size distribution between 2 μm and 10 μm which is illustrated in Fig. 2A. In a next step, the particles were compressed to tablets. In addition to SEM, tablets were analyzed using CRM after bisectioning (Fig. 2B). Raman spectra were acquired every 0.5 μm along *x*-axis and *y*-axis. For both formulations, all Raman spectra contained patterns specific for the drug and the polymer, demonstrating homogeneous distribution of the drug in the polymer matrix. Blue color in Raman false color images indicated mixed spectra of both compounds, aprepitant and Soluplus, as well as aprepitant and PVP.

3.2. In vitro dissolution testing

The cumulative release profiles of aprepitant from amorphous solid dispersions in Soluplus and PVP are shown in Fig. 3. The release from the Soluplus matrix is rather slow but steady, and follows a linear dependence of concentration on time. Visual observation confirmed that the tablets swell during dissolution but they are not eroded. Soluplus creates a highly viscous gel, which was not dissolved over the timescale of the experiment and acted as diffusion barrier for aprepitant. On the other hand, the quantity of aprepitant released from the PVP matrix was higher compared

to the Soluplus matrix until 480 min. This was mainly due a higher release rate during the first 60 min; between 60 min and 480, the slopes of the release curves from both matrices were similar. However, after approx. 480 min aprepitant precipitates and its bulk concentration starts to decrease (Fig. 3). Unlike Soluplus, the swollen PVP matrix was susceptible to erosion and eroded parts of the tablet were found in the bulk dissolution medium. The release profile in the case of PVP implies the solution was supersaturated with respect to the API, which started to re-crystallize after approx. 450 min. In order to estimate the extent of supersaturation, the equilibrium solubility of aprepitant in both PVP and Soluplus solutions at several polymer concentrations, namely, 200, 400 and 800 mg/l was measured, and found to be below 0.20 mg/l (detection limit of the HPLC method) in all cases, except for the highest concentration of Soluplus (800 mg/l) where the equilibrium solubility of aprepitant was 1.31 mg/l. Note that the polymer concentration of 800 mg/l would correspond to complete dissolution of the tablet under the conditions of the dissolution test shown in Fig. 3. Overall, this means that the release curves shown in Fig. 3 have entered the supersaturated region not only for PVP, but also for Soluplus.
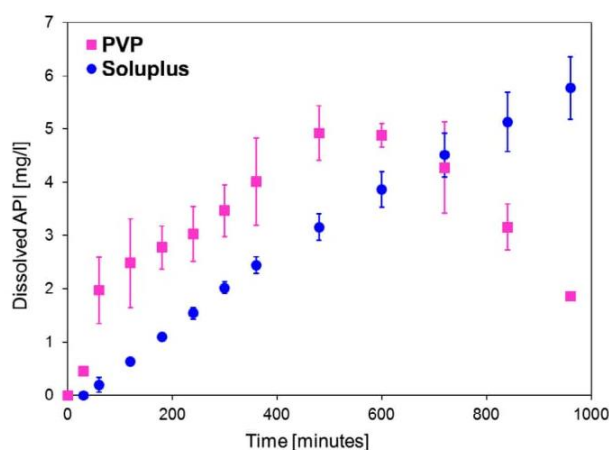
Even though the difference in release kinetics is obvious, accurate understanding of the release mechanism based on the release profiles alone is not possible. Previous analysis by ATR-FTIR spectroscopic imaging indicated that local precipitation of aprepitant could take place in the case of dissolution from the PVP formulation [26]. However, direct visualization or quantification of the crystalline phase was not pursued since crystal growth could be affected by the physical contact of the tablet surface with the ATR imaging crystal [26]. Thus, in a next step, we applied confocal Raman microscopy for non-invasive *in situ* analysis of the release and recrystallization processes directly in the dissolution medium.

3.3. In situ Raman imaging during dissolution

Confocal Raman microscopy was applied to simultaneously track the different compounds of the amorphous solid dispersions (drug and polymer) and their physical changes during dissolution testing. Tablets prepared from the two solid dispersions were immersed in purified water as a release medium and non-invasive virtual cross sections were taken during the release process at laboratory temperature. Differentiation of the different compounds was achieved based on their individual Raman spectra as depicted in Fig. 4. Unique bands used for the differentiation of
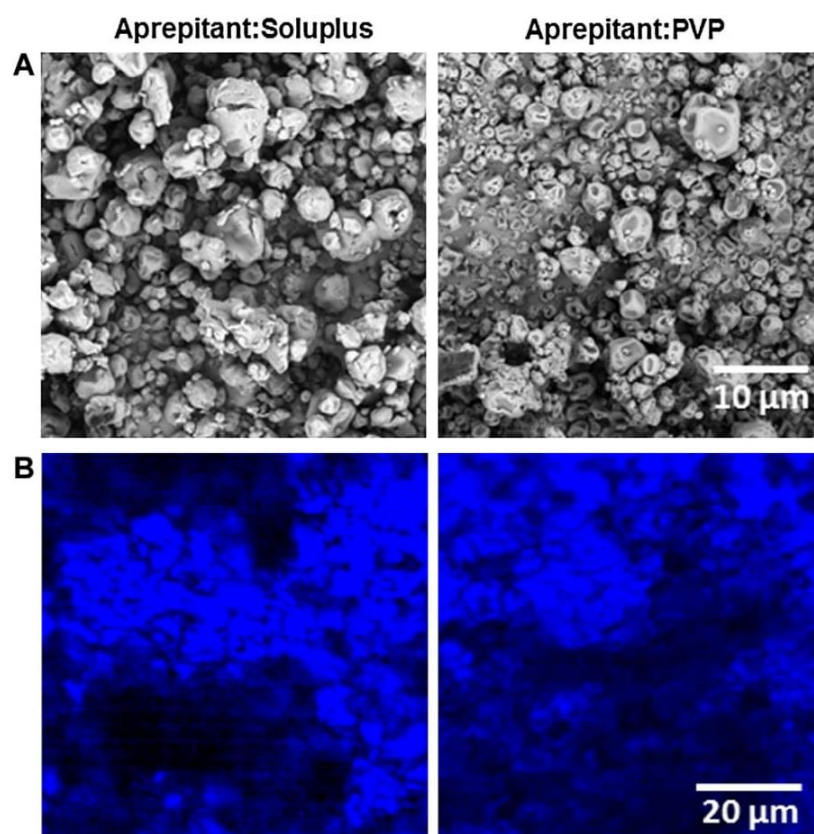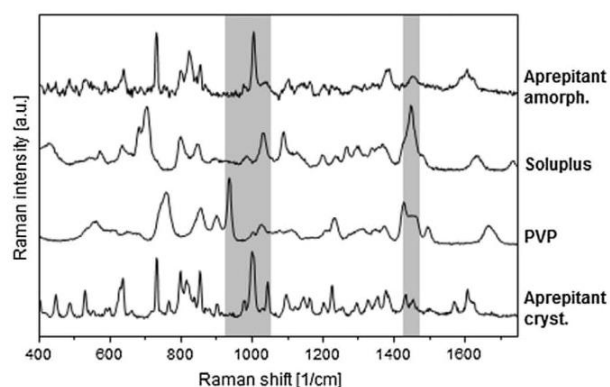
Fig. 2. (A) SEM micrographs of spray-dried particles, (B) Raman false color images of tablet surface after bisecting, acquired with 0.5 μm step size. Blue color indicates mixed spectrum of both compounds, aprepitant and Soluplus, as well as aprepitant and PVP. (For interpretation of the references to colour in this figure legend, the reader is referred to the web version of this article.)

Fig. 3. Cumulative release profiles of aprepitant from tablets compressed of spray-dried particles of amorphous solid dispersions of aprepitant in Soluplus and PVP.

Fig. 4. Raman spectra of individual compounds (bands for identification are highlighted).

amorphous drug, crystalline drug, Soluplus and PVP were $1005\,cm^{-1}$, $1047\,cm^{-1}$, $1450\,cm^{-1}$ and $935\,cm^{-1}$, respectively. The Raman spectra of amorphous solid dispersions show distinctive peaks which belong to both components, drug and polymer, in a homogeneous mixture without any evidence of crystalline aprepitant.

Based on spatially resolved spectral information of the tablets during dissolution testing, CRM allows for non-destructive and chemically selective analysis of distribution changes within the amorphous solid dispersions during dissolution. In order to preserve the intactness of the samples we applied virtual cross section imaging (x, z direction). For each of the measurements, we initially focussed on the tablet surface and let the laser penetrate into the sample down to a depth of around 20 μm. Raman false color images of a tablet compressed from aprepitant:Soluplus spray-dried particles did not indicate any phase separation or recrystallization processes during the dissolution testing (Fig. 5A). In contrast, for the aprepitant:PVP matrix, PVP is rapidly dissolving
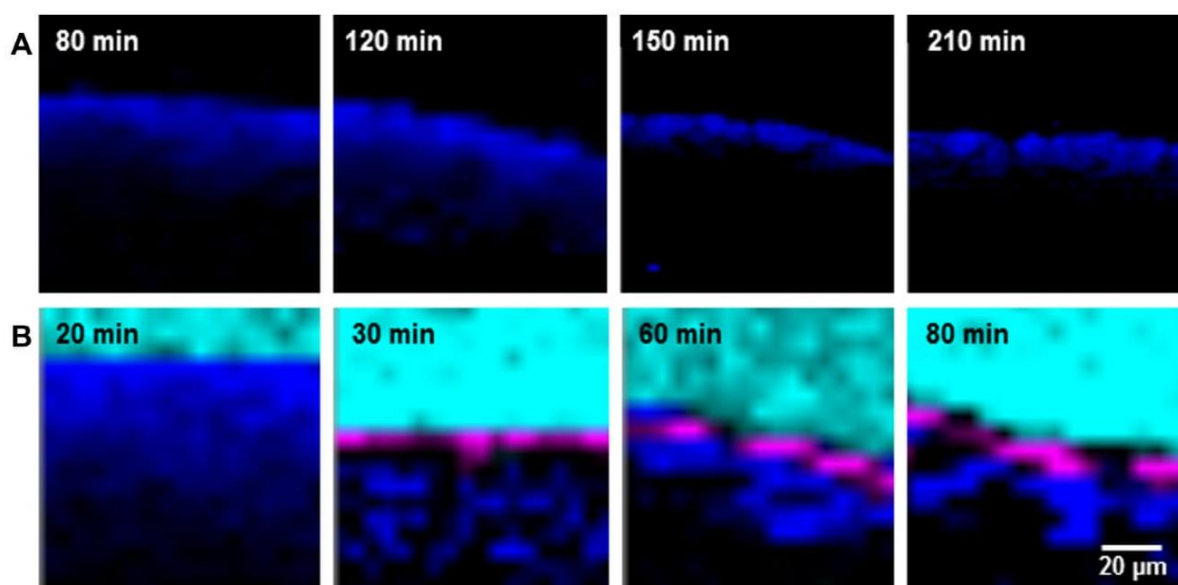
Fig. 5. Raman imaging of compound distribution changes during dissolution. (A) Tablet (Soluplus:aprepitant) and (B) tablet (PVP:aprepitant). False colors depict the solid dispersion of both compounds in dark blue, pure PVP in light blue, and pure drug crystals in pink, respectively. (For interpretation of the references to colour in this figure legend, the reader is referred to the web version of this article.)
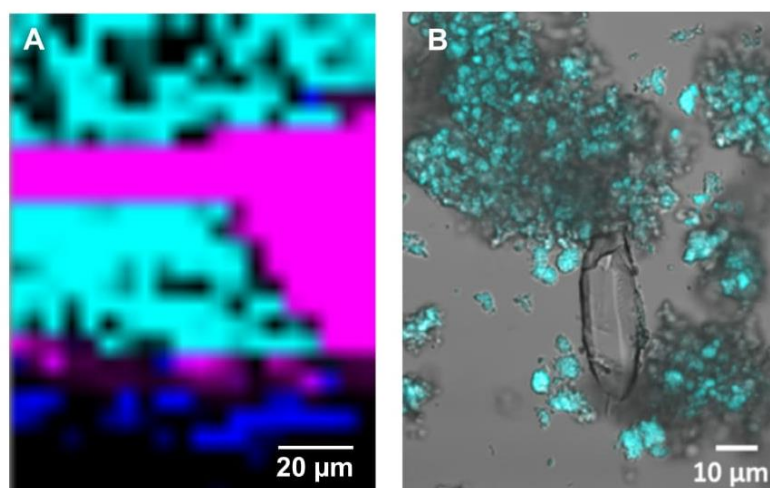
Fig. 6. Visualization of aprepitant crystals during dissolution (PVP:aprepitant tablet). (A) Virtual cross-sections using confocal Raman spectroscopy, (B) fluorescence images after staining PVP with DEAC.

from the solid dispersion. This is indicated by the separation of the solid dispersion (dark blue) and a highly hydrated PVP gel layer without any drug (light blue) whose formation is depicted in Fig 5B. After approximately 30 min, drug crystals (pink in Fig. 5B) can be detected at the interface of the PVP gel and the solid dispersion.

The reasons for this different behavior can be found in the chemical structure of the two polymers. Soluplus contains hydrogen donors as well as hydrogen acceptors for interactions with the drug and the solvent. It provides a polyethylene glycol backbone as a hydrophilic part, and vinylcaprolactam/vinyl acetate side chains as a lipophilic structure. In contrast, PVP has a hydrophilic character and exhibits fewer functional groups and a marked absence of hydrogen donors.

3.4. Analysis of crystal formation

Characterization of particle size and morphology as well as identification of crystalline and amorphous forms of the drug helps to understand the dissolution behavior of different tablet compositions. CRM analysis of aprepitant:PVP tablets confirms recrystallization of the initially amorphous drug during dissolution. It seems that after 30 min of the dissolution, the tablet surface is covered with a thin crystal layer. Then crystal growth occurs and crystalline aprepitant is released to the viscous PVP gel layer. Fig. 6A shows one such precipitated macroscopic crystal on the tablet surface in a viscous PVP layer after 110 min.

In addition, the gel layer was carefully removed after dissolution testing for 110 min and resuspended in DEAC solution
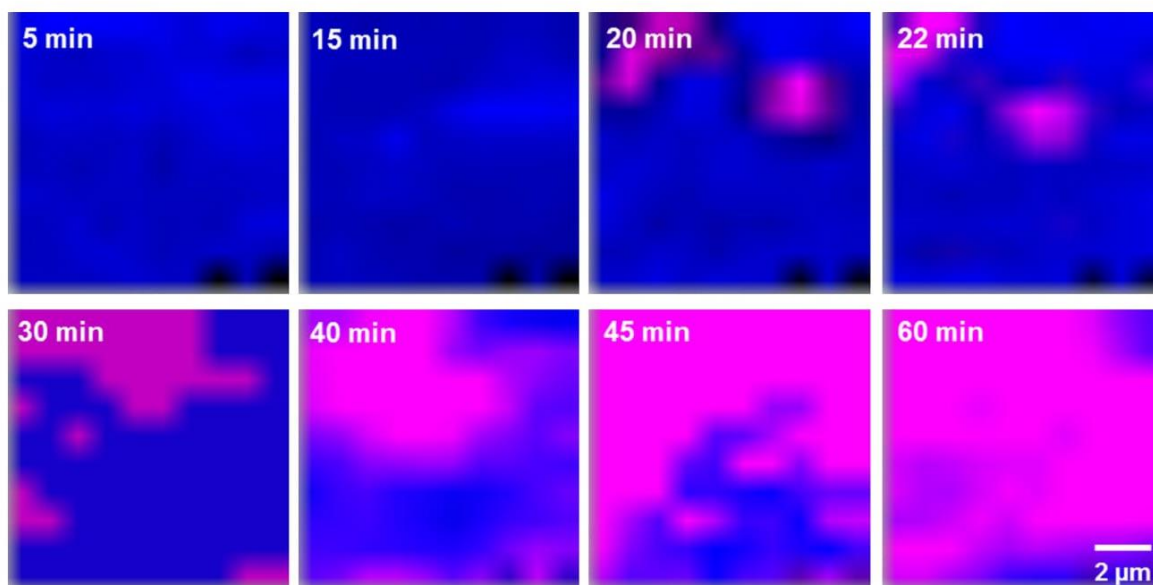
Fig. 7. Raman images of a tablet surface (PVP: aprepitant) at different time points during dissolution. False colors indicate drug crystals in pink and solid dispersion in blue. (For interpretation of the references to colour in this figure legend, the reader is referred to the web version of this article.)

enabling the formation of a fluorescent complex [27]. The macroscopic crystals of aprepitant as well as agglomerates of PVP and microscopic drug crystals were visualized with fluorescence microscopy. Drug crystals (identity confirmed by CRM) as well as PVP could be visualized (Fig. 6B).

Further, *xy* Raman images of the surface of the tablet were acquired during dissolution testing. The initial formation of aprepitant crystals was detected after 20 min of dissolution (Fig. 7, depicted in pink), followed by gradual crystal growth on the tablet surface.

3.5. Drug release mechanisms

Drug release kinetics are affected by many factors such as gel formation and erosion, drug diffusion characteristics, drug distribution inside the matrix and drug-polymer ratio. As presented above, Raman images acquired *in situ* during dissolution testing (Fig. 5) could be used for explaining the previously observed in vitro dissolution profiles (Fig. 3) and significantly contribute to our understanding of the dissolution mechanisms from solid dispersions. The Soluplus matrix is hydrated and forms a gel layer on the surface of the tablet (Fig. 8A top part). Consequently, the release of aprepitant is limited by water penetration to the tablet as well as drug diffusion through the gel layer. Local drug crystallization does not occur, presumably owing to the amphiphilic and solubilization character of Soluplus.

In contrast to Soluplus, the solid dispersion based on PVP exhibits dissolution with drug recrystallization after 20 min in static conditions on the surface of a tablet in a small volume of water, as the Raman images visualize (Fig. 5), and after 480 min in dynamic conditions in the bulk dissolution medium, as the dissolution study shows (Fig. 3). The dissolution medium is rapidly penetrating into the hydrophilic PVP matrix, resulting in PVP dissolution. The intensive stirring of the dissolution medium causes erosion of the tablet, which significantly helps to enhance the dissolution rate in the early stages until supersaturation is reached in the bulk. The difference in the release mechanisms of aprepitant from Soluplus and PVP matrices is depicted schematically in Fig. 8A. Theoretically, due to the intensive erosion the drug
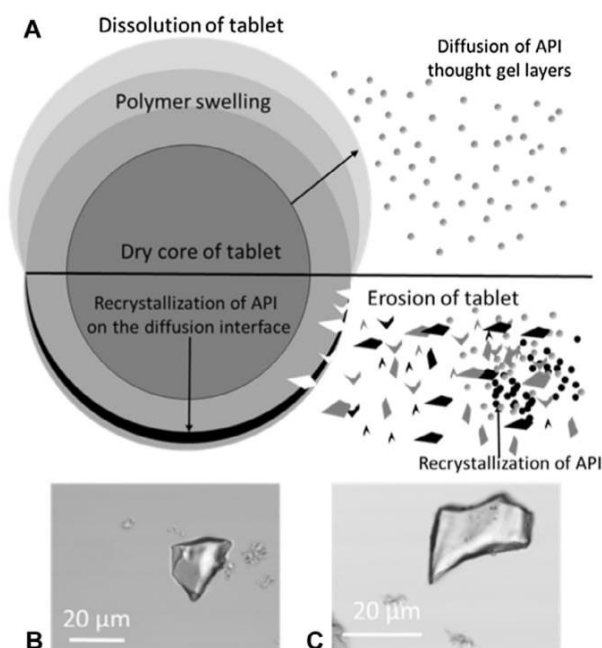
Fig. 8. (A) Scheme of processes during drug release from a tablet compressed from spray-dried particles (Soluplus:aprepitant – top part, PVP: aprepitant – bottom part), (B and C) precipitated drug crystals recovered from the dissolution medium.

does not achieve the local supersaturation on the surface of tablet after PVP depletion or the erosion of tablet enables the release of amorphous drug from the lower layers of the tablet. Moreover, optical microscopy revealed drug precipitation and crystal formation after 6 h in dissolution medium (Fig. 8B and C) during the bulk dissolution test. The eroded crystals recovered from the bulk solution had a similar shape and their size was around 30–50 μm. Both systems (static conditions in Raman images and dynamic conditions in dissolution test) confirm the inability of PVP to inhibit the precipitation of aprepitant.

4. Conclusions

The release behavior of the poorly soluble drug aprepitant from two different solid dispersions was investigated non invasively by confocal Raman microscopy and found to be largely dependent on the nature of the polymer. Even though both formulations initially incorporated the amorphous form of the drug, Soluplus has retained this form without any recrystallization during dissolution whereas drug crystals were formed in the PVP matrix after a certain time, which was conditions-dependent (20 min in static, small volume dissolution; 480 min in stirred, bulk dissolution test). PVP, as a hydrophilic polymer, dissolves rapidly and leaves behind a supersaturated solution of the drug which locally precipitates, gradually covering the tablet surface by a crystalline layer. On the other hand, the solubilization effect of Soluplus has inhibited drug precipitation. It can be hypothesized that the combination of both polymers in one matrix might improve the slow release of the drug from a solid solution with Soluplus, at the same time inhibiting the precipitation in PVP. This will be the subject of our further investigation.

Acknowledgments

References

[1] I. Tomaszewska, S. Karki, J. Shur, R. Price, N. Fotaki, Pharmaceutical characterisation and evaluation of cocrystals: importance of in vitro dissolution conditions and type of conformer, Int. J. Pharm. 453 (2013) 380–388.

[2] A.T. Serajuddin, Solid dispersion of poorly water-soluble drugs: early promises, subsequent problems, and recent breakthroughs, J. Pharm. Sci. 88 (1999) 1058–1066.

[3] R. Laitinen, K. Löbmann, C.J. Strachan, H. Grohganz, T. Rades, Emerging trends in the stabilization of amorphous drugs, Int. J. Pharm. 453 (2013) 65–79.

[4] P. Kinnari, E. Mäkilä, T. Heikkilä, J. Salonen, J. Hirvonen, H.A. Santos, Comparison of mesoporous silicon and non-ordered mesoporous silica materials as drug carriers for itraconazole, Int. J. Pharm. 414 (2011) 148–156.

[5] C.W. Pouton, Formulation of poorly water-soluble drugs for oral administration: physicochemical and physiological issues and the lipid formulation classification system, Eur. J. Pharm. Sci. 29 (2006) 278–287.

[6] S. Yamamura, H. Gotoh, Y. Sakamoto, Y. Momose, Physicochemical properties of amorphous salt of cimetidine and diflunisal system, Int. J. Pharm. 241 (2002) 213–221.

[7] W.L. Chiou, S. Riegelman, Pharmaceutical applications of solid dispersion systems, J. Pharm. Sci. 60 (1971) 1281–1302.

[8] S. Okonogi, T. Oguchi, E. Yonemochi, S. Puttipipatkhachorn, K. Yamamoto, Improved dissolution of ofloxacin via solid dispersion, Int. J. Pharm. 156 (1997) 175–180.

[9] J.Y. Jung, S.D. Yoo, S.H. Lee, K.H. Kim, D.S. Yoon, K.H. Lee, Enhanced solubility and dissolution rate of itraconazole by a solid dispersion technique, Int. J. Pharm. 187 (1999) 209–218.

[10] T. Vasconcelos, B. Sarmento, P. Costa, Soli dispersions as strategy to improve oral bioavailability of poor water soluble drugs, Drug Discovery Today 12 (2007) 1068–1075.

[11] D.Q.M. Craig, The mechanisms of drug release from solid dispersion in water-soluble polymers, Int. J. Pharm. 231 (2002) 131–144.

[12] Ch. Leuner, J. Dressman, Improving drug solubility for oral delivery using solid dispersions, Eur. J. Pharm. Biopharm. 50 (2000) 47–60.

[13] Y. Lu, N. Tang, R. Lian, J. Qi, W. Wu, Understanding the relationship between wettability and dissolution of solid dispersion, Int. J. Pharm. 465 (2014) 25–31.

[14] S.K. Das, S. Roy, Y. Kalimuthu, J. Khanam, A. Nanda, Solid dispersion: an approach to enhance the bioavailability of poorly water-soluble drugs, Int. J. Pharm. Technol. 1 (2012) 37–46.

[15] L. Lindfors, S. Forséen, J. Westergren, U. Olsson, Nucleation and crystal growth in supersaturated solutions of a model drug, J. Colloid Interface Sci. 325 (2008) 404–413.

[16] S. Janssens, G.V. Mooter, Review: physical chemistry of solid dispersions, J. Pharm. Pharmacol. 61 (2009) 1571–1586.

[17] S. Ozaki, I. Kushida, T. Yamashita, T. Hasebe, O. Shirai, K. Kano, Inhibition of crystal nucleation and growth by water-soluble polymers and its impact on the supersaturation profiles of amorphous drugs, J. Pharm. Sci. 102 (2013) 2273–2281.

[18] J. Brouwers, M.E. Brewster, P. Augustijns, Supersaturating drug delivery system: The answer to solubility-limited oral bioavailability?, J Pharm. Sci. 98 (2009) 2549–2572.

[19] B. Chamsai, P. Sriamornsak, Physical stabilizing effect of biopolymers on solid dispersions containing Indomethacin and polyethylene glycol, Adv. Mater. Res. 506 (2012) 307–310.

[20] W.I. Higuchi, N.A. Mir, S.J. Desai, Dissolution rates of polyphase mixtures, J. Pharm. Sci. 54 (1965) 1405–1410.

[21] O.I. Corrigan, Retardation of polymeric carrier dissolution by dispersed drugs: factors influencing the dissolution of solid dispersions containing polyethylene glycols, Drug Dev. Ind. Pharm. 12 (1986) 1777–1793.

[22] J.B. Nanubolu, J.C. Burley, In situ Raman mapping for identifying transient solid forms, CrystEngComm 17 (2015) 5280–5287.

[23] F. Tres, K. Treacher, J. Booth, L.P. Hughes, S.A.C. Wren, J.W. Aylott, J. Burley, Real time Raman imaging to understand dissolution performance of amorphous solid dispersions, J. Control Release 188 (2014) 53–60.

[24] K.C. Gordon, C.M. McGoverin, Raman mapping of pharmaceuticals, Int. J. Pharm. 417 (2011) 151–162.

[25] K. Punčochová, J.Y.Y. Heng, J. Beránek, F. Štěpánek, Investigation of drug-polymer interaction in solid dispersions by vapour sorption methods, Int. J. Pharm. 469 (2014) 159–167.

[26] K. Punčochová, A.V. Ewing, M. Gajdošová, N. Sarvašová, S.G. Kazarian, J. Beránek, F. Štěpánek, Identifying the mechanisms of drug release from amorphous solid dispersions using MRI and ATR-FTIR spectroscopic imaging, Int. J. Pharm. 483 (2015) 256–267.

[27] G.N. Sheth, Studies in interaction between polyvinyl pyrrolidone and stilbene fluorescent compounds. Part I: interaction with individual compounds, J. Appl. Polym. Sci. 31 (1986) 1227–1237.

5.3   Three-Dimensional Hierarchical Cultivation of Human Skin Cells on Bio-Adaptive Hybrid Fibers

47

Three-dimensional hierarchical cultivation of human skin cells on bio-adaptive hybrid fibers

V. Planz, S. Seif, J.C. Atchison, <u>B. Vukosavljevic</u>, L. Sparenberg, E. Kroner, M. Windbergs
Integr. Biol. **2016**, 8(7):775-84.

Integrative Biology

PAPER

Three-dimensional hierarchical cultivation of human skin cells on bio-adaptive hybrid fibers†

Viktoria Planz,‡[a] Salem Seif,‡[ab] Jennifer S. Atchison,[c] Branko Vukosavljevic,[d] Lisa Sparenberg,[a] Elmar Kroner[c] and Maike Windbergs*[abd]

The human skin comprises a complex multi-scale layered structure with hierarchical organization of different cells within the extracellular matrix (ECM). This supportive fiber-reinforced structure provides a dynamically changing microenvironment with specific topographical, mechanical and biochemical cell recognition sites to facilitate cell attachment and proliferation. Current advances in developing artificial matrices for cultivation of human cells concentrate on surface functionalizing of biocompatible materials with different biomolecules like growth factors to enhance cell attachment. However, an often neglected aspect for efficient modulation of cell–matrix interactions is posed by the mechanical characteristics of such artificial matrices. To address this issue, we fabricated biocompatible hybrid fibers simulating the complex biomechanical characteristics of native ECM in human skin. Subsequently, we analyzed interactions of such fibers with human skin cells focusing on the identification of key fiber characteristics for optimized cell–matrix interactions. We successfully identified the mediating effect of bio-adaptive elasto-plastic stiffness paired with hydrophilic surface properties as key factors for cell attachment and proliferation, thus elucidating the synergistic role of these parameters to induce cellular responses. Co-cultivation of fibroblasts and keratinocytes on such fiber mats representing the specific cells in dermis and epidermis resulted in a hierarchical organization of dermal and epidermal tissue layers. In addition, terminal differentiation of keratinocytes at the air interface was observed. These findings provide valuable new insights into cell behaviour in three-dimensional structures and cell–material interactions which can be used for rational development of bio-inspired functional materials for advanced biomedical applications.

1. Introduction

In-depth understanding of the composition of human tissues and interactions of their individual components currently attracts profound interest for elucidating natural processes as well as for developing bio-inspired functional materials.[1,2] In the biomedical context, one unique natural structure is represented by the extracellular matrix (ECM), which forms the basic framework for all tissues in the human body. Based on a fibrillar network,

the ECM provides three-dimensional structural support for adherence as well as for cell infiltration during migration and differentiation processes.[3] Depending on the tissue, different cell types co-exist within the ECM in a specific hierarchical order. Thus, an artificial imitation of native ECM is highly interesting with the potential to address basic research questions like cell behavior in three-dimensional structures as well as cell–material interactions with a perspective for bio-inspired products like wound dressings.[4–8]

In this context, physicochemical material characteristics like wettability and surface roughness which affect cell attachment and proliferation have extensively been investigated.[9–11] However, only recently the high importance of biomechanical properties within hierarchical native biostructures was discovered.[12–14]

In human ECM, collagen and elastin fibers as the main constituents exhibit a complex interplay upon mechanical forces.[15–17] Elastin fibers act as energy absorbers resulting in fiber fracture, while the consecutive load transfer to the larger collagen fibers leads to realignment and significant fiber elongation. Exceeding the critical yield stress causes plastic deformation of the collagen fibers by separation into fiber substructures prior

[a] Department of Biopharmaceutics and Pharmaceutical Technology, Saarland University, Campus Building A 4.1, 66123 Saarbrücken, Germany. E-mail: m.windbergs@mx.uni-saarland.de; Fax: +49 681 98806 1009; Tel: +49 681 98806 1040
[b] PharmBioTec GmbH, Science Park 1, 66123 Saarbrücken, Germany
[c] INM – Leibniz Institute for New Materials, Campus Building D 2.2, 66123 Saarbrücken, Germany
[d] Helmholtz Centre for Infection Research (HZI) and Helmholtz Institute for Pharmaceutical Research Saarland (HIPS), Department of Drug Delivery (DDEL), Campus Building E 8.1, 66123 Saarbrücken, Germany
† Electronic supplementary information (ESI) available. See DOI: 10.1039/c6ib00080k
‡ Authors contributed equally to the manuscript.

to failure.[18,19] Computational-based simulations of the hierarchical architecture of collagen could successfully demonstrate this mechano-mutable behavior at multi-scale level upon controlled mechanical stress.[20–22]

The aim of this study was to transfer this recent knowledge for fabricating biocompatible fibers by electrospinning which simulate the complex biomechanical characteristics of native ECM in human skin. Hybrid fibers based on biocompatible materials were fabricated with the intention to mimic the synchronized interplay of adequate substrate stiffness and flexibility found in ECM as a prerequisite for favored cell–material interactions. Further, advanced biomechanical testing and interaction studies with primary human skin cells were performed with the newly designed fibers to identify key characteristics for cell attachment and proliferation.

2. Materials and methods

2.1 Fabrication of electrospun scaffolds

Fiber mats were prepared by pumping a polycaprolactone (PCL) solution (12% w/v in chloroform/ethanol 1 : 1, molecular weight 80 000, Sigma-Aldrich, Steinheim, Germany) through a syringe nozzle using a flow rate of 3 ml h^{-1} and applying voltage of 8 kV. The formed fibers were deposited on a drum collector rotating at a speed of 0.5 m s^{-1} with a nozzle to collector distance of 13 cm. Blend fiber mats were fabricated based on the PCL/gelatin mixture (3 : 1 w/w, gelatin type A, 300 Bloom, Sigma-Aldrich, Steinheim, Germany) in 2,2,2-trifluoroethanol (TFE) (purity $\geq$ 99%, Sigma-Aldrich, Steinheim, Germany) at a concentration of 9% (w/v). The pumping flow rate was 3 ml h^{-1}, while the voltage was 7 kV. The syringe nozzle was located 17 cm from a drum collector rotating at 0.5 m s^{-1}. For hybrid fiber mats, two polymeric solutions were simultaneously spun allowing two types of fibers to form one fiber mat. For gelatin fibers, a flow rate of 2 ml h^{-1}, high voltage of 14 kV, and a nozzle to collector distance of 15 cm were applied. For blend fibers, a pumping flow rate of 1.5 ml h^{-1}, high voltage of 8 kV, and a nozzle to collector distance of 17 cm were used. Both fibers were simultaneously collected on the same drum collector rotating at a speed of 0.5 m s^{-1} to assure homogeneous distribution of the fibers within the fiber mat.

2.2 Confocal Raman microscopy

Confocal Raman microscopy (CRM, WITec alpha 300R+; WITec GmbH, Ulm, Germany) was utilized for chemical imaging to characterize the distribution of PCL and gelatin within the electrospun fibers. The setup was equipped with a Zeiss Epiplan Neofluar objective (50×/NA = 0.8 or 100×/NA = 0.9). Images were recorded using a diode laser with an excitation wavelength of 532 nm adjusted to a power of 20 mW before the objective. Raman spectra were acquired with a spatial resolution of 0.25 μm. Data processing and analysis were performed using WITec Project Plus software (WITec GmbH, Ulm, Germany). After removal of cosmic ray peaks and background subtraction, the collected Raman spectra were converted into false color images by supervised cluster analysis.

2.3 Physicochemical characterization of the electrospun scaffolds

Visualization of the morphological appearance of the electrospun fibers was carried out by scanning electron microscopy (SEM) using a Zeiss EVO HD 15 (Carl Zeiss AG, Oberkochen, Germany) at an acceleration voltage of 5 kV. The specimen preparation for SEM imaging included the coating of the sample surface with a thin gold layer using the sputter coater Quorum Q150R ES (Quorum Technologies Ltd, East Grinstead, UK). For the determination of the average diameter of the fibers and the pore sizes, randomly selected fibers were measured based on SEM images using ImageJ software (National Institutes of Health, USA).

Wetting properties of the electrospun fiber mats were evaluated by contact angle measurements calculating the slope of the tangent to the drop at the liquid–solid interface. Droplets with a volume of 1 μl were dispensed onto the scaffolds using a Hamilton syringe. After 5 s of incubation, the contact angle was acquired with a camera based measurement device CAM 100 (KSV Instruments Ltd, Helsinki, Finland).

Determination of the fiber mat thickness on randomly selected sample punches of the fiber mats was performed with a surface testing instrument MiniTest 3100 (ElektroPhysik Dr Steingroever GmbH & Co. KG, Cologne, Germany) based on magnetic induction. Mechanical properties of the fiber mats were determined by using a table top material testing machine from Inspekt Table Blue (Hegewald & Peschke, Nossen, Germany) by loading tension with a 5 kN load cell under constant cross head speed of 5 mm min^{-1}. Fiber mat samples were cut into rectangles of 4 × 1 cm and mounted into paper frames with an opening of 3 × 1 cm. Before applying tension, the frames were clamped with grips and cut on both lateral sides to allow for consistent loading of the samples, thus initiating the tensile test in a reproducible manner. The Young's modulus was determined by calculating the slope of the initial linear elastic region of the stress–strain curve.

2.4 Human skin preparation

Human skin was immediately received after excision from plastic surgery of female Caucasians (Department of Plastic and Hand Surgery, Caritas-Krankenhaus, Lebach, Germany) based on an ethical approval of the Saarland ethics commission (no. 88/12) and informed consent of the donors. For further proceeding, removal of the subcutaneous fat layer was performed by a scalpel and the remaining tissue was stored at −26 °C.

2.5 Extracellular matrix isolation

The isolation of native extracellular matrix based on excised human skin included two process steps. First, the deepidermization of the skin specimens was performed by heat separation. In detail, skin biopsy punches were incubated in a water bath (60 °C) for 90 s to remove the epidermis by peeling it off from the underlying dermal part using forceps. The deepidermized dermis samples were subsequently immersed in 1 M sodium hydroxide solution and stored at 37 °C for 24 h

under gentle stirring conditions to induce the decellularization of the tissue.

2.6 Degradation study

The degradation kinetics of gelatin from hybrid fiber mats were evaluated by calculating the weight loss. Previous weighed 1.2 cm punches of the hybrid fibers (about 3–4 mg each) were placed in glass vials containing 5 ml phosphate buffer solution (BSA, pH 7.4) and incubated at 37 °C for a defined period of time without shaking. At predetermined intervals, triplicate samples were removed from the test vials and analyzed. After drying at 37 °C for 24 h, the weight loss of the punches was determined in comparison to their initial weight.

2.7 Cultivation of human cells

Human primary dermal fibroblasts (NHDF-p, cat. no. C-12352) were purchased from PromoCell GmbH (Heidelberg, Germany). The immortalized human keratinocyte cell line HaCaT was kindly provided by Prof. N. Fusenig (German Cancer Research Center, Heidelberg, Germany).[23] The cells were cultivated in high-glucose Dulbecco modified Eagle's medium (Gibco® Life Technologies, Darmstadt, Germany) supplemented with 10% fetal bovine serum (Lonza, Verviers, Belgium). The cultures were maintained at 37 °C in a humidified 5% CO_2 atmosphere with medium refreshed every two days.

2.8 Cell cultivation on electrospun scaffolds

For cell cultivation, punches of 1.8 cm in diameter were prepared from PCL, blend and hybrid fiber mats. The punches were placed in 24-well plates (Greiner Bio-One GmbH, Frickenhausen, Germany) covering the whole seeding area of the well to prevent cell attachment to the well bottom. Human dermal fibroblasts were seeded at a density of 0.1×10^6 cells per well by slowly dropping the cell suspension onto the fiber mats and cultivated for 14 days. To resemble the epidermal layer, keratinocytes were seeded on top of the scaffold at a density of 0.1×10^6 cells per well and submersed cultivated for 10 days with further cultivation at air–liquid interface to induce barrier formation for 14 days. The cell-scaffold constructs were cultivated in Dulbecco modified Eagle's medium supplemented with 10% fetal bovine serum and 1% penicillin/streptomycin (PAA Laboratories, Pasching, Austria) at 37 °C in a humidified incubator gassed with 5% CO_2. The medium was carefully replaced every two days during a culture period of 38 days.

2.9 Histology

Histological assessment of the cell-scaffold constructs was performed by fixation in 4% buffered formalin, dehydration in ascending concentrations of ethanol followed by xylol incubation before paraffin embedding. Tissue sections were stained with hematoxylin/eosin (Carl Roth GmbH & Co. KG, Karlsruhe, Germany).

2.10 Cell viability

The viability of human dermal fibroblasts cultivated for five days on fiber mats was investigated by determining the amount of lactate dehydrogenase (LDH) released from cells with damaged cell membrane into the surrounding cell culture medium (Cytotoxicity Detection Kit, Roche Diagnostics, Mannheim, Germany). Absorbance values were measured using a plate reader at 550 nm wavelength.

2.11 Fluorescence staining

Evaluation of the cell behavior focusing on cell attachment, migration and proliferation of NHDF-p cells cultured on the different fiber types was performed by staining with Rhodamine labeled *Ricinus Communis Agglutinin I* (Vector Laboratories, CA, USA) to visualize the cell membrane and 4,6-diamidin-2-phenyl-indole (DAPI) obtained from Sigma-Aldrich (Steinheim, Germany) for cell nucleus labeling. Briefly, samples were washed with PBS, fixed in ice cold methanol for 10 minutes at 4 °C and rinsed again with PBS prior to the staining with the fluorescence dyes. Samples were analyzed by Zeiss LSM 700 confocal laser scanning microscopy (Jena, Germany).

2.12 Immunofluorescence staining

Assessment of barrier formation of the reconstructed skin tissue was performed by immunofluorescence staining using mouse monoclonal antibody against involucrin (Abcam ab68, Cambridge, United Kingdom). For antigen retrieval, a gentle antigen unmasking method was used by incubating the slides in 10 mM citrate buffer (pH 6.0) at 37 °C for 30 minutes. Tissue permeabilization and blocking of unspecific binding sites was achieved by using buffered solution of 0.05% saponin and 1% bovine serum albumin for 30 minutes at room temperature before primary antibody incubation at a 1:100 dilution overnight at 4 °C in a humidified chamber. Secondary polyclonal rabbit anti-mouse antibody conjugated with Alexa Fluor 488® (A-11059, Life Technologies, Carlsbad, CA, USA) was applied at a 1:500 dilution for 1 hour at room temperature. Nuclei counterstaining was performed using DAPI.

3. Results and discussion

3.1 Fabrication and characterization of bio-inspired electrospun fibers

Intensive research has been conducted to analyze the complex interactions of human cells with material surfaces for rational development of functional healthcare materials.[24] As the native ECM exhibits a fibrous structure, numerous studies focused on the analysis of biocompatible fibers and cells elucidating the influence of factors like *e.g.* surface wettability, fiber diameter and roughness.[25–29] However, even though the biomechanics within human tissues have been identified to play a vital role for cell growth, the relationship of biomechanical fiber characteristics and cellular response has not thoroughly been investigated yet.

To address this gap, we designed different types of electrospun fiber mats with individual biomechanical characteristics and analyzed and evaluated their interactions with primary human cells.

As a first approach, we electrospun one component fiber mats based on polycaprolactone (PCL), a FDA-approved, biocompatible polymer, which is insoluble in water providing a mechanically stable and flexible fiber matrix.[30] Further, to increase the wettability of the fiber surface and to coordinate the biomechanical fiber behavior using a multi-component system, we electrospun blend fibers by mixing PCL with gelatin as a natural, water soluble polymer.[31] Electrospinning of scaffolds made of PCL and gelatin has previously been reported using PCL for mechanical strength and gelatin for optimized cell attachment.[32–37] However, adequate cell attachment properties and proliferation capability as well as optimized cell penetration into the scaffold induced by sufficient scaffold porosity are critical aspects, which are still challenging to realize in case of only PCL/gelatin blend fibers. Initial attempts focused on surface modification with cost-intense bio-functionalization using collagen type I to increase the number of adhered cells.[38] Cell seeding from both scaffold sides was addressed to improve the extent of cell penetration into the scaffold.[36] Further, salt leaching procedures of the fibers were considered to increase scaffold porosity.[37] However, all these procedures are either cost-intense or accompanied by an artificial nature. Therefore, we developed as a third approach a novel compositional assembly of PCL and gelatin to fabricate scaffolds designated as "hybrid" fibers. Specifically, combining pure gelatin fibers with blend fibers (PCL/gelatin) into one scaffold based on a novel co-electrospinning setup was intended to attain a dense fiber network for the initial phase of cell attachment with a high proportion of gelatin providing more cell attachment points. Upon degradation of the pure gelatin fibers and out of the blend fibers within the hybrid assembly, the porosity of the fiber mat increases, leaving more space for scaffold infiltration. Hereby, modulation of fiber mechanics was addressed by the combination of two polymers as well as

different diameters of the two fiber types within the hybrid matrix. All three types of fiber mats were compared to native human ECM which was isolated from human skin and subsequently decellularized. Each fiber mat exhibited a homogenous fiber network with well-defined, interconnected porosity similar to the hierarchical architecture of native ECM and smooth surface (Fig. 1A). With respect to fiber diameter, especially the hybrid fibers were closely comparable to native ECM.

As the spatial distribution of different compounds in one fiber strongly affects the biomechanical properties of the material, we visualized the localization of PCL and gelatin in the blend fibers by confocal Raman microscopy as a non-invasive and chemically selective analytical technique. Based on z-stack analysis, virtual slices of the fibers in different focal planes allowed for spatially resolved, three-dimensional visualization of the fiber composition. One representative false-color image is depicted in Fig. 1B. Interestingly, gelatin (green) is mainly found at the surface of the fiber, whereas the cores of the fibers consist of pure PCL (red).

In addition, to exclude any adverse effects of the electrospun fiber mats on human cells, we performed biocompatibility testing by lactate dehydrogenase (LDH) release analysis, an established test for cell viability. Primary human fibroblasts were cultivated on the fiber mats in conventional cell culture multi-well plates for five days. Based on the respective LDH release, cells grown on fiber mats (independent of their composition) showed a higher viability compared to the ones cultivated on standard polystyrene surfaces of culture wells (Fig. 1C).

As the surface wettability is a well-known determinant influencing the biological behavior of cells on material surfaces, contact angle measurements were performed on the individual fiber mats. PCL fibers exhibited a rather hydrophobic surface indicated by a contact angle of 119°, whereas incorporation of
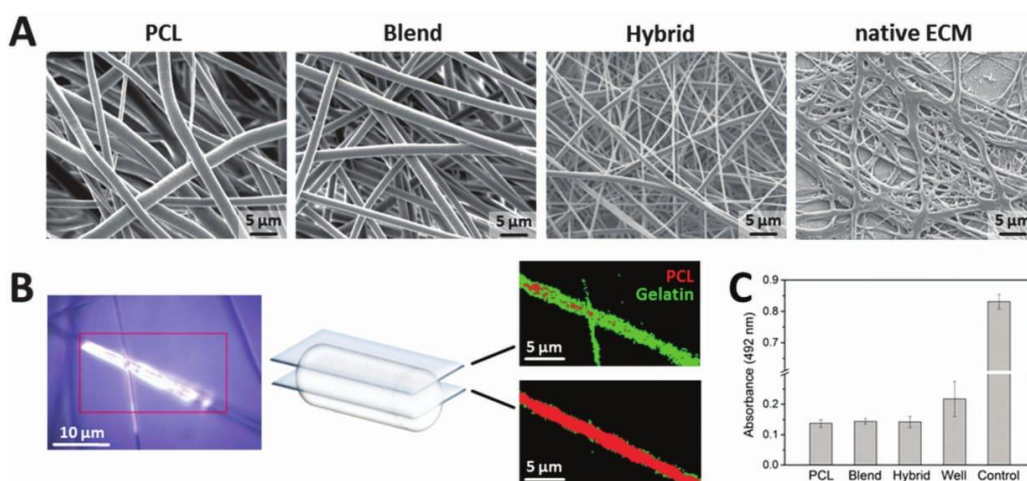
Fig. 1 Characterization of electrospun PCL, blend and hybrid fiber mats. (A) Analysis of fiber morphology based on SEM images. (B) Non-invasive, chemically selective Raman analysis of compound distribution (PCL – red, gelatin – green) in electrospun hybrid fibers. (C) Biocompatibility testing of electrospun fiber mats cultivated for five days with human dermal fibroblasts using the LDH release assay compared to cells cultivated without fiber matrix support in a well. Cells treated with 1% Triton X-100 served as control for cytotoxicity.
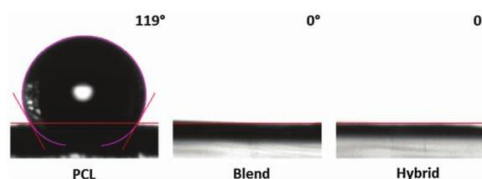
Integrative Biology

Fig. 2 Evaluation of the wetting properties of electrospun PCL, blend and hybrid fiber mats by contact angle measurements (n = 5).

gelatin as a second component in the blend and hybrid fibers significantly improved the hydrophilicity of the fiber surfaces with contact angles of 0°, thus demonstrating their excellent wettability (Fig. 2).

3.2 Evaluation of mechano-adaptive fiber characteristics

As the main focus of this study, comprehensive biomechanical testing was performed with the fabricated fibers as the biophysical micro-environment plays a crucial role as regulator of cell behavior like migration and proliferation.[39–41]

In this respect, sufficient matrix stiffness is of high importance for anchorage-dependent cells facilitating bonding to the matrix and cell proliferation. In contrast, cell adhesion and proliferation were found to be dramatically reduced upon contact with soft matrices.[40] However, intermediate matrix stiffness was identified as the best promotor for cell motility after successful adherence and proliferation.[40] These findings demonstrate the complexity of biomechanical requirements for optimized cell cultivation with the intention to mimic the native situation. For fibroblasts, Wong et al. reported the capability of these cells to probe substrate rigidity by their filopodia extensions and to adapt their cell response accordingly. They demonstrated the inhibition of focal adhesion maturation and facilitation of cell retraction on soft matrices, whereas rigid substrates promoted cell adhesion and spreading.[42] Therefore, a synchronized interplay of adequate substrate stiffness and flexibility is a prerequisite for favored cell–matrix interactions. Based on the existing knowledge that cell attachment and proliferation are promoted on stiff matrices and cell migration on an intermediate stiffness level, we aimed at introducing both aspects by providing a dynamically changing environment due to gradual gelatin degradation.[39,40] Hereby, the great amount of gelatin at the beginning of cultivation assured high fiber stiffness due to its brittle nature to promote cell attachment and proliferation. Dependent on the rate of gelatin degradation, a successive reduction in fiber stiffness is achieved, thus favoring cell infiltration into the scaffold. Another important parameter is toughness as determinant of the energy amount absorbed by a material prior to fracture. Sufficient toughness of engineered fibers to withstand contractile forces of cells attaching to the fibers is mandatory.[39] However, mimicking the optimal combination of stiffness and toughness of native ECM is a challenging task.[43,44] Based on the recent knowledge from materiomics, we followed two strategic approaches to design fiber mats intending to simulate the biomechanical properties of native ECM.[43,45–47] First, we generated multi-component fibers of different materials (PCL and gelatin) to modulate the

biomechanical behavior of pure PCL fibers. As a second strategy, we fabricated hybrid fiber mats based on the PCL/gelatin blend fibers and additional pure gelatin fibers to combine two types of fibers exhibiting different mechanical characteristics in one fiber mat. We evaluated our fabricated fibers in terms of their stiffness, flexibility and toughness properties by mechanical testing with special focus on elucidating the mechanism of fiber failure. The three different fiber mats (PCL, blend and hybrid) were characterized by uniaxial tensile testing capturing the dynamic structural changes of the fibers and their failure upon tensile loading. The PCL fiber mats started to deform by extensive necking and continuous propagation along the tension axis until the final fiber failure was attained by rapid crack propagation from the edge at a point of weakness. After tensile loading, inter-fiber fusing and negligible fiber alignment could be visualized based on electron microscopy analysis (Fig. 3A). The main reason for the bulk-like failure behavior which is also reflected in the stress–strain curve (Fig. 3B) might be related to the dense fusion of the individual fibers which does not allow for reorientation or unraveling of individual fibers.[43] In comparison, the blend fiber mats exhibited non-uniform elongation properties along the tensile axis. With ongoing deformation, defects started to appear at different positions of the sample until a critical defect density led to failure (Fig. 3A).[46] The fracture process of blend fibers could generally be identified as tearing failure starting from the sample edge with rapid propagation along the sample surface. After tensile loading, electron microscopy revealed less fiber fusing and notable fiber alignment in the direction of the tensile stress (Fig. 3A). This behavior might be related to the core–shell structure of the fibers (shell-gelatin, core-PCL). It is known that gelatin fibers are considerably stiffer than PCL fibers as reflected by the higher Young's modulus of gelatin.[32] Thus, compared to pure PCL fibers, blending PCL with gelatin to form two-component fibers considerably altered their biomechanical characteristics towards a stiffer and tougher matrix as indicated by the steep shift of the linear elastic phase within the stress–strain curve of blend fibers in y-direction (Fig. 3B). In contrast to the rapid crack propagation of PCL and blend fibers, hybrid fibers failed by gradual fiber breakage. Under tensile loading, hybrid fibers exhibited significant reorganization and alignment along the tensile axis during the test. At the initial phase of the test, the uniformly stretched hybrid fibers exhibited some localized weak points where first fiber breakage occurred. Each failure event seemed to allow unraveling of the fibers and facilitated increased elongation (Fig. 3A). Continuous elongation of the fibers resulted in progressive thinning of the parallely realigned fibers until final sample breakage was induced by sequential failure of individual fibers. The presence of multiple fracture events, also evident in stepped stress–strain curve, further reinforced this sequential fiber fracture mode (Fig. 3B). In addition, the stress–strain curve revealed a brittle-to-ductile transition during fracture of hybrid fibers. Consequently, two coordinated failure mechanisms could be derived, one by the blend fibers and another one by the pure gelatin fibers. In detail, upon tensile loading, the thin gelatin fibers within the hybrid assembly underwent brittle failure at low strains after
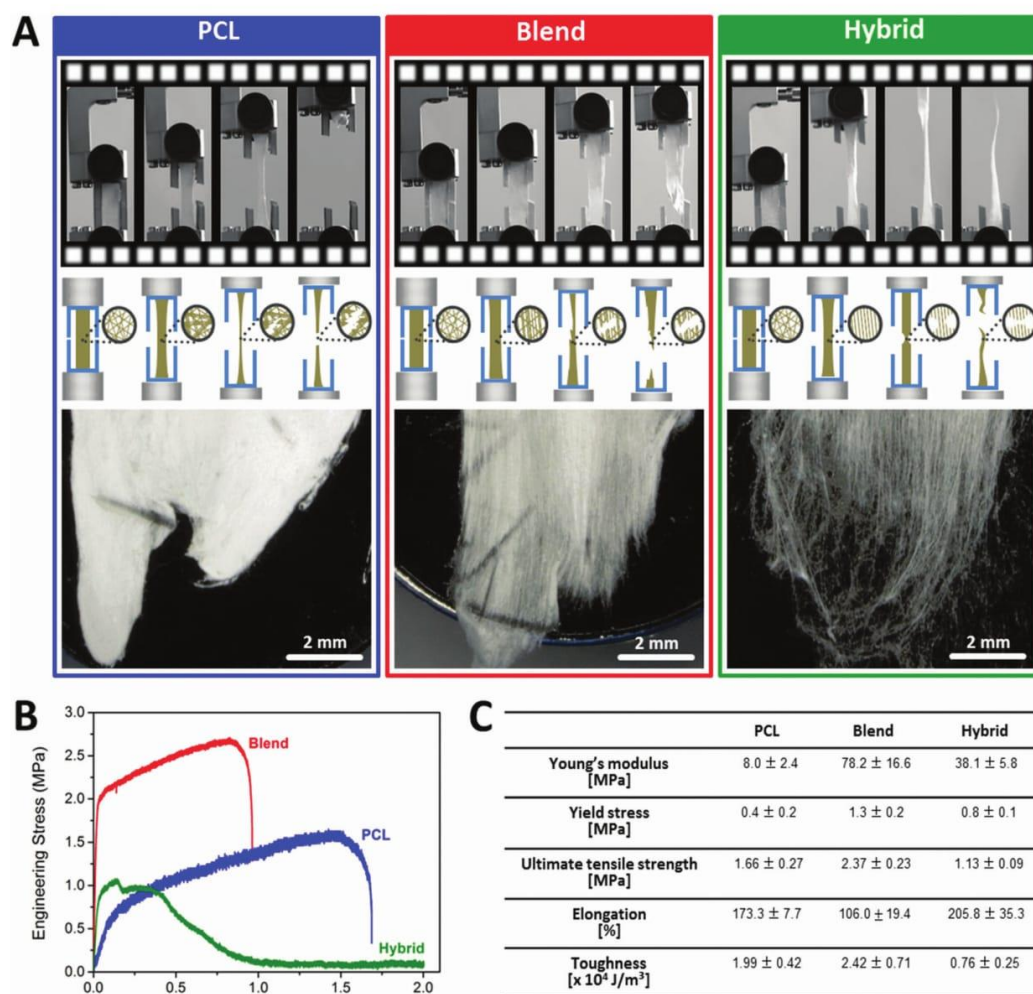
Fig. 3 Mechanical properties of electrospun PCL, blend and hybrid fiber mats. (A) Visualization of the different failure modes based on acquired time-lapsed serial images upon tensile loading and representative optical micrographs of the fracture fiber surfaces after mechanical testing. (B) Typical engineering stress–strain curves for each type of fiber mats. (C) Mechanical parameters calculated from the engineering stress–strain curves.

energy absorbance. Consequently, the load was transferred to the larger blend fibers, thereby providing more space for reorganization and alignment until final fiber fracture was attained in a ductile manner. Accordingly, the failure behavior of the hybrid fibers excellently correlated to the anisotropic mechanical behavior found in native ECM as described above.[18,19,22] High-speed video sequences of typical tensile loading tests for the different fibers are provided as ESI,† V1–V3. A detailed characterization of the fiber mechanics focusing on Young's modulus, toughness and elongation obtained from stress–strain curve calculations is summarized in Fig. 3C. In terms of elongation, all fibers could be stretched at least 100% of their original length before failure, with the highest elongation capability for hybrid fibers. As previously reported for collagen-rich tissue, extensive fiber deformation capability is of major importance for optimal biological function by minimizing brittle-like failure events.[20]

These findings highlight that effective modulation of bio-mechanical fiber properties can be governed by both, mechanical properties of the materials (brittle or ductile) and structural organization of different materials within the fiber matrix.

3.3 Degradation kinetics of gelatin from bio-adaptive hybrid fibers

In addition to the biomechanical properties, the surface properties of the fibers and the porosity of the mats play important roles for cell behavior as already mentioned above.[9,10,28,29] The hybrid fibers consist of gelatin as water-soluble polymer with good wettability and PCL which is not water-soluble and less wettable. The intention of mixing pure gelatin fibers with blend

fibers (PCL/gelatin) was to provide a dense fiber network for the initial phase of cell attachment with gelatin providing binding sites at the pure fibers as well as on the surface of the blend fibers. Upon slow degradation of the gelatin, the porosity of the fiber mat increases leaving more space for cell infiltration and migration into the remaining part of the blend fibers. To determine the degradation kinetics of gelatin within the hybrid scaffolds, we performed degradation studies in PBS buffer solution at 37 °C for a duration of four months. A combination

of electron microscopy and confocal Raman microscopy was utilized to visualize changes during gelatin degradation. Before degradation, two fiber types with different diameters were identified within the hybrid fiber mats, the thinner ones being gelatin and the thicker ones being blend fibers (Fig. 4A). During the study, pure gelatin fibers were completely degraded, indicated by the absence of thin fibers on SEM micrographs, which could be confirmed by CRM examination (Fig. 4B). At a higher magnification, the degradation of gelatin can also be traced on the surface of the blend fibers. Before contact with liquid media, the fibers exhibit a smooth surface mainly based on gelatin (Fig. 4C). Upon degradation, the dissolved gelatin leaves small voids in the surface
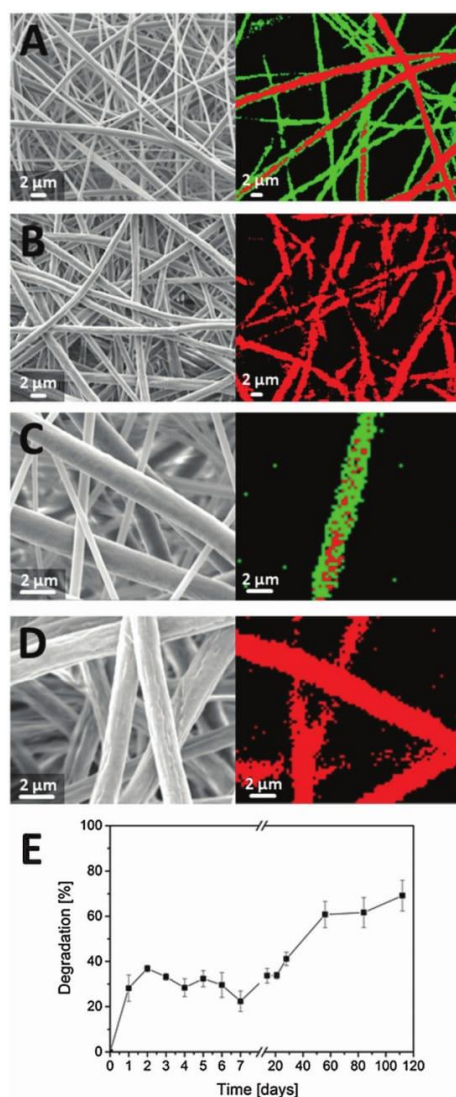
Fig. 4 Evaluation of degradation kinetics of gelatin from hybrid fiber mats using SEM and Raman analysis (PCL – red, gelatin – green); (A) before degradation; (B) after degradation; (C) before degradation at higher magnification exhibiting a smooth surface; (D) after degradation at higher magnification exhibiting a structured surface; (E) degradation kinetics of gelatin over four months.
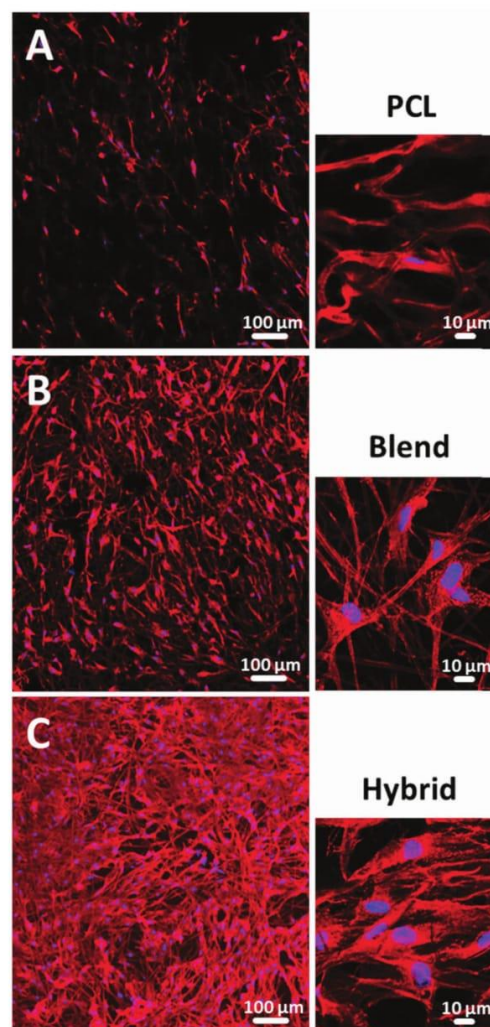
Fig. 5 Evaluation of cell−matrix interactions by analysis of cell behavior as response to fiber surface. Fluorescence staining of cell membrane (red) and cell nuclei (blue) to visualize human dermal fibroblasts cultivated for 14 days onto (A) PCL, (B) blend and (C) hybrid fiber mats revealing considerable differences in cell density and three-dimensional cell-shaping among these three electrospun fiber mats.

of the fibers visualized by electron microscopy in Fig. 4D. Such increase of "surface roughness" due to a soluble compound in blend fibers has already been reported by Xue *et al.*[33] Further, the degradation kinetics ideally match the requirements for the different phases of cell cultivation, providing a dense gelatin-rich structure in the first 24–48 hours for cell attachment. Subsequently, higher porosity due to degradation of the pure gelatin fibers facilitates cell infiltration and migration (Fig. 4E).

3.4 Assessment of cell–matrix interactions

As a next step, we cultivated primary human skin fibroblasts on all three fiber mats (pure PCL, blend and hybrid fibers) to analyze cell–fiber interactions for evaluating the suitability of each fiber mat type and elucidating critical composite attributes for imitation of native ECM. Among the three fabricated types of fibers, we observed considerable differences in terms of cell morphology and density. The level of cell coverage on the PCL fiber mats was rather low (Fig. 5A). This effect is due to the hydrophobic surface characteristics (contact angle 119°), which hamper optimal cell attachment as well as to low stiffness properties (8.0 MPa ± 2.5 MPa, $n = 6$) and moderate toughness (1.99×10^4 J m^{-3} ± 0.42, $n = 6$). In contrast, fiber mats consisting of a PCL/gelatin blend showed a higher cell density

and three-dimensional cell shaping induced by improved cell attachment properties due to the increased fiber hydrophilicity (contact angle 0°) as well as a considerable increase in stiffness (78.2 MPa ± 16.6 MPa, $n = 6$) and toughness (2.42×10^4 J m^{-3} ± 0.71, $n = 6$) (Fig. 5B). The highest level of cell growth and three-dimensional cell organization was visualized for the PCL/gelatin hybrid fiber mats. The cells were able to attach to multiple fibers due to their improved surface hydrophilicity and smaller pore sizes in the initial phase (Fig. 5C). To verify our findings regarding the supportive effect of hybrid fibers on cell proliferation based on qualitative analysis using fluorescence imaging in comparison to pure PCL and blend fibers, we further performed quantitative cell counting experiments. The data are presented as ESI,† S1.

The biodegradation of gelatin over time induced the fiber mat pore structure to dynamically change during cultivation allowing the cells to infiltrate the hybrid fiber mat as shown for human dermal fibroblasts (Fig. 6A) and human keratinocytes (Fig. 6B) based on z-stack analysis. These findings highlight the potential of the hybrid fiber mats as a suitable biomimetic structure comparable to native ECM.

3.5 Evaluation of hierarchical three-dimensional cultivation of human cells

Further, we evaluated the potential of the hybrid fiber mats for the hierarchical three-dimensional co-cultivation of different human skin cells. As previously reported, conventional two-dimensional culture surfaces significantly influence cell morphology and function *e.g.* flattening.[48–50] Three-dimensional cell cultures are generally grown with the use of hydrogel substrates.[51–54] However, obviously a gel is not mimicking the fiber structure and mechanical properties of native ECM.[55,56] In this study, we cultivated fibroblasts (as cells forming the dermis in human skin) on the fiber mats in a multi-well plate assembly equipped with permeable membrane inserts. After 14 days of cultivation, keratinocytes were seeded on top of this assembly to form the
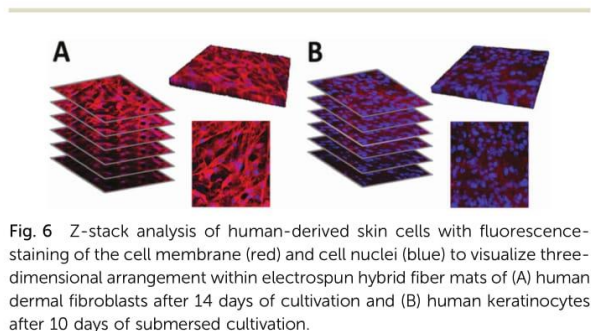

Fig. 6 Z-stack analysis of human-derived skin cells with fluorescence-staining of the cell membrane (red) and cell nuclei (blue) to visualize three-dimensional arrangement within electrospun hybrid fiber mats of (A) human dermal fibroblasts after 14 days of cultivation and (B) human keratinocytes after 10 days of submersed cultivation.
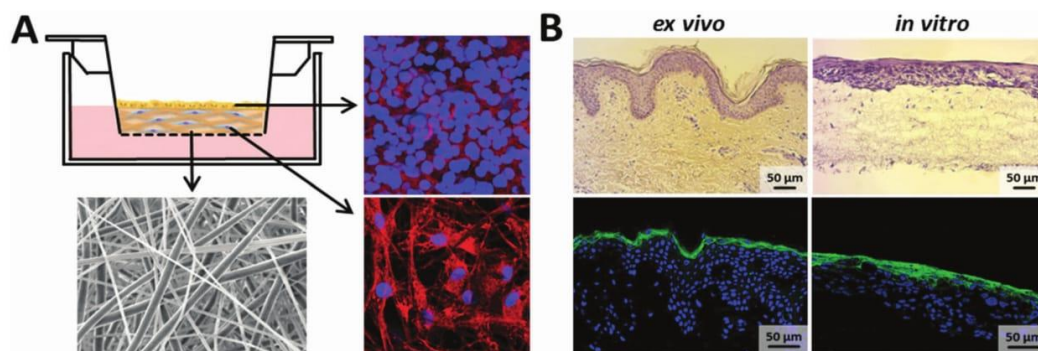

Fig. 7 Evaluation of the applicability of electrospun hybrid fiber mats for hierarchical co-cultivation of human-derived skin cells. (A) Experimental setup for *in vitro* reconstruction of human skin tissue using a Transwell®-system by first seeding human primary dermal fibroblasts on electrospun hybrid fiber mats for 14 days, followed by co-cultivation with human keratinocytes on top of the fiber mats surface for 10 days under submersed culture conditions and further cultivation at air–liquid interface for 14 days. (B) Example of *in vitro* reconstructed skin tissue visualized by hematoxylin/eosin staining and evaluation of barrier formation by immunofluorescence-staining of terminal differentiated keratinocytes (green) using involucrin (right column) compared to *ex vivo* human skin tissue (left column).

upper epidermal part of human skin. Subsequently, the inserts of the well plate were lifted to the air–liquid interface to induce a stratification of the upper keratinocyte layers,[57,58] thus mimicking the *in vivo* situation in the human body as illustrated in the schematic diagram of Fig. 7A. Representative fluorescence-based images of fibroblasts (bottom right corner) and keratinocytes (top right corner) cultivated on hybrid fibers are shown in Fig. 7A. Visualization of cell compartments was performed by fluorescence-based staining of the cell membrane (red) and cell nuclei (blue). The fibroblasts revealed a three-dimensional cellular organization in response to the hybrid fiber mat surface after two weeks of cultivation. The high cell density of keratinocytes detected on the hybrid fiber mat surface after ten days of submersed cultivation further reinforced the applicability of these hybrid fibers offering optimal conditions for cell growth. As the final step of our study, we compared the fiber mats with excised human skin by histological analysis based on cross sections stained with hematoxylin/eosin (Fig. 7B). Hematoxylin (blue) binds to cell nuclei, whereas eosin staining (pink) visualizes collagenous structures as the main constituents of the dermis part. As the direct comparison of fiber mat and excised human skin shows, a multilayered sheet of keratinocytes was evident and highly comparable to native epidermal structures. The presence and in-growth of the fibroblasts into the scaffold could clearly be visualized by the distribution of the fibroblast nuclei throughout the entire scaffold (Fig. 7B). Further, we verified the barrier formation by involucrin (green) as a specific immunofluorescence-based marker for terminal differentiation of the keratinocytes.[59,60] In addition, we used DAPI staining (blue) to visualize the cell nuclei, which are present in high density in the viable epidermis to confirm the corresponding localization of involucrin occurring towards the air exposed region above the viable part of the epidermis. A uniform consistent stratified layer was apparent as shown at the bottom right corner of Fig. 7B, indicating the presence of an intact barrier in our reconstructed skin along the entire length of the cross section with morphological similarity to the situation in the human body as visualized at the bottom left corner of Fig. 7B.

4. Conclusions

In summary, we fabricated biocompatible hybrid fibers simulating the complex biomechanical characteristics of native ECM in human skin. These three-dimensional fibrillar networks provide a unique bio-adaptive environment for cell attachment, migration, and proliferation within the fiber matrix without the necessity to attach additional growth factors. In interactions studies with skin cells, we demonstrated the mediating effect of tailored biomechanics, in combination with wettability and biodegradation of the fibers on cellular behavior, thus verifying the synergistic role of these key parameters to facilitate cell attachment and proliferation. Co-cultivation of fibroblasts and keratinocytes on the fiber mats resulted in a hierarchical organization of dermal and epidermal tissue layers with terminal cell differentiation. These findings provide valuable new insights into cell behavior

in three-dimensional structures and cell–material interactions which can be used for rational development of bio-inspired functional materials for advanced biomedical applications. Future studies will aim on a quantitative understanding of how local fiber properties determine the behavior on a three-dimensional tissue level.

Acknowledgements

References

1 Y. Bar-Cohen, *Bioinspiration Biomimetics*, 2006, **1**, P1.
2 N. F. Lepora, P. Verschure and T. J. Prescott, *Bioinspiration Biomimetics*, 2013, **8**, 013001.
3 C. Frantz, K. M. Stewart and V. M. Weaver, *J. Cell Sci.*, 2010, **123**, 4195.
4 O. Guillame-Gentil, O. Semenov, A. S. Roca, T. Groth, R. Zahn, J. Vörös and M. Zenobi-Wong, *Adv. Mater.*, 2010, **22**, 5443.
5 R. Xu, M. B. Taskin, M. Rubert, D. Seliktar, F. Besenbacher and M. Chen, *Sci. Rep.*, 2015, **5**, 8480.
6 T. C. Reis, S. Castleberry, A. M. Rego, A. Aquiar-Ricardo and P. T. Hammond, *Biomater. Sci.*, 2016, **4**, 319.
7 M. Norouzi, S. M. Boroujeni, N. Omidvarkordshouli and M. Soleimani, *Adv. Healthcare Mater.*, 2015, **4**, 1114.
8 S. Drotleff, U. Lungwitz, M. Breunig, A. Dennis, T. Blunk, J. Tessmar and A. Göpferich, *Eur. J. Pharm. Biopharm.*, 2004, **58**, 385.
9 N. M. Alves, I. Pashkuleva, R. L. Reis and J. F. Mano, *Small*, 2010, **6**, 2208.
10 J. Pelipenko, P. Kocbek, B. Govedarica, R. Rošic, S. Baumgartner and J. Kristl, *Eur. J. Pharm. Biopharm.*, 2013, **84**, 401.
11 H. Rashidi, J. Yang and K. M. Shakesheff, *Biomater. Sci.*, 2014, **2**, 1318.
12 S. W. Cranford, J. de Boer, C. van Blitterswijk and M. J. Buehler, *Adv. Mater.*, 2013, **25**, 802.
13 S. Cranford and M. J. Buehler, *Nanotechnol., Sci. Appl.*, 2010, **3**, 127.
14 M. J. Buehler, *MRS Bull.*, 2013, **38**, 169.
15 L. D. Muiznieks and F. W. Keeley, *Biochim. Biophys. Acta*, 2013, **1832**, 866.
16 N. Naik, J. Caves, E. L. Chaikof and M. G. Allen, *Adv. Healthcare Mater.*, 2014, **3**, 367.
17 Z. Zhang and B. B. Michniak-Kohn, *Pharmaceutics*, 2012, **4**, 26.
18 A. Ní Annaidh, K. Bruyère, M. Destrade, M. D. Gilchrist and M. Otténio, *J. Mech. Behav. Biomed. Mater.*, 2012, **5**, 139.
19 R. H. Pritchard, Y. Y. Huang and E. M. Terentjev, *Soft Matter*, 2014, **10**, 1864.
20 M. J. Buehler, *Proc. Natl. Acad. Sci. U. S. A.*, 2006, **103**, 12285.
21 A. Gautieri, S. Vesentini, A. Redaelli and M. J. Buehler, *Nano Lett.*, 2011, **11**, 757.

22 Y. Tang, R. Ballarini, M. J. Buehler and S. J. Eppell, *J. R. Soc., Interface*, 2010, **7**, 839.
23 P. Boukamp, R. T. Petrussevska, D. Breitkreutz, J. Hornung, A. Markham and N. E. Fusenig, *J. Cell Biol.*, 1988, **106**, 761.
24 N. Oliva, S. Unterman, Y. Zhang, J. Conde, H. S. Song and N. Artzi, *Adv. Healthcare Mater.*, 2015, **4**, 1584.
25 T. Sun, D. Norton, R. J. McKean, J. W. Haycock, A. J. Ryan and S. MacNeil, *Biotechnol. Bioeng.*, 2007, **97**, 1318.
26 J. L. Lowery, N. Datta and G. C. Rutledge, *Biomaterials*, 2010, **31**, 491.
27 J. Pelipenko, P. Kocbek and J. Kristl, *Eur. J. Pharm. Sci.*, 2014, **66C**, 29.
28 M. Nikkhah, F. Edalat, S. Manoucherie and A. Khademhosseini, *Biomaterials*, 2012, **33**, 5230.
29 W. Zheng, W. Zhang and X. Jiang, *Adv. Healthcare Mater.*, 2013, **2**, 95.
30 M. A. Woodruff and D. W. Hutmacher, *Prog. Polym. Sci.*, 2010, **35**, 1217.
31 Z.-M. Huang, Y. Z. Zhang, S. Ramakrishna and C. T. Lim, *Polymer*, 2004, **45**, 5361.
32 Y. Zhang, H. Ouyang, C. T. Lim, S. Ramakrishna and Z.-M. Huang, *J. Biomed. Mater. Res., Part B*, 2005, **72**, 156.
33 J. Xue, M. He, H. Liu, Y. Niu, A. Crawford, P. D. Coates, D. Chen, R. Shi and L. Zhang, *Biomaterials*, 2014, **35**, 9395.
34 S. Gautam, A. K. Dinda and N. C. Mishra, *Mater. Sci. Eng., C*, 2013, **33**, 1228.
35 L. Ghasemi-Mobarakeh, M. P. Prabhakaran, M. Morshed, M. H. Nasr-Esfahani and S. Ramakrishna, *Biomaterials*, 2008, **29**, 4532.
36 E. J. Chong, T. T. Phan, I. J. Lim, Y. Z. Zhang, B. H. Bay, S. Ramakrishna and C. T. Lim, *Acta Biomater.*, 2007, **3**, 321.
37 P. T. Hwang, K. Murdock, G. C. Alexander, A. D. Salaam, J. I. Ng, D. J. Lim, D. Dean and H. W. Jun, *J. Biomed. Mater. Res., Part A*, 2016, **104**, 1017.
38 S. Gautam, C. F. Chou, A. K. Dinda, P. D. Potdar and N. C. Mishra, *Mater. Sci. Eng., C*, 2014, **34**, 402.
39 D. E. Discher, P. Janmey and Y.-L. Wang, *Science*, 2005, **310**, 1139.
40 R. G. Wells, *Hepatology*, 2008, **47**, 1394.
41 B. Geiger, J. P. Spatz and A. D. Bershadsky, *Nat. Rev. Mol. Cell Biol.*, 2009, **10**, 21.
42 S. Wong, W.-H. Guo and Y.-L. Wang, *Proc. Natl. Acad. Sci. U. S. A.*, 2014, **111**, 17176.
43 C. T. Koh and M. L. Oyen, *J. Mech. Behav. Biomed. Mater.*, 2012, **12**, 74.
44 R. O. Ritchie, *Nat. Mater.*, 2011, **10**, 817.
45 M. E. Launey and R. O. Ritchie, *Adv. Mater.*, 2009, **21**, 2103.
46 C. T. Koh, D. G. Strange, K. Tonsomboon and M. L. Oyen, *Acta Biomater.*, 2013, **9**, 7326.
47 U. G. Wegst, H. Bai, E. Saiz, A. P. Tomsia and R. O. Ritchie, *Nat. Mater.*, 2015, **14**, 23.
48 F. Pampaloni, E. G. Reynaud and E. H. K. Stelzer, *Nat. Rev. Mol. Cell Biol.*, 2007, **8**, 839.
49 H. Page, P. Flood and E. G. Reynaud, *Cell Tissue Res.*, 2013, **352**, 123.
50 E. Knight and S. Przyborski, *J. Anat.*, 2015, **227**, 746.
51 T. Elsdale and J. Bard, *Cell Biol.*, 1972, **54**, 626.
52 E. Bell, H. P. Ehrlich, D. J. Buttle and T. Nakatsuji, *Science*, 1981, **211**, 1052.
53 R. A. Brown, *Exp. Cell Res.*, 2013, **319**, 2460.
54 R. Dong, Y. Pang, Y. Su and X. Zhu, *Biomater. Sci.*, 2015, **3**, 937.
55 H.-J. Stark, M. J. Willhauck, N. Mirancea, K. Boehnke, I. Nord, D. Breitkreutz, A. Pavesio, P. Boukamp and N. E. Fusenig, *Eur. J. Cell Biol.*, 2004, **83**, 631.
56 M. L. Oyen, *Int. Mater. Rev.*, 2014, **59**, 44.
57 M. Fartasch and M. Ponec, *J. Invest. Dermatol.*, 1994, **102**, 366.
58 M. O. Danso, T. Berkers, A. Mieremet, F. Hausil and J. A. Bouwstra, *Exp. Dermatol.*, 2015, **24**, 48.
59 F. M. Watt, *J. Invest. Dermatol.*, 1983, **81**, 100s.
60 E. Candi, R. Schmidt and G. Melino, *Nat. Rev. Mol. Cell Biol.*, 2005, **6**, 328.

5.4   Tracing Molecular and Structural Changes upon Mucolysis with N-Acetyl Cysteine in Human Airway Mucus

Tracing molecular and structural changes upon mucolysis with N-acetyl cysteine in human airway mucus

B. Vukosavljevic*, X. Murgia*, K. Schwarzkopf, U.F. Schaefer, C.M. Lehr, M. Windbergs
Int. J. Pharm. **2017**, DOI: 10.1016/j.ijpharm.2017.07.022.

* These authors contributed equally to this work.

ARTICLE IN PRESS

Contents lists available at ScienceDirect

International Journal of Pharmaceutics

journal homepage: www.elsevier.com/locate/ijpharm

Tracing molecular and structural changes upon mucolysis with N-acetyl cysteine in human airway mucus

Branko Vukosavljevic[a,1], Xabier Murgia[a,1], Konrad Schwarzkopf[b], Ulrich F. Schaefer[c], Claus-Michael Lehr[a,c,*], Maike Windbergs[a,d,*]

[a] Helmholtz Institute for Pharmaceutical Research Saarland (HIPS), Helmholtz Centre for Infection Research (HZI), Saarland University, 66123 Saarbruecken, Germany
[b] Department of Anesthesia and Intensive Care, Clinics Saarbruecken, 66119 Saarbruecken, Germany
[c] Biopharmaceutics and Pharmaceutical Technology, Department of Pharmacy, Saarland University, 66123 Saarbruecken, Germany
[d] Institute of Pharmaceutical Technology and Buchmann Institute for Molecular Life Sciences, Goethe University Frankfurt, 60438 Frankfurt am Main, Germany

A B S T R A C T

The conducting airways of the human lungs are lined by mucus, which lubricates the lung epithelium and provides a first-line protection against airborne threats. As a novel approach for visualization of the human mucus microstructure, we applied confocal Raman microscopy as a label-free and chemically selective technique. We were successfully able to chemically resolve the pulmonary surfactant from the mucus matrix and show its spatial distribution, as well as to visualize the structural changes within the freeze–dried mucus mesh upon chemical mucolysis. Subsequently, we performed rheological measurements before and after mucolysis and correlated morphology and chemical structure of the mucus with its rheological characteristics. These results do not only enrich the knowledge about the mucus microstructure, but can also, significantly contribute to rational development of future lung therapeutics.

© 2017 Elsevier B.V. All rights reserved.

1. Introduction

Among cellular and non-cellular biological barriers of the human lungs, mucus plays a prominent role in protecting the conducting airways and the underlying epithelial tissue against external airborne threats (Sigurdsson et al., 2013). As mucus lines the surface of the airways, its properties can affect pathophysiological processes as well as absorption of drugs administered via the pulmonary route, e.g. by particle trapping (Suk et al., 2014; Kim et al., 2015) and subsequent clearance by the mucociliary escalator (Knowles and Boucher, 2002). Therefore, insight into the biochemical mucus structure and understanding its composition and interactions is of high interest for elucidating the course of

lung diseases as well as for rational development of effective therapeutics for lung application (Kumar et al., 2016; Sakuma et al., 2012; Yu et al., 2016; Nordg&rd et al., 2014).

Airway mucus forms a complex hydrogel (water content 95% w/w) incorporating glycoproteins (mucins, 2–5% w/w), non-mucin proteins, lipids, salts, DNA, enzymes, cellular debris, and pulmonary surfactant (Rubin, 2002; Schuster et al., 2013; Ruge et al., 2013).
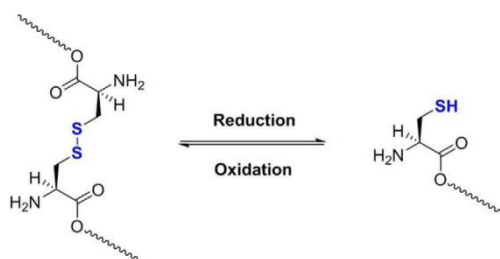
The structural mesh for this hydrogel is constituted by mucins which consist of a polypeptide backbone with side glycans (O-glycosylated units) stabilized by intermolecular disulfide bonding (Sigurdsson et al., 2013). These bonds are formed between the thiol groups of cysteine residues in a reversible process called oxidative folding. This systematic overlapping of mucins leads to protein stabilization (Sevier and Kaiser, 2002) and to the formation of a tight mesh with a highly heterogeneous pore size (Murgia et al., 2016). However, chemical reduction leads to the reversion of this process by formation of free thiol groups (Fig. 1). This reaction is intentionally targeted when applying N-acetyl cysteine, which is currently the only approved thiol-based mucolytic agent for therapeutic purposes.

Fig. 1. Chemical reduction of a disulfide bond (-S-S-) in a cysteine dimer and oxidative folding of a thiol group (-SH) as reversible reaction.

Systematic analysis of the mucus microstructure in its native state is challenging, as it requires conserving the hydration state of the hydrogel to avoid collapsing of the gel mesh and thus dislocation of the compounds. Established techniques generally either require manipulation of the sample (e.g. staining, fixation) or can only visualize the morphological structure without the chemical information of the individual compounds.

In this study, we investigated human airway mucus with confocal Raman microscopy as a label-free and chemically selective technique to visualize its structure and composition. Mucus samples were analyzed in its native state as well as after freeze drying. We investigated structural changes within the mucus mesh upon chemical mucolysis with N-acetylcysteine as an established therapeutic mucolytic agent. Subsequently, we performed rheological measurements before and after mucolysis and correlated morphology and chemical structure of the mucus with its rheological characteristics.

2. Materials and methods

2.1. Materials

For acquisition of the reference spectrum, dipalmitoyl phosphatidylcholine (DPPC) was purchased from Avanti Polar lipids, Inc. (Alabaster, AL) and N-acetyl cysteine (NAC) from Sigma −Aldrich (Munich, Germany).

2.2. Mucus sample collection

Human airway mucus samples were collected by the endotracheal tube method (Nordgård et al., 2014) after informed consent from the patients and in compliance with a protocol approved by the Ethics Commission of the "Ärztkammer des Saarlandes" (file number 19/15). In brief, the tracheal tubes of patients undergoing elective surgery non-related to pulmonary conditions were collected after surgery. The distal portion of the tube (5–10 cm) was cut and placed in a 50 ml centrifuge tube. The mucus of each tracheal tube was pooled by centrifuging the samples at 1200 rpms for 30 s. Mucus samples were stored at −20 °C until use. This storage method does not have a significant influence neither on the viscoelasticity of mucus, nor in the diffusion coefficient of drugs (Sanders et al., 2000; Larhed et al., 1997). In total 10 mucus samples from independent patients were used in this study. Mean age of the patients was 58.3 ± 19 years, male: female ratio was 6:4, and mean surgery time 75 ± 34 min.

2.3. Freeze drying

Native mucus aliquots were gradually thawed and volumes of approximately 30–40 μl were spread over a Teflon surface and stored at −80 °C for 4 h. Thereafter, frozen mucus samples were immediately transferred to the freeze-drier (Alpha 2–4 LSC, Christ,

Germany) and freeze-dried overnight at −80 °C. Freeze–dried mucus samples were stored in a dark and dry environment until analysis. For controlled mucolysis, mucus aliquots were incubated for two hours with NAC (100 mg/ml, 10% w/w) before starting the freeze-drying process(Yuan et al., 2015).

2.4. Scanning electron microscopy (SEM)

Fresh mucus samples were spread over the surface of a SEM imaging carbon disk and freeze-dried in situ following the aforementioned protocol. Freeze-dried mucus samples were gold-sputtered (QUORUM Q150R ES, Gala Instrument, Germany) and then transferred to the SEM (EVO HD15, Zeiss, Germany) for mucus-imaging.

2.5. Confocal Raman microscopy

Confocal Raman microscopy measurements of both, native and freeze-dried human tracheal mucus samples were performed using a WITec alpha 300R+ instrument (WITec GmbH, Ulm, Germany). The excitation source was a diode laser with a wavelength of 532 nm adjusted to a power of 30 mW. The setup was equipped with a Zeiss Epiplan Neofluar 50x objective (NA = 0.8), with maximal lateral and axial resolution of around 0.34 μm and 1.47 μm, respectively, and a 100x oil immersion objective (NA = 1.2), with maximal lateral and axial resolution of around 0.23 μm and 0.65 μm, respectively. Raman spectra were acquired with a spatial resolution of 0.5 μm; background subtracted and normalized to the most intense peak, and further converted into false color images using hierarchical cluster and basis analysis (WITec Project plus Software). In contrast to hierarchical cluster analysis as a binary approach, basis analysis is more sophisticated and involves Raman spectra of the pure compounds acquired from the sample as references. The false color image depicts the relative congruence of the spectra with the predefined reference spectra for each pixel. This approach is not binary and allows for a simultaneous weighted display of multiple components in one single pixel as visualized by color intensity differences.

2.6. Rheological measurements

Rheology experiments were conducted on an Anton-Paar MCR 102 rheometer (Graz, Austria) equipped with cone-plate geometry (diameter: 25 mm, cone angle: 2°) at controlled conditions (23.38 ± 0.5 °C). Frequency (ω) dependency of the storage modulus G' and the loss modulus G'' was measured in the range between 0.1 and 40 rad/s at a strain amplitudes of 1%, within the linear viscoelastic region. The experiments were conducted with fresh mucus samples (no treatment) and also with fresh mucus samples that had been incubated with NAC (100 mg/ml, 10% w/w) for 2 h.

3. Results and discussion

Even though the microstructure of human mucus can be visualized by electron microscopy, the localization of its individual chemical compounds in the complex hydrogel matrix is still unknown. To overcome this challenge, we applied confocal Raman microscopy to elucidate the localization of the mucus compounds with a chemically selective and thus label-free approach. Raman microscopy is based on laser light scattering and different chemical bonds can be differentiated by their unique scattering patterns. Initial studies probing lung mucus with Raman spectroscopy identified a strong scattering signal generated by lipids, predominantly triolein (Koljenović et al., 2004).

ARTICLE IN PRESS
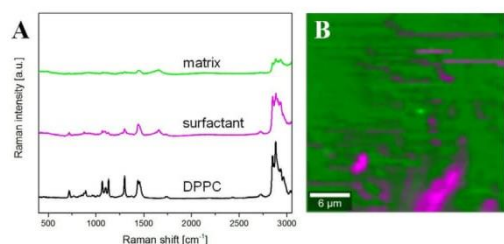
Fig. 2. Analysis of the native human airway mucus: (A) Single Raman spectra assigned to the mucus matrix, to pulmonary surfactant and to dipalmitoyl phosphatidylcholine (DPPC) as a reference, respectively; (B) False color Raman image representing the spatial distribution of the pulmonary surfactant in the mucus matrix (xy-scan). False colors depict the mucus matrix in green, and the pulmonary surfactant in pink, respectively. (For interpretation of the references to colour in this figure legend, the reader is referred to the web version of this article.)

As a first step in our study, we systematically investigated different mucus samples collected from human airways by Raman microscopy. After spectral assignment of the Raman peak patterns, we successfully differentiated individual signal contributions. Fig. 2 depicts a representative false color Raman image of human mucus with the mucus matrix (depicted in green, consisting of glycoproteins and lipids), as well as the pulmonary surfactant (depicted in pink). The surfactant spectrum is very distinctive and displays dipalmitoyl phosphatidylcholine (DPPC, Fig. 2A) as a major constituent of the pulmonary surfactant (Perez-Gil and Weaver, 2010). The most important spectral assignments of DPPC (reference spectrum presented in Fig. 2A) and surfactant-like spectra are: choline head group at $717\,cm^{-1}$, three distinct peaks at $1066\,cm^{-1}$, $1102\,cm^{-1}$ and $1128\,cm^{-1}$ representing the carbon backbone vibrations, and aliphatic ester at $1740\,cm^{-1}$.

As Raman imaging of the spatially resolved compound distribution within the mucus mesh was exacerbated by the samples' gel-like structure and the high water content, we freeze dried the mucus samples. Freeze-drying has already been reported as a valuable preparation technique for in vitro testing of the human skin and other tissues (Franzen et al., 2013) allowing for analysis of the mucus microstructure without chemical manipulation and fixation. However, we are aware that this and other fixation protocols may alter the pore size distribution of mucus (Schuster et al., 2013).

First, the ultrastructure of freeze-dried mucus was successfully visualized using SEM (Fig. 3A). It revealed the typical mesh-like structure with a highly heterogeneous pore size, ranging from pores in the nanoscale up to pores in the range of $1–10\,\mu m$. The structure is similar to native mucus which has previously been investigated by cryoSEM, thus suggesting that structural damage of the mucus mesh induced by the freeze drying process is most likely insignificant (Kirch et al., 2012). However, SEM images are limited to the morphological structure and cannot reveal the location of
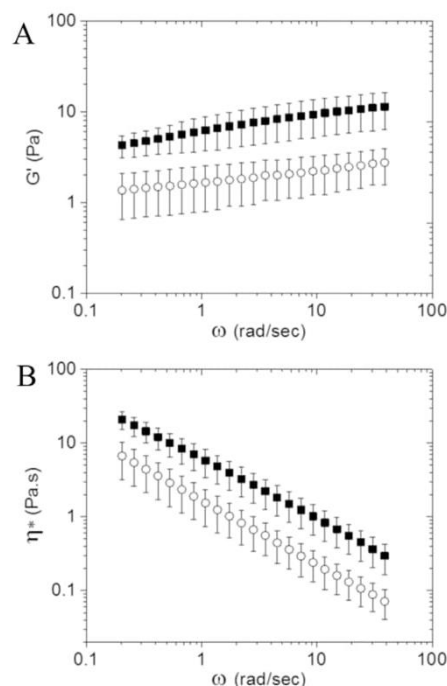

Fig. 4. Rheological properties of native tracheal mucus: (A) frequency (ω) sweep (0.2 to 40 rad/sec, strain 1%) showing the elastic modulus (G') of untreated (solid squares) and N-acetylcysteine-treated (NAC 10% w/w, empty circles) pulmonary mucus samples; (B) Complex viscosity (η^*) as a function of frequency (ω) of untreated (solid squares) and NAC-treated (10% w/w, empty circles) pulmonary mucus samples. N = 3 from independent mucus samples.

the chemical mucus building blocks (mucins, proteins, lipids) and their chemical interactions. Consequently, we applied Raman imaging for further chemically selective and label-free visualization. Two Raman spectra, one consisting of all prominent glycoprotein and lipid related peaks, representing the mucus matrix, and the other one consisting of peaks corresponding to disulfide bonds (-S-S-) at $492\,cm^{-1}$ and the surfactant related choline head group (-N +) at $717\,cm^{-1}$ were successfully identified. Fig. 3B displays the mucus matrix spectrum in red and the cysteine-rich domains in blue. The coexistence of the disulfide bonds and the choline headgroup in the blue spectrum can be explained by local hydrophobic interaction between the cysteine-rich domains (disulfide bonds) and the surfactant itself (choline headgroups) which coexist in the airway mucus, as confirmed after analysis of native airway mucus (Fig. 2). After conversion of the Raman spectra into false-color images, areas in which mucins interact by disulfide binding could be visualized (Fig. 3C). These
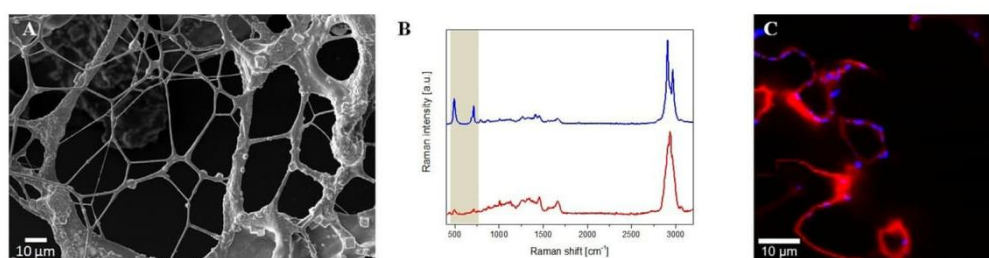
Fig. 3. Analysis of the freeze-dried mucus: (A) SEM image; (B) two individual single Raman spectra corresponding to the mucus matrix (red) and cysteine-rich domains (blue) with the spectral region of interest highlighted; (C) false color Raman image (same color coding like in 3B). (For interpretation of the references to colour in this figure legend, the reader is referred to the web version of this article.)

ARTICLE IN PRESS
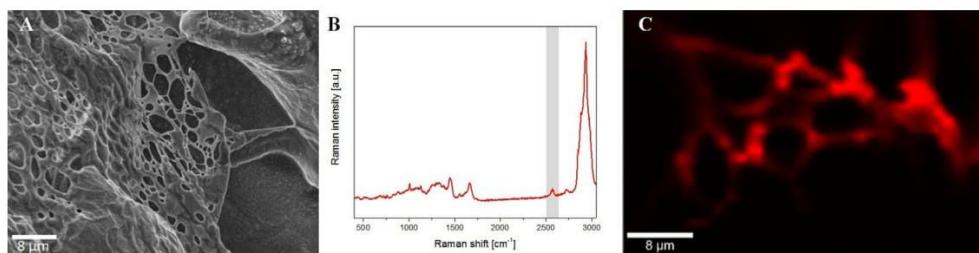
Fig. 5. Analysis of the freeze-dried mucus samples after treatment with N-acetylcysteine (NAC, 10% w/w): (A) SEM image; (B) Single Raman spectrum corresponding to the mucus matrix with the spectral region of interest highlighted; (C) false color Raman image (mucus matrix depicted in red). (For interpretation of the references to colour in this figure legend, the reader is referred to the web version of this article.)

areas, depicted in blue, were located in the edges of thin mucin fibers, thus most likely stabilizing the fragile macrostructure of human airway mucus.

Moreover, in order to investigate potential changes in the mucus microstructure upon mucolytic treatment, we incubated the human airway mucus with N-acetylcysteine (NAC, 10% w/w), as a therapeutic mucolytic agent (Yuan et al., 2015; Matera et al., 2016; Rubin, 2015). We performed rheological measurements with the mucus samples before and after treatment. The corresponding rheograms depict a significant decrease of the elastic modulus (G') arising from the chemical reduction of the inter-mucin disulfide bonds (Fig. 4A). In addition, the complex viscosity of mucus showed a marked decrease after NAC treatment in comparison to the untreated samples (Fig. 4B) (Yuan et al., 2015).

Additionally, SEM images of NAC-treated samples show a partially collapsed mesh structure (Fig. 5A) contrasting the structure of non-treated mucus (Fig. 3A).

Raman spectra of freeze dried mucus samples after mucolysis revealed the presence of free thiol (-SH) groups at 2560–2590 cm^{-1} (Fig. 5B, highlighted), thus proving the reduction of the disulfide bonds within the mucus matrix upon mucolytic treatment. In addition, no pure NAC signal can be detected after incubation of the mucus with NAC for two hours (data not shown). The false color Raman image presented in Fig. 5C reveals the presence of a mucus fiber-like structure even after chemical reduction with NAC, and similar pore size as shown with the corresponding SEM picture (Fig. 5A).

4. Conclusion

The airway mucus layer together with the alveolar pulmonary surfactant represents a major non-cellular pulmonary barrier to inhaled therapeutics. In this study, we investigated human airway mucus with confocal Raman microscopy to visualize and better understand its complex structure and composition. We successfully resolved the pulmonary surfactant from the mucus matrix in the native mucus hydrogel and revealed its spatial distribution. In the next step, we analyzed freeze-dried mucus discs before and after mucolytic treatment. Initially, we visualized cysteine rich domains (disulfide bonds), responsible for the structural stabilization of the mucus mesh. In contrast to this, upon mucolysis, we revealed the chemical reduction (thiol groups). Subsequently, we performed rheological measurements before and after mucolysis, proved the change of the viscoelastic properties, and correlated morphology and chemical structure of the mucus with its rheological characteristics. Our approach provides new insights into the airway mucus microstructure and brings Raman microscopy in focus as an upcoming tool for elucidation of the interaction mechanisms between the mucus and airborne threats, thus potentially contributing to more rational development of future lung therapeutics.

Author information

All authors have given approval to the final version of the manuscript. B.V. and X.M. contributed equally to this work.

References

Franzen, L., Vidlarova, L., Kostka, K.H., Schaefer, U.F., Windbergs, M., 2013. Exp. Dermatol. 22, 54.

Kim, M., Chen, W.G., Kang, J.W., Glassman, M.J., Ribbeck, K., Olsen, B.D., 2015. Adv. Mater. (Deerfield Beach, Fla.) 27, 4207.

Kirch, J., Schneider, A., Abou, B., Hopf, A., Schaefer, U.F., Schneider, M., Schall, C., Wagner, C., Lehr, C.M., 2012. Proc. Natl. Acad. Sci. U.S.A. 109, 18355.

Knowles, M.R., Boucher, R.C., 2002. J. Clin. Invest. 109, 571.

Koljenović, S., Bakker Schut, T.C., Van Meerbeeck, J.P., Maat, A.P.W.M., Burgers, S.A., Zondervan, P.E., Kros, J.M., Puppels, G.J., 2004. J. Biomed. Opt. 9, 1187.

Kumar, K., Castaño, E.J., Weidner, A.R., Yildirim, A., Goodwin, A.P., 2016. ACS Macro Lett. 5, 636.

Larhed, A.W., Artursson, P., Grasjo, J., Bjork, E., 1997. J. Pharm. Sci. 86, 660.

Matera, M.G., Calzetta, L., Cazzola, M., 2016. Expert Rev. Respir. Med. 10, 89.

Murgia, X., Pawelzyk, P., Schaefer, U.F., Wagner, C., Willenbacher, N., Lehr, C.-M., 2016. Biomacromolecules 17, 1536.

Nordgård, C.T., Nonstad, U., Ø. Olderøy, M., Espevik, T., Draget, K.I., 2014. Biomacromolecules 15, 2294.

Perez-Gil, J., Weaver, T.E., 2010. Physiol. (Bethesda) 25, 132.

Rubin, B.K., 2002. Respir. Care 47, 761.

Rubin, B.K., 2015. Respir. Care 60, 825.

Ruge, C.A., Kirch, J., Lehr, C.-M., 2013. Lancet Respir. Med. 1, 402.

Sakuma, S., Suita, M., Inoue, S., Marui, Y., Nishida, K., Masaoka, Y., Kataoka, M., Yamashita, S., Nakajima, N., Shinkai, N., Yamauchi, H., Hiwatari, K.-i., Tachikawa, H., Kimura, R., Uto, T., Baba, M., 2012. Mol. Pharm. 9, 2933.

Sanders, N.N., De Smedt, S.C., Van Rompaey, E., Simoens, P., De Baets, F., Demeester, J., 2000. Am. J. Respir. Crit. Care Med. 162, 1905.

Schuster, B.S., Suk, J.S., Woodworth, G.F., Hanes, J., 2013. Biomaterials 34, 3439.

Sevier, C.S., Kaiser, C.A., 2002. Nat. Rev. Mol. Cell Biol. 3, 836.

Sigurdsson, H.H., Kirch, J., Lehr, C.M., 2013. Int. J. Pharm. 453, 56.

Suk, J.S., Kim, A.J., Trehan, K., Schneider, C.S., Cebotaru, L., Woodward, O.M., Boylan, N.J., Boyle, M.P., Lai, S.K., Guggino, W.B., Hanes, J., 2014. J. Controlled Release 178, 8.

Yu, M., Wang, J., Yang, Y., Zhu, C., Su, Q., Guo, S., Sun, J., Gan, Y., Shi, X., Gao, H., 2016. Nano Lett..

Yuan, S., Hollinger, M., Lachowicz-Scroggins, M.E., Kerr, S.C., Dunican, E.M., Daniel, B. M., Ghosh, S., Erzurum, S.C., Willard, B., Hazen, S.L., Huang, X., Carrington, S.D., Oscarson, S., Fahy, J.V., 2015. Sci. Transl. Med. 7 (276ra27).

5.5   Synthesis of a Deuterated Probe for the Confocal Raman Microscopy Imaging of Squalenoyl Nanomedicines

Synthesis of a deuterated probe for the confocal Raman microscopy imaging of squalenoyl nanomedicines

E. Buchy, <u>B. Vukosavljevic</u>, M. Windbergs, D. Sobot, C. Dejean, S. Mura, P. Couvreur, D. Desmaele
Beilstein J. Org. Chem. **2016**, 12:1127-1135.

BEILSTEIN JOURNAL OF ORGANIC CHEMISTRY

Synthesis of a deuterated probe for the confocal Raman microscopy imaging of squalenoyl nanomedicines

Eric Buchy[1], Branko Vukosavljevic[2,3], Maike Windbergs[2,3], Dunja Sobot[1], Camille Dejean[4], Simona Mura[1], Patrick Couvreur[1] and Didier Desmaële[*1]

Full Research Paper

Address:
[1]Institut Galien (UMR CNRS 8612) Faculté de Pharmacie, Université Paris-Sud, 5, rue Jean-Baptiste Clément, 92296 Châtenay-Malabry, France, [2]Department of Drug Delivery, Helmholtz Centre for Infection Research and Helmholtz Institute for Pharmaceutical Research Saarland, Campus E8.1, 66123 Saarbruecken, Germany, [3]Biopharmaceutics and Pharmaceutical Technology, Saarland University, Campus A 4.1, 66123 Saarbruecken, Germany and [4]BIOCIS (UMR CNRS 8076) Faculté de Pharmacie, Université Paris-Sud, 5, rue Jean-Baptiste Clément, 92296 Châtenay-Malabry, France

Email:
Didier Desmaële[*] - didier.desmaele@u-psud.fr

* Corresponding author

Keywords:
deuterium labelling; nanomedicine; Raman spectroscopy; Shapiro reaction; squalene

Abstract

The synthesis of ω-di-(trideuteromethyl)-trisnorsqualenic acid has been achieved from natural squalene. The synthesis features the use of a Shapiro reaction of acetone-d_6 trisylhydrazone as a key step to implement the terminal isopropylidene-d_6 moiety. The obtained squalenic acid-d_6 has been coupled to gemcitabine to provide the deuterated analogue of squalenoyl gemcitabine, a powerful anticancer agent endowed with self-assembling properties. The Raman spectra of both deuterated and non-deuterated squalenoyl gemcitabine nanoparticles displayed significant Raman scattering signals. They revealed no differences except from the deuterium peak patterns in the silent spectral region of cells. This paves the way for label-free intracellular trafficking studies of squalenoyl nanomedicines.

Introduction

Application of nanotechnology to medicine holds promises to profoundly impact healthcare especially to treat severe diseases such as cancer, intracellular infections, neurodegenerative diseases, etc. Indeed, the nanometric size confers to drug delivery systems unique properties which improve the pharma- cokinetics and the biodistribution of many active compounds, thus increasing specificity, therapeutic efficacy and reducing systemic exposure and toxicity [1,2]. In recent years, many drug delivery systems have been developed covering all aspects of medicine. Among them, lipid drug conjugates (LDC) were

especially developed for the delivery of hydrophilic drugs by covalent coupling with lipid components [3,4]. In this context we recently found that the chemical conjugation of squalene, a natural and biocompatible triterpene, to a drug led to the formation of a prodrug that spontaneously self-assembled as nanoparticles in water. The advantage of this approach is a very high drug loading into the nanoparticles and the absence of burst release [5]. The proof of concept of this method has been done using gemcitabine (**2**), an anticancer chemotherapeutic drug used to treat various solid tumors [6]. Remarkably, the squalene conjugate of gemcitabine (GemSQ) self-assembled in aqueous media as nanoassemblies of around 100 nm mean particle size with a low polydispersity index. The nanosuspension exhibited impressively greater anticancer activity than free gemcitabine against different experimental tumor models [7-11] overcoming the main drawbacks of the parent drug such as its short biological half-life and its low intracellular diffusion [12,13]. Following these initial results, the squalenoylation method was extended to other nucleoside analogues such as antiretroviral agents, ddC, ddI and AZT [14] and to siRNA oligonucleotides [15]. More notably, squalenoylation of adenosine and the subsequent formation of NAs, allowed prolonged circulation of this nucleoside, providing neuroprotection in mice with induced focal cerebral ischemia and in rats undergoing spinal cord injury [16]. Interestingly, the "squalenisation platform" initially developed with highly hydrophilic therapeutics has been further extended to hydrophobic drugs such as beta-lactam antibiotics [17], paclitaxel [18], indolinone kinase inhibitors [19] or doxorubicin [20].

For the elucidation of the mechanisms involved in the efficacy of these promising nanomedicines, the precise knowledge regarding the cellular uptake, the intracellular localization and the determination of the subcellular interactions and trafficking is crucial. To fulfill this task, radioactive labeling or fluorescent probes have been thoroughly used. For example, the subcellular localization of the ^{3}H-radiolabeled GemSQ conjugate has been evaluated by micro-autoradiography coupled to confocal imaging of fluorescently labeled cellular structures [21]. A dual radioactive labeling ^{3}H,[14]C has been taken into profit to study the pharmacokinetics, the biodistribution and the metabolism of squalenoyl adenosine nanoparticles [22]. Nevertheless, the synthesis of labeled compounds is chemically challenging, expensive and submitted to drastic regulation rules. In addition, the use of fluorescent probes requires the covalent binding of large dye molecules (bodipy, cyanine, rhodamine etc, ...) to the drug conjugate, thus potentially modifying its physicochemical profile as well as the in vivo fate and the pharmacological activity. A simple encapsulation of an amphiphilic fluorochrome in LDC nanoparticles can be used as far as the colloidal stability of the nanocarrier is preserved, but cannot address the intracel-
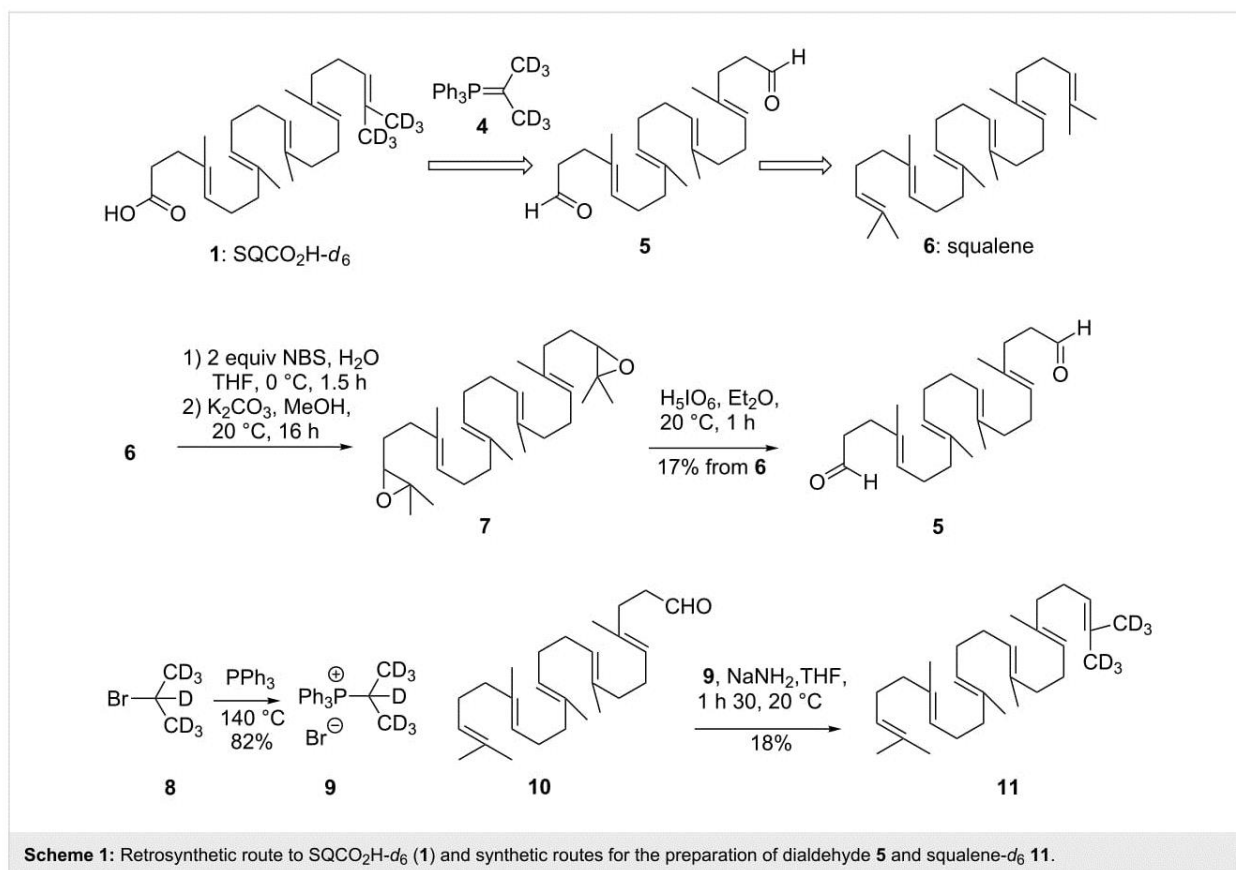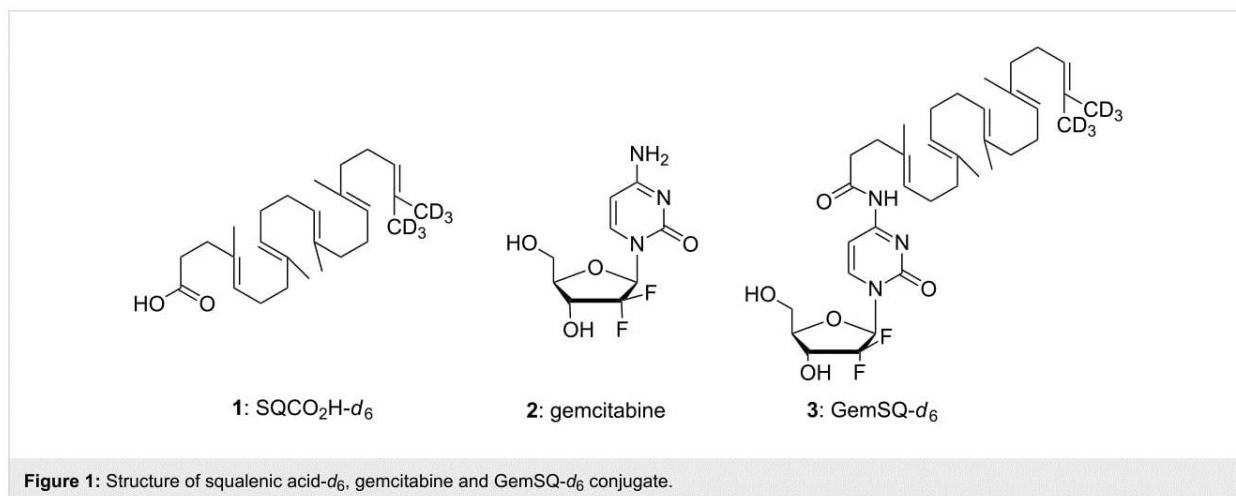
lular tracking of the loaded drug after carrier disassembling. Thus, specific tools such as fluorescence resonance energy transfer (FRET) and fluorescence quenching, have been developed to study the stability of nanoparticles [23].

In this context, Raman spectroscopy is an interesting technique which is based on the detection of scattered laser light upon irradiating the sample. Nevertheless, because of the low intensity of the Raman scattering, efficient in vivo confocal Raman microspectroscopy of cells had to wait until laser technology and mathematical image processing have made enough progress [24,25]. In contrast to fluorescence spectroscopy, Raman spectroscopy is label-free, as its scattering effect is unique for a specific molecular structure. Raman spectra of cells usually consist of spectral contributions from proteins, lipids and polysaccharides. For the simultaneous detection of both the drug and the cell components with the aim to investigate how they interact, a significant spectral contrast is required. Unfortunately, it can be hardly achieved when dealing with low drug concentrations or biological-like structures such as peptide drugs or nucleoside analogues. To overcome this issue, deuterium can be introduced to a sample molecule, as it exhibits a significant Raman signal at around 2200 cm^{-1}, which is in a so called "silent region" (1800–2800 cm^{-1}) of most biological molecules. For example as early as 1976, specifically deuterated stearic acids have been used by Sunder et al. in Raman studies and Stiebing et al. studied the uptake of arachidonic acid in human macrophages [26,27]. Furthermore, deuterium does not change the physicochemical properties and thus does not perturb the structure of the described NAs. Consequently, deuterated squalenic acid is expected to be excellent as bioorthogonal Raman tag for squalene-based NAs. Since the Raman signal intensity is expected to increase with the number of deuterium atoms in the same chemical environment, we have undertaken an effort directed towards the synthesis of ω-di-(trideuteromethyl)trisnorsqualenic acid (SQCO$_2$H-d_6, **1**) bearing six deuterium atoms on a non-labile position via isotopic exchange. We disclose herein the synthesis of this deuterated Raman probe from natural squalene, its coupling with gemcitabine and the Raman spectra of the deuterated GemSQ nanoassemblies, opening the way to perform intracellular imaging of squalenoyl nanomedicine (Figure 1).

Results and Discussion
Chemical synthesis of squalenic acid-d_6 and GemSQ-d_6 conjugate
In a first approach we decided to explore the selective Wittig mono-olefination of dialdehyde **5** readily accessible from the known 2,3;22,23-epoxysqualene (**7**) [28]. As depicted in Scheme 1, the synthetic sequence began with the treatment of squalene with two equivalents of NBS in a water/THF mixture.

Figure 1: Structure of squalenic acid-d_6, gemcitabine and GemSQ-d_6 conjugate.

Scheme 1: Retrosynthetic route to SQCO$_2$H-d_6 (**1**) and synthetic routes for the preparation of dialdehyde **5** and squalene-d_6 **11**.

After separation of the bis-bromohydrin from the monoproduct, potassium carbonate treatment gave the expected diepoxide **7**. Oxidative cleavage with periodic acid provided the corresponding dialdehyde **5** in 17% overall yield from squalene. The perdeuterated phosphonium salt **9** was obtained by simple condensation of commercially available 2-bromopropane-d_7 (**8**) with triphenylphosphine [29]. To our surprise, condensation of dialdehyde **5** with one equivalent of the ylide **4** (**9**, *n*-BuLi,
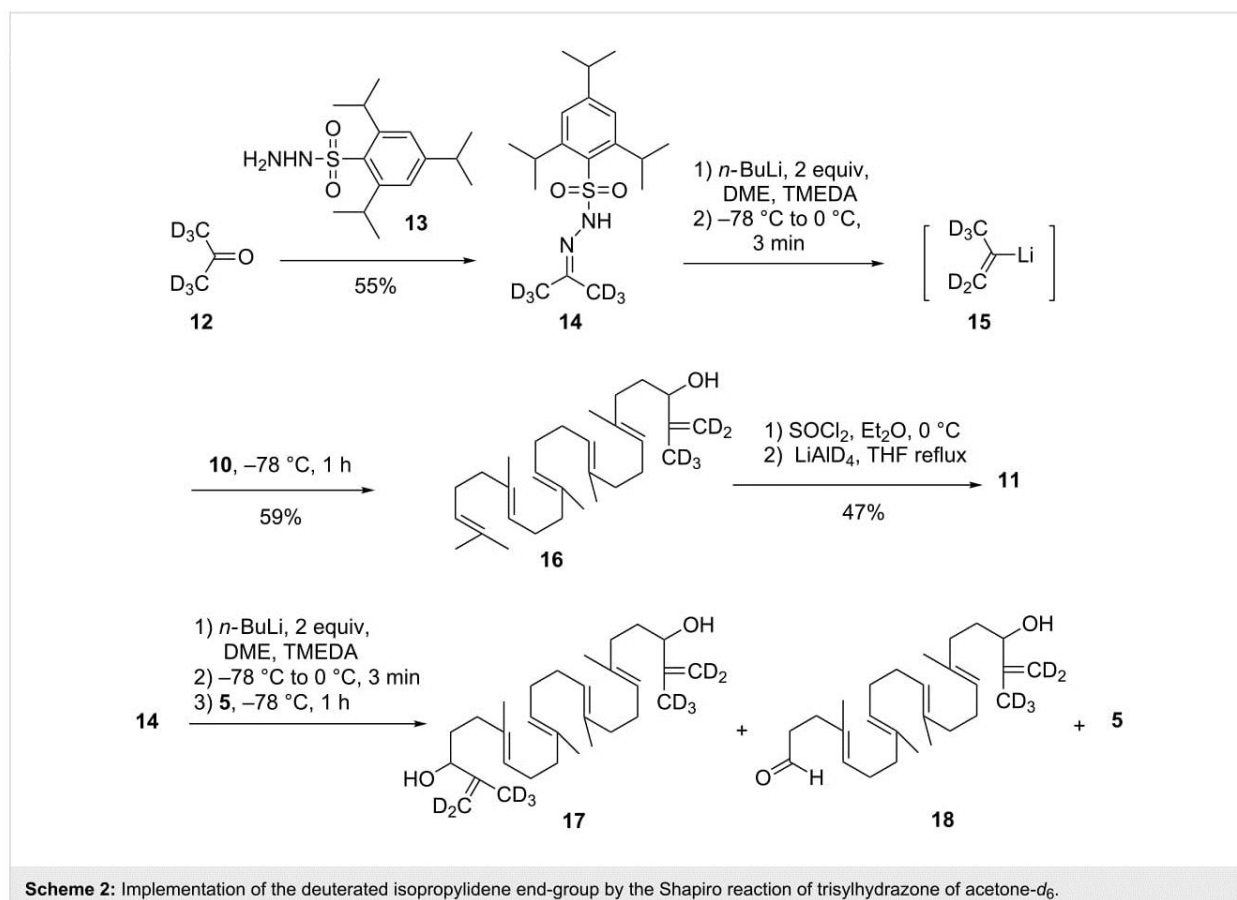
THF, −78 °C) did not afford any amount of the desired deuterated olefin but only polar material that could not be characterized. In an attempt to find more efficient reaction conditions, we investigated this reaction using the simple aldehyde **10** as a model compound, easily accessible from squalene according to the van Tamelen procedure [30]. The condensation of ylide **4** with **10** seemed to be an easy task, but many well-established procedures using various bases (*n*-BuLi, LiHMDS, NaH/

DMSO, PhLi) [29,31,32] gave only intractable materials. We finally found that the treatment of **10** with the "instant ylide mixture" of Schlosser made by grinding a solid mixture of **9** and NaNH$_2$ [33] delivered the desired squalene-d_6 (**11**) although in a low 18% yield. However, when applied to the dialdehyde **5** this procedure failed to give the expected Wittig adduct.

Whatever the origin of this problem, we decided to explore a new strategy based on a more nucleophilic deuterated synthon. In this regard we targeted prop-1-en-2-yllithium-d_5 (**15**) which is easily accessible through the Shapiro reaction of sulfonylhydrazone of acetone-d_6 [34,35]. Thus condensation of trisylhydrazine with acetone-d_6 (99.8% D) gave the expected hydrazone **14** in 55% yield. To our delight, upon treatment with two equivalents of *n*-BuLi and warming to 0 °C, the trisylhydrazone **14** afforded the vinyllithium reagent **15** (along with N$_2$ and the trisyl anion) which upon condensation with squalenaldehyde **10** furnished the desired allylic alcohol **16** in 59% yield. Reduction of the hydroxy group of **16** was straightforwardly achieved in 47% yield by treatment with a large excess of thionyl chloride followed by LiAlD$_4$ reduction [36]. Having secured an efficient method to reinstall the isopropylidene end-

group, we turned our attention to the application of this method to a two-end functionalized squalene derivative. However, when applied to dialdehyde **5** the Shapiro reaction led to a mixture of starting material (30%), allylic alcohol **18** (15%) and diol **17** (20%). This result could not by improved using reverse addition conditions (Scheme 2). Therefore, selective monoprotection of the dialdehyde **5** was next attempted. Unfortunately, treatment of the latter either with ethylene glycol or 2,2-dimethylpropandiol gave a mixture of di- and monoacetal whatever the conditions, as a new example of the lack of chemoselectivity of this long polyisoprenyl chain derivatives.

The differentiation of both ends of squalene was thus performed starting from trisnorsqualenaldehyde **10**. Protection of **10** as 2,2-dimethyl-1,3-dioxane derivative gave **19** in 96% yield which was further elaborated into aldehyde **20** in 16% overall yield according to the three-step van Tamelen sequence (i. NBS, THF, H$_2$O; ii. K$_2$CO$_3$, MeOH; iii. H$_3$IO$_6$, Et$_2$O) [30]. Interestingly enough, the 1,3-dioxane group survived the strongly acidic conditions of the oxidative cleavage. We next turned to the elaboration of the isopropylidene-d_6 moiety. In the event, the Shapiro reaction using trisylhydrazide **14** delivered the expected allylic alcohol **21** in 70% yield. The latter afforded

Scheme 2: Implementation of the deuterated isopropylidene end-group by the Shapiro reaction of trisylhydrazone of acetone-d_6.

67

the deuterated ketal **22** in 52% yield, upon sequential treatment with thionyl chloride and LiAlD$_4$ as described above. With the success of the implementation of the terminal deuterated isopropylidene group we turned our attention to the deprotection of the ketal and the oxidation of the aldehyde group. This seemingly trivial task, turned out to be unexpectedly challenging. All conditions tried (HCl 3 N, THF, 20 °C; HCl 3 N, THF, reflux; HCl 6 N, dioxane, 20 °C; HCO$_2$H, reflux; FeCl$_3$·6H$_2$O/SiO$_2$ [37], Jones reagent) either let the starting material unchanged or induced a complete decomposition. Even treatment with 1,2-ethanedithiol in the presence of BF$_3$·OEt$_2$ failed to give the corresponding thioketal [38]. These results clearly showed that another protecting group must be used, avoiding the use of an acidic catalyst that triggered the cyclization cascade of the polyisoprenyl chain (Scheme 3).

Despite this setback, the synthetic route seemed suitable to produce the desired material. Thus, the synthetic pathway described above was reimplemented starting from *tert*-butyldiphenylsiloxysqualene **23** readily obtained in 85% yield from squalenaldehyde **10** by NaBH$_4$ reduction followed by protection with *tert*-butyldiphenylsilyl chloride. Functionalisation of the opposite extremity of the polyisoprenoid chain using the van Tamelen sequence (i. 1 equiv NBS, THF, H$_2$O; ii. K$_2$CO$_3$, MeOH; iii. H$_3$IO$_6$, Et$_2$O) afforded the aldehyde **26** in 16% overall yield. Uneventfully, the Shapiro reaction with trisylhydrazone **14** produced the allylic alcohol **27**. Thionyl chloride treatment followed by LiAlD$_4$ reduction delivered directly the alcohol **28** in 41% yield through concomitant reduction of the intermediate allylic chloride and cleavage of the silyl protecting group. The reductive cleavage of *tert*-butyldiphenyl-silyl ethers by LiAlH$_4$ has been previously noticed [39]. Jones oxidation straightforwardly completed the synthesis
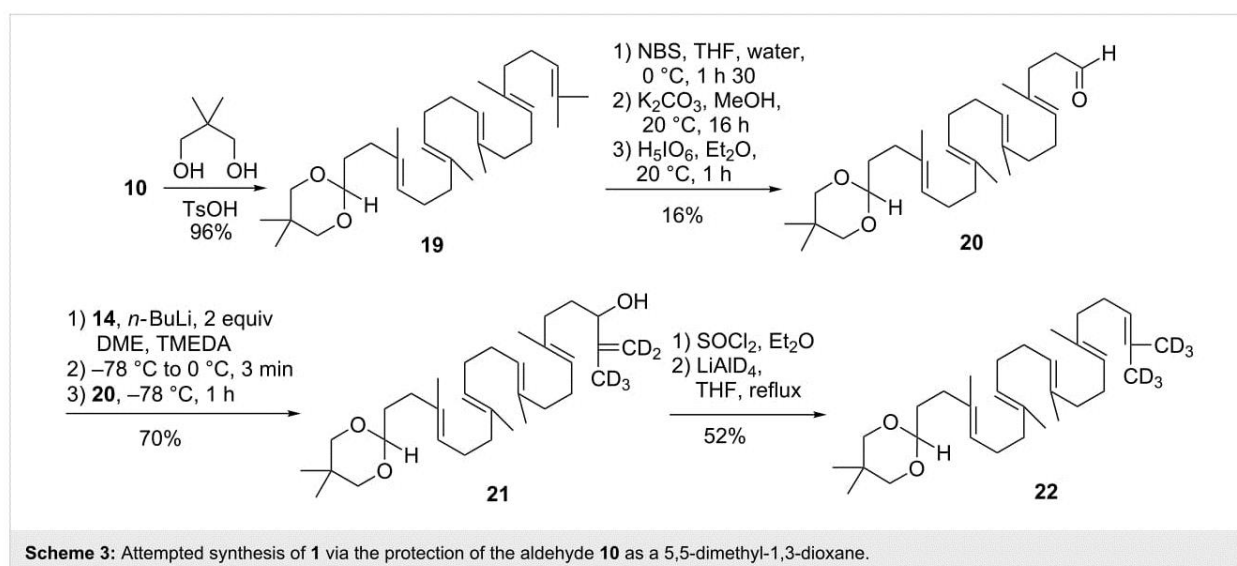
of SQCO$_2$H-d_6 **1**. Mass spectral analysis confirmed the presence of the six deuterium atoms (m/z = 405.3631 for [C$_{27}$H$_{37}$D$_6$O$_2^-$]) along a small amount (~5%) of SQCO$_2$H-d_5. GemSQ-d_6 **3** was next synthetized using activation with ethyl chloroformate as previously reported [7]. However, to optimize the process a large excess of gemcitabine was used in the reaction to increase the yield to 72% in respect of the more valuable SQCO$_2$H-d_6 (Scheme 4).
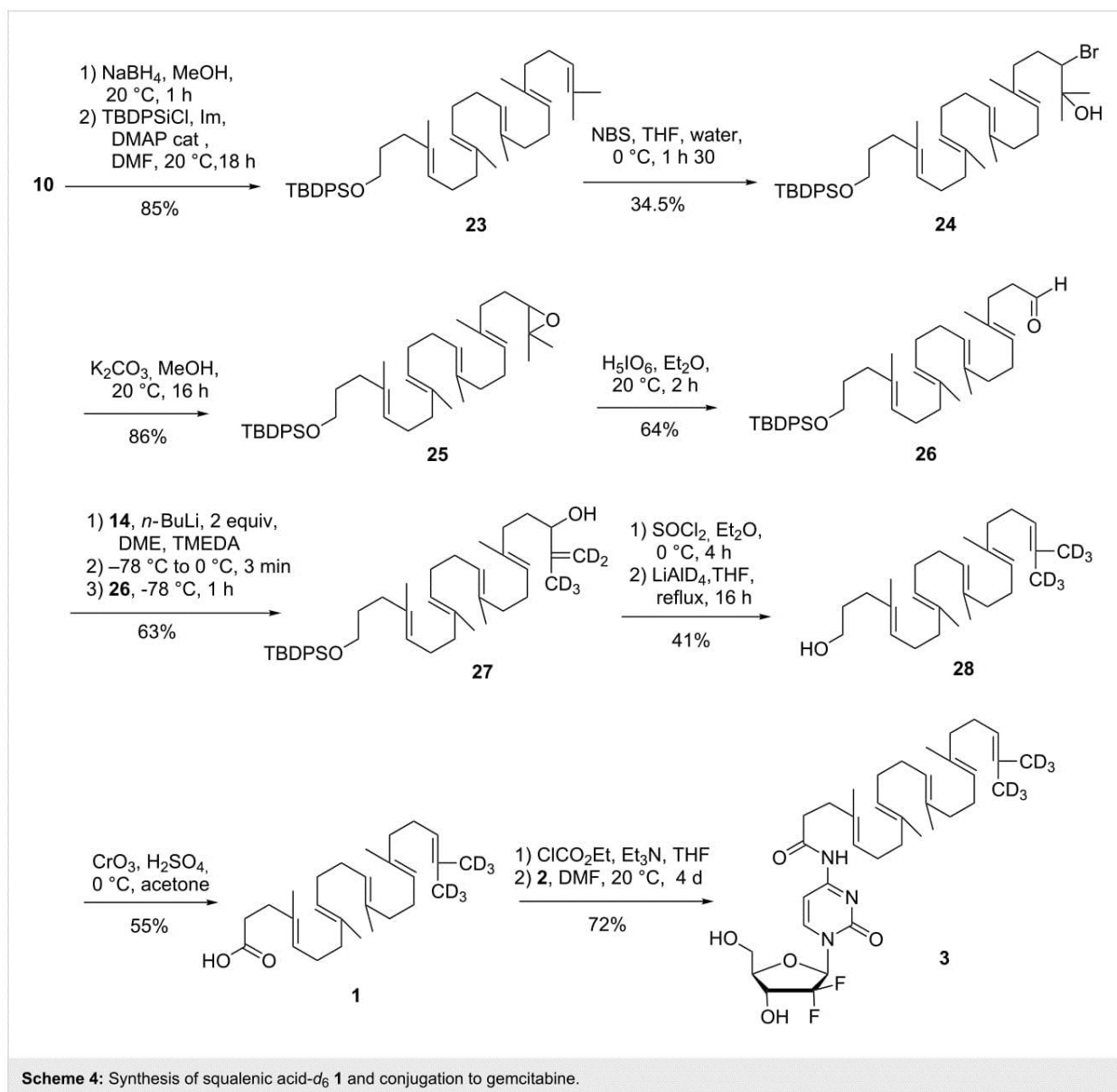
Nanoparticle formulation of the GemSQ-d_6 conjugate and Raman spectroscopy

The GemSQ and GemSQ-d_6 nanoassembly suspensions (2 mg·mL^{-1}) were prepared in a single step by nanoprecipitation of an ethanolic solution (2–4 mg·mL^{-1}) in milli-Q water [7]. After spontaneous formation of the NAs the organic solvent was evaporated under vacuum (Figure 2A). Single Raman spectra of the raw substances as well as of the particles were recorded (Figure 2B). As depicted in Figure 2C and Figure 2D, the Raman spectra of the deuterated and non-deuterated compounds revealed no differences except the deuterium peaks in the silent region.

Conclusion

A synthesis of squalenic acid-d_6 was developed through the Shapiro reaction of the sulfonylhydrazone of acetone-d_6 with an ω-silyloxysqualene aldehyde derivative followed by a regioselective reduction of the obtained allylic alcohol. This material was obtained from natural squalene in 0.6% yield over 12 steps. The synthesized deuterated squalenic acid was coupled to gemcitabine to provide the corresponding deuterated squalenoyl conjugate. Raman spectra of the nanoassemblies made of this conjugate were recorded, showing significant Raman peaks in the silent region of the cells thus making this material a poten-

Scheme 3: Attempted synthesis of **1** via the protection of the aldehyde **10** as a 5,5-dimethyl-1,3-dioxane.

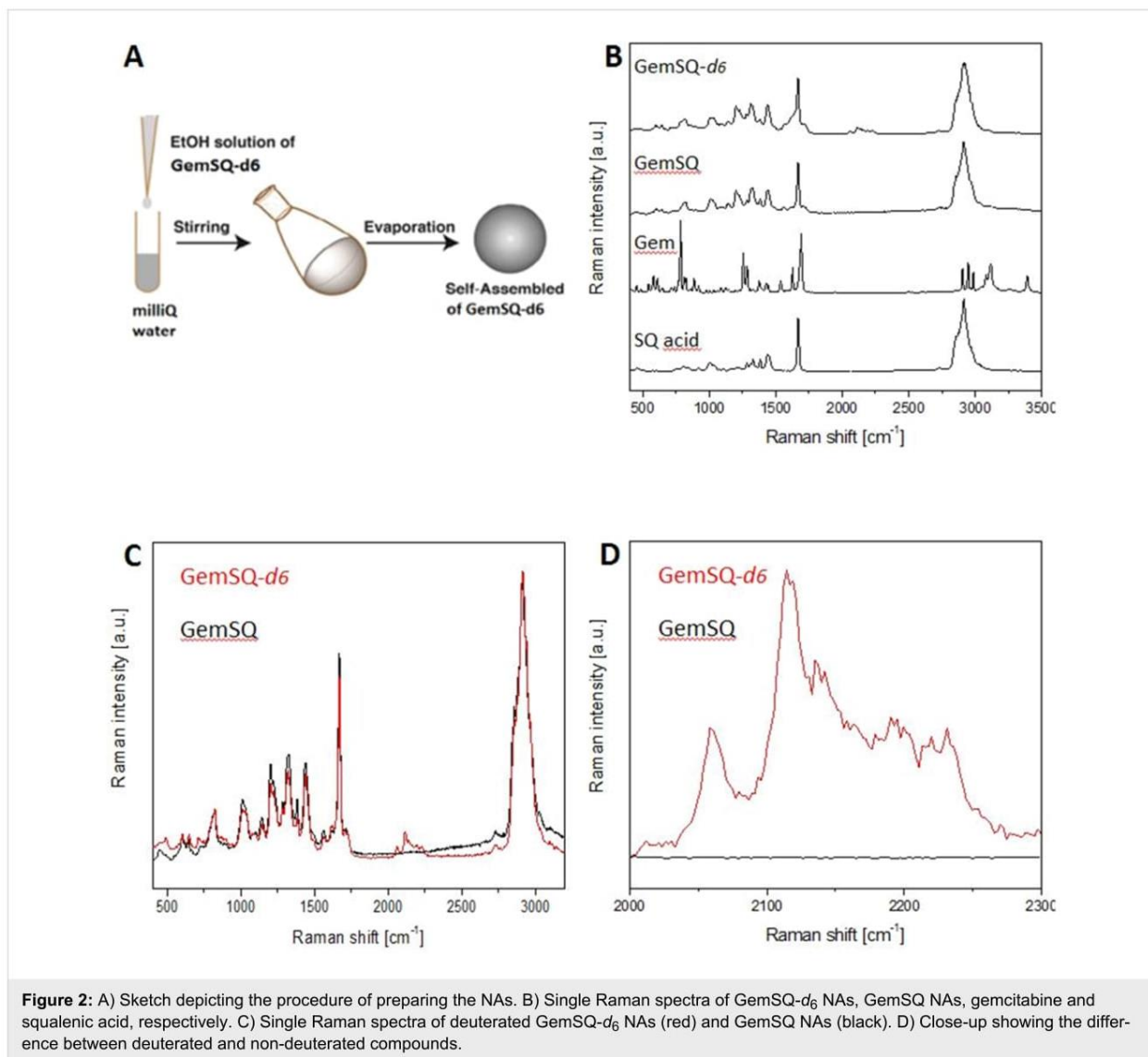**Scheme 4:** Synthesis of squalenic acid-d_6 **1** and conjugation to gemcitabine.

tial Raman probe. The use of this material as Raman probe in the study of the intracellular trafficking of GemSQ-based NAs is currently in progress and will be reported in due course.

Experimental

(4E,8E,12E,16E)-21-(^{2}H$_3$)methyl-4,8,13,17-tetramethyl(22,22,22-^{2}H$_3$)docosa-4,8,12,16,20-pentaenoic acid (1): An ice-cooled solution of alcohol **28** (55 mg, 0.14 mmol) in acetone (2 mL) was treated with a few drops of Jones reagent (CrO$_3$/H$_2$SO$_4$ 6 M) until the mixture took a persistent dark red color. After complete disappearance of the starting material a few drops of isopropanol were added. The mixture was taken into brine (10 mL) and extracted with Et$_2$O (4 × 15 mL), dried over MgSO$_4$ and concentrated under reduced pressure. The

crude product was purified by chromatography over silica gel eluting with petroleum ether/Et$_2$O 80:20 to give tris-norsqualenic acid-d_6 (**1**) as a colorless oil (31.5 mg, 55%). ^{1}H NMR (CDCl$_3$, 300 MHz) δ 5.19–5.07 (m, 5H, =C*H*), 2.45 (t, *J* = 7.6 Hz, 2H, C*H$_2$*CO$_2$H), 2.30 (t, *J* = 7.6 Hz, 2H, C*H$_2$*CH$_2$CO$_2$H), 2.15–1.95 (m, 16H, =HCC*H$_2$*C*H$_2$*C(CH$_3$)), 1.62 (s, 3H, (C*H$_3$*)C=), 1.60 (br s, 9H, (C*H$_3$*)C=); ^{13}C NMR (CDCl$_3$, 75 MHz) δ 179.2 (C, *C*O$_2$H), 135.3 (C, CH$_2$(CH$_3$)*C*=), 135.1 (C, CH$_2$(CH$_3$)*C*=), 135.0 (C, CH$_2$(CH$_3$)*C*=), 133.0 (C, CH$_2$(CH$_3$)*C*=), 131.2 (C, (CD$_3$)$_2$*C*=), 125.5 (CH, H*C*=), 124.6 (2CH, H*C*=), 124.4 (2CH, H*C*=), 39.9 (2CH$_2$), 39.7 (CH$_2$), 34.4(CH$_2$, *C*H$_2$CH$_2$CO$_2$H), 33.0 (CH$_2$, *C*H$_2$CO$_2$H), 28.4 (2CH$_2$), 26.9 (CH$_2$), 26.8 (2CH$_2$), 16.1 (3CH$_3$), 16.0 (CH$_3$); IR (film, cm^{-1}) ν: 3500–2600 (broad), 2962, 2916, 2856, 2222,

69

Figure 2: A) Sketch depicting the procedure of preparing the NAs. B) Single Raman spectra of GemSQ-d_6 NAs, GemSQ NAs, gemcitabine and squalenic acid, respectively. C) Single Raman spectra of deuterated GemSQ-d_6 NAs (red) and GemSQ NAs (black). D) Close-up showing the difference between deuterated and non-deuterated compounds.

2188, 1709, 1666, 1450, 1411, 1302, 1299, 1259, 1211, 1096, 1049, 955, 846, 736, 704; HRMS–ESI⁻: calcd for $C_{27}H_{37}D_6O_2$: 405.3645; found: 405.3631.

(4*E*,8*E*,12*E*,16*E*)-*N*-{1-[(2*R*,5*R*)-3,3-difluoro-4-hydroxy-5-(hydroxymethyl)oxolan-2-yl]-2-oxo-1,2-dihydropyrimidin-4-yl}-21-(²H₃)methyl-4,8,13,17-tetramethyl(22,22,22-²H₃)docosa-4,8,12,16,20-pentaenamide (3): To a solution cooled at −5 °C of trisnorsqualenic acid-d_6 (**1**) (31.5 mg, 0.077 mmol) in dry THF (0.6 mL) was sequentially added triethylamine (60 mg, 0.23 mmol) and ethyl chloroformate (10 mg, 0.093 mmol). The reaction mixture was stirred for 30 min at this temperature and a solution of gemcitabine base (60.6 mg, 0.23 mmol) in DMF (2 mL) was added. The reaction mixture was stirred for 4 days at 20 °C and concentrated under reduced pressure. The residue was directly chromatographed

over silica gel eluting with cyclohexane/AcOEt 4:1 followed by neat AcOEt to provide GemSQ-d_6 (**3**) as a colorless oil (36.0 mg, 72%). ¹H NMR (CDCl₃, 400 MHz) δ 9.15 (br s, 1H, N*H*CO), 8.10 (d, *J* = 7.5 Hz, 1H, H-6), 7.47 (d, *J* = 7.5 Hz, 1H, H-5), 6.18 (t, *J* = 7.4 Hz, 1H, H-1'), 5.20–5.06 (m, 5H, =C*H*), 4.55–4.41 (m, 1H, H-3'), 4.15–3.95 (m, 3H, H-4', H-5', O*H*), 3.91 (d, 1H, *J* = 10.8 Hz, H-5'), 2.55 (2H, t, *J* = 7.6 Hz, C*H₂*CON), 2.32 (2H, t, *J* = 7.4 Hz, C*H₂*CH₂CON), 2.10–1.91 (m, 16H, =CC*H₂*C*H₂*C(CH₃)), 1.60 (3H, s, =C(C*H₃*)), 1.59 (s, 6H, =C(C*H₃*)), 1.58 (3H, s, =C(C*H₃*)); ¹³C NMR (CDCl₃, 75 MHz) δ 173.6 (C, *C*ONH), 163.1 (C, C-4), 155.8 (C, C-2), 145.6 (CH, C-6), 135.3 (C, (CH₃)*C*= CH₂(CH₃)*C*=), 135.0 (2C, CH₂(CH₃)*C*=), 132.8 (C, CH₂(CH₃)*C*=), 131.2 (C, (CD₃)₂*C*=), 126.0 (CH, H*C*=), 124.5 (2CH, H*C*=), 124.4 (2 H*C*=), 122.5 (CF₂, t, *J* = 258 Hz, C-2'), 97.8 (CH, C-5), 81.8 (CH, C-4'), 69.3 (CH, m, C-3'), 60.0 (CH₂, C-5'), 39.9 (2CH₂), 39.7 (CH₂),

36.7 (CH_2, NHCOCH_2CH$_2$), 34.5 (CH_2, NHCOCH$_2CH_2$), 29.8 (CH_2), 28.4 ($2CH_2$), 27.0 (CH_2), 26.9 ($2CH_2$), 26.8 ($2CH_2$), 16.2 ($2CH_3$), 16.1 (CH_3), 16.0 (CH_3); IR (film, cm^{-1}) v: 3500–3000 (broad), 2979, 2932, 2872, 2852, 2222, 2191, 1724, 1683, 1660, 1618, 1561, 1494, 1433, 1397, 1383, 1365, 1337, 1320, 1312, 1272, 1206, 1194, 1134, 1086, 1069, 1051, 915, 893, 813, 787, 738; HRMS–ESI$^-$: calcd for $C_{36}H_{46}D_6N_3O_5F_2$: 650.4257; found: 650.4230.

Preparation of nanoassemblies from GemSQ and GemSQ-d_6: In a similar manner to the procedure published [19] the prodrugs based nanoparticle suspensions (2 mg·mL^{-1}) were prepared in a single step by dropwise addition of an ethanol solution (4 mg·mL^{-1}) in milli-Q water (1 mL) under vigorous stirring (500 rpm). Formation of NAs occurred immediately. After being stirred for 2 min, the nanoparticle suspension was then transferred into a weighted round bottom flask and ethanol was evaporated using a Rotavapor with a preheated water bath (35 °C) setting the vacuum to about 15–50 mbar for about 5 min. Then, the flask was dipped into a water bath (water temperature 37 °C) for about 3–5 minutes. Evaporation was continued till the weight of the contents decreased to 0.8–0.9 g. Then, the volume of the suspension in the flask was made-up to 1.0 g using either 5% dextrose solution or milli-Q water. The colloidal dispersions were stored at 4 °C.

Raman microscopy measurements. Confocal Raman microscopy measurements were performed with a WITec alpha 300R+ (WITec GmbH, Ulm, Germany). The excitation source was a diode laser with a wavelength of 532 nm adjusted to a power of 40 mW before the objective. A confocal pinhole of 50 μm rejected signals from out-of-focus regions. An objective with 50× magnification (N.A. 0.8, Epiplan Neofluar, Zeiss, Germany) was applied for acquiring single Raman spectra of the pure compounds with an integration time of 2 s and 10 accumulations. All spectra were background subtracted and normalized to the most intense peak.

Supporting Information

Supporting Information File 1
Experimental procedures and ^{1}H and ^{13}C NMR spectral data for compounds **1, 3, 11, 25, 27, 28**.
[http://www.beilstein-journals.org/bjoc/content/supplementary/1860-5397-12-109-S1.pdf]

Acknowledgements

References

1. Koo, O. M.; Rubinstein, I.; Onyuksel, H. *Nanomed.: Nanotechnol. Biol. Med.* **2005,** *1,* 193–212. doi:10.1016/j.nano.2005.06.004
2. Farokhzad, O. C.; Langer, R. *ACS Nano* **2009,** *3,* 16–20. doi:10.1021/nn900002m
3. Müller, R. H.; Mehnert, W.; Lucks, J. S.; Schwarz, C.; Mühlen, Z.; Weyhers, H.; Freitas, C.; Rühl, D. *Eur. J. Pharm. Biopharm.* **1995,** *41,* 62–69.
4. Olbrich, C.; Gessner, A.; Kayser, O.; Müller, R. H. *J. Drug Targeting* **2002,** *10,* 387–396. doi:10.1080/1061186021000001832
5. Desmaële, D.; Gref, R.; Couvreur, P. *J. Controlled Release* **2012,** *161,* 609–618. doi:10.1016/j.jconrel.2011.07.038
6. Burris, H. A., III; Moore, M. J.; Andersen, J.; Green, M. R.; Rothenberg, M. L.; Modiano, M. R.; Cripps, M. C.; Portenoy, R. K.; Storniolo, A. M.; Tarassoff, P.; Nelson, R.; Dorr, F. A.; Stephens, C. D.; Von Hoff, D. D. *J. Clin. Oncol.* **1997,** *15,* 2403–2413.
7. Couvreur, P.; Stella, B.; Reddy, L. H.; Hillaireau, H.; Dubernet, C.; Desmaële, D.; Lepêtre-Mouelhi, S.; Rocco, F.; Dereuddre-Bosquet, N.; Clayette, P.; Rosilio, V.; Marsaud, V.; Renoir, J.-M.; Cattel, L. *Nano Lett.* **2006,** *6,* 2544–2548. doi:10.1021/nl061942q
8. Reddy, L. H.; Renoir, J.-M.; Marsaud, V.; Lepetre-Mouelhi, S.; Desmaële, D.; Couvreur, P. *Mol. Pharmaceutics* **2009,** *6,* 1526–1535. doi:10.1021/mp900099e
9. Reddy, L. H.; Ferreira, H.; Dubernet, C.; Mouelhi, S. L.; Desmaële, D.; Rousseau, B.; Couvreur, P. *Anti-Cancer Drugs* **2008,** *19,* 999–1006. doi:10.1097/CAD.0b013e3283126585
10. Reddy, L. H.; Marque, P.-E.; Dubernet, C.; Lepêtre Mouelhi, S.; Desmaële, D.; Couvreur, P. *J. Pharmacol. Exp. Ther.* **2008,** *325,* 484–490. doi:10.1124/jpet.107.133751
11. Réjiba, S.; Reddy, L. H.; Bigand, C.; Parmentier, C.; Couvreur, P.; Hajri, A. *Nanomedicine* **2011,** *7,* 841–849. doi:10.1016/j.nano.2011.02.012
12. Gourdeau, H.; Clarke, M. L.; Ouellet, F.; Mowles, D.; Selner, M.; Richard, A.; Lee, N.; Mackey, J. R.; Young, J. D.; Jolivet, J.; Lafrenière, R. G.; Cass, C. E. *Cancer Res.* **2001,** *61,* 7217–7224.
13. Kim, M. P.; Gallick, G. E. *Clin. Cancer Res.* **2008,** *14,* 1284–1285. doi:10.1158/1078-0432.CCR-07-2247
14. Hillaireau, H.; Dereuddre-Bosquet, N.; Skanji, R.; Bekkara-Aounallah, F.; Caron, J.; Lepêtre, S.; Argote, S.; Bauduin, L.; Yousfi, R.; Rogez-Kreuz, C.; Desmaële, D.; Rousseau, B.; Gref, B.; Andrieux, K.; Clayette, P.; Couvreur, P. *Biomaterials* **2013,** *34,* 4831–4838. doi:10.1016/j.biomaterials.2013.03.022
15. Raouane, M.; Desmaele, D.; Gilbert-Sirieix, M.; Gueutin, C.; Zouhiri, F.; Bourgaux, C.; Lepeltier, E.; Gref, R.; Ben Salah, R.; Clayman, G.; Massaad-Massade, L.; Couvreur, P. *J. Med. Chem.* **2011,** *54,* 4067–4076. doi:10.1021/jm2000272
16. Gaudin, A.; Yemisci, M.; Eroglu, H.; Lepêtre-Mouelhi, S.; Turgoglu, O. F.; Dönmez-Demir, B.; Caban, S.; Fevzi Sargon, M.; Garcia-Argote, S.; Pieters, G.; Loreau, O.; Rousseau, B.; Tagit, O.; Hildebrandt, N.; Le Dantec, Y.; Mougin, J.; Valetti, S.; Chacun, H.; Nicolas, V.; Desmaële, D.; Andrieux, K.; Capan, Y.; Dalkara, T.; Couvreur, P. *Nat. Nanotechnol.* **2014,** *9,* 1054–1062. doi:10.1038/nnano.2014.274

17. Sémiramoth, N.; Di Meo, C.; Zouhiri, F.; Saïd-Hassane, F.; Valetti, S.;
    Gorges, R.; Nicolas, V.; Poupaert, J. H.; Chollet-Martin, S.;
    Desmaële, D.; Gref, R.; Couvreur, P. *ACS Nano* **2012,** *6,* 3820–3831.
    doi:10.1021/nn204928v

18. Caron, J.; Maksimenko, A.; Wack, S.; Lepeltier, E.; Bourgaux, C.;
    Morvan, E.; Leblanc, K.; Couvreur, P.; Desmaële, D.
    Adv. Healthcare Mater. **2013,** *2,* 172–185.
    doi:10.1002/adhm.201200099

19. Buchy, E.; Valetti, S.; Mura, S.; Mougin, J.; Trouff
lard, C.; Couvreur, P.;
    Desmaële, D. *Eur. J. Org. Chem.* **2015,** 202–212.
    doi:10.1002/ejoc.201403088

20. Maksimenko, A.; Dosio, F.; Mougin, J.; Ferrero, A.; Wack, S.;
    Reddy, L. H.; Weyn, A.-A.; Lepeltier, E.; Bourgaux, C.; Stella, B.;
    Cattel, L.; Couvreur, P. *Proc. Natl. Acad. Sci. U. S. A.* **2014,** *111,*
    E217–E226. doi:10.1073/pnas.1313459110

21. Bildstein, L.; Marsaud, V.; Chacun, H.; Lepêtre-Mouelhi, S.;
    Desmaële, D.; Couvreur, P.; Dubernet, C. *Soft Matter* **2010,** *6,*
    5570–5580. doi:10.1039/C0SM00342E

22. Gaudin, A.; Lepetre-Mouelhi, S.; Mougin, J.; Parrod, M.; Pieters, G.;
    Garcia-Argote, S.; Loreau, O.; Goncalves, J.; Chacun, H.;
    Courbebaisse, Y.; Clayette, P.; Desmaële, D.; Rousseau, B.;
    Andrieux, K.; Couvreur, P. *J. Controlled Release* **2015,** *212,* 50–58.
    doi:10.1016/j.jconrel.2015.06.016

23. Li, Y.; Budamagunta, M. S.; Luo, J.; Xiao, W.; Voss, J. C.; Lam, K. S.
    ACS Nano **2012,** *6,* 9485–9495. doi:10.1021/nn302317j

24. Antonio, K. A.; Schultz, Z. D. *Anal. Chem.* **2014,** *86,* 30–46.
    doi:10.1021/ac403640f

25. Kann, B.; Offerhaus, H. L.; Windbergs, M.; Otto, C.
    Adv. Drug Delivery Rev. **2015,** *89,* 71–90.
    doi:10.1016/j.addr.2015.02.006

26. Mendelsohn, R.; Sunder, S.; Berstein, H. J. *Biochim. Biophys. Acta*
    1976, *443,* 613–617.

27. Stiebing, C.; Matthäus, C.; Krafft, C.; Keller, A.-A.; Weber, K.;
    Lorkowski, S.; Popp, J. *Anal. Bioanal. Chem.* **2014,** *406,* 7037–7046.
    doi:10.1007/s00216-014-7927-0

28. Hauptfleisch, R.; Franck, B. *Tetrahedron Lett.* **1997,** *38,* 383–386.
    doi:10.1016/S0040-4039(96)02332-5

29. West, R.; Wang, Y.; Atkinson, J. *J. Labelled Compd. Radiopharm.*
    2008, *51,* 413–418. doi:10.1002/jlcr.1554

30. van Tamelen, E. E.; Curphey, T. J. *Tetrahedron Lett.* **1962,** *3,*
    121–124. doi:10.1016/S0040-4039(00)71112-9

31. Morimoto, Y.; Takeuchi, E.; Kambara, H.; Kodama, T.; Tachi, Y.;
    Nishikawa, K. *Org. Lett.* **2013,** *15,* 2966–2969. doi:10.1021/ol401081e

32. Murray, D. F. *J. Org. Chem.* **1983,** *48,* 4860–4864.
    doi:10.1021/jo00173a015

33. Schlosser, M.; Schaub, B. *Chimia* **1982,** *36,* 396–397.

34. Shapiro, R. H.; Heath, M. J. *J. Am. Chem. Soc.* **1967,** *89,* 5734–5735.
    doi:10.1021/ja00998a601

35. Surendra, K.; Corey, E. J. *J. Am. Chem. Soc.* **2008,** *130,* 8865–8869.
    doi:10.1021/ja802730a

36. Faulkner, D. J.; Petersen, M. R. *J. Am. Chem. Soc.* **1973,** *95,* 553–563.
    doi:10.1021/ja00783a040

37. Kim, K. S.; Song, Y. H.; Lee, B. H.; Hahn, C. S. *J. Org. Chem.* **1986,**
    51, 404–407. doi:10.1021/jo00353a027

38. Honda, Y.; Ori, A.; Tsuchihashi, G. *Chem. Lett.* **1987,** *16,* 1259–1962.
    doi:10.1246/cl.1987.1259

39. Rajashekhar, B.; Kaiser, E. T. *J. Org. Chem.* **1985,** *50,* 5480–5484.
    doi:10.1021/jo00350a007

5.6   Circulating Lipoprotein: a Trojan horse Guiding Squalenoylated Drugs to LDL-Accumulating Cancer Cells

Circulating lipoprotein: a Trojan horse guiding squalenoylated drugs to LDL-accumulating cancer cells

D. Sobot, S. Mura, M. Rouquette, B. Vukosavljevic, F. Cayre, E. Buchy, G. Pieters, M. Windbergs, D. Desmaele, P. Couvreur

Molecular Therapy
Original Article

AMERICAN SOCIETY of
GENE & CELL
THERAPY

Circulating Lipoproteins: A Trojan Horse Guiding Squalenoylated Drugs to LDL-Accumulating Cancer Cells

Dunja Sobot,[1] Simona Mura,[1] Marie Rouquette,[1] Branko Vukosavljevic,[2] Fanny Cayre,[1] Eric Buchy,[1] Grégory Pieters,[3] Sébastien Garcia-Argote,[3] Maike Windbergs,[2,4] Didier Desmaële,[1] and Patrick Couvreur[1]

[1]Institut Galien Paris-Sud, UMR 8612, CNRS, University Paris-Sud, Université Paris-Saclay, Faculté de Pharmacie, 5 rue Jean-Baptiste Clément, 92296 Châtenay-Malabry Cedex, France; [2]Department of Drug Delivery, Helmholtz Institute for Pharmaceutical Research Saarland, Helmholtz Center for Infection Research, Campus E8 1, 66123 Saarbruecken, Germany; [3]SCBM, CEA, Université Paris Saclay, LabEx LERMIT, 91191 Gif-sur-Yvette, France; [4]Institute of Pharmaceutical Technology, Buchmann Institute for Molecular Life Sciences, Goethe University, Max-von-Laue-Strasse 15, 60438 Frankfurt am Main, Germany

Selective delivery of anticancer drugs to rapidly growing cancer cells can be achieved by taking advantage of their high receptor-mediated uptake of low-density lipoproteins (LDLs). Indeed, we have recently discovered that nanoparticles made of the squalene derivative of the anticancer agent gemcitabine (SQGem) strongly interacted with the LDLs in the human blood. In the present study, we showed both in vitro and in vivo that such interaction led to the preferential accumulation of SQGem in cancer cells (MDA-MB-231) with high LDL receptor expression. As a result, an improved pharmacological activity has been observed in MDA-MB-231 tumor-bearing mice, an experimental model with a low sensitivity to gemcitabine. Accordingly, we proved that the use of squalene moieties not only induced the gemcitabine insertion into lipoproteins, but that it could also be exploited to indirectly target cancer cells in vivo.

INTRODUCTION

Selective delivery of anticancer compounds to tumor cells might be achieved by taking advantage of some unique features displayed by these cells, such as the increased metabolic requirements associated with their elevated proliferation rate.[1] For instance, higher amounts of cholesterol are essential for cell proliferation, in order to build more cell membranes.[2] This observation is supported by epidemiological studies that revealed a reduction in plasma cholesterol levels in patients suffering from certain types of cancer.[3–6] Later on, a high-fat diet-induced hypercholesterolemia was recognized as a factor of an enhanced aggressiveness in several animal tumor models.[7–9] In addition, a large number of emerging reports continue to reveal the complex role of cholesterol in cancer development and progression.[10–12] Intracellular cholesterol levels can be regulated by cancer cells through de novo synthesis or receptor-mediated uptake of low-density lipoproteins (LDLs), which are the main source of cholesterol for the peripheral tissues.[13] Uptake of LDLs is often used by fast proliferating cancer cells to satisfy their cholesterol needs, as supported by the observation that various hematological[14,15] and solid tumors[16–18] display an increased uptake of LDLs compared with healthy tissues.[3]
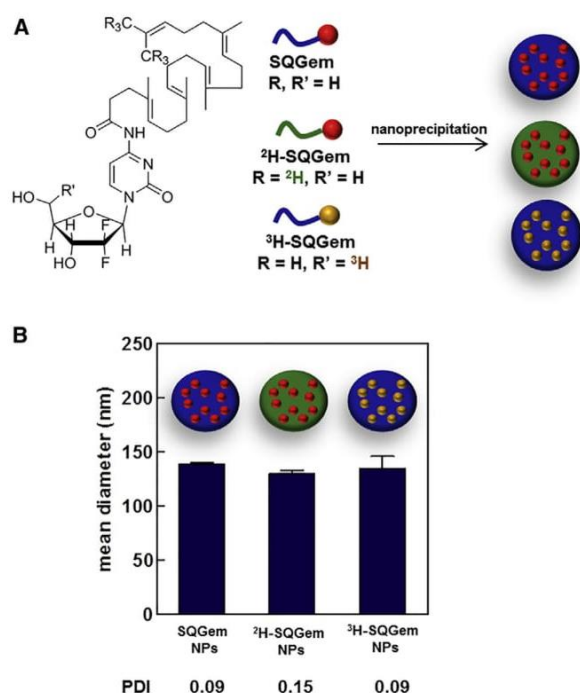
In this view, endogenous, long-circulating LDL particles have been proposed as delivery vehicles for lipophilic anticancer drugs.[18–20] LDL, an approximately 22-nm particle, is composed of a hydrophobic core containing cholesterol esters and triglycerides surrounded by a phospholipid monolayer containing free cholesterol and a single copy of apolipoprotein B-100 (apoB-100), which is responsible for the interaction with LDL receptors (LDLRs).[21,22] Many examples of increased efficacy of anticancer agents after their incorporation into LDL particles isolated from human plasma have been reported.[23–27] However, the main challenges of this approach rely on the complex isolation of LDLs from human plasma and their preservation in intact form, the potential pathogen contamination, the need for efficient drug loading techniques, as well as the limited stability of the resulting drug-LDL complexes.[26,28] In an attempt to overcome some of these drawbacks, synthetic LDL-like particles consisting of commercial lipids were developed.[29,30] Nevertheless, other difficulties (e.g., availability of apoB-100, batch reproducibility, and production costs) have thwarted this promising approach,[31,32] thus seriously hampering any further industrial development. In contrast to these somewhat complicated approaches, we have recently observed that it was possible to exploit the circulating lipoproteins as indirect natural carriers of intravenously administered drug molecules, if these drugs are equipped with a LDL affine moiety.[33]

The proof of concept of this approach has been achieved by the chemical linkage of the anticancer drug gemcitabine (Gem) to squalene (SQ; a natural lipid precursor of the cholesterol's biosynthesis), which additionally triggers the self-assembly of the SQ-drug bioconjugates into nanoparticles (SQGem NPs).[34] The conjugation

Figure 1. Structures of the Bioconjugates and Physico-chemical Properties of the NPs Used in This Study

(A) Chemical structures of SQGem, ^{2}H-SQGem, and ^{3}H-SQGem bioconjugates, and schematic representation of the corresponding unlabeled, deuterated, and tritiated NPs prepared according to the nanoprecipitation technique. Color changes as compared with the unlabeled bioconjugate highlight chemical modification on the SQ (green) or the Gem (yellow) moiety. (B) Mean diameter and polydispersity index (PDI) of SQGem, ^{2}H-SQGem, and ^{3}H-SQGem NPs.

to SQ has also allowed for reduction of Gem blood clearance and metabolization, and also achievement of improved anticancer efficacy on different experimental tumor models, compared with the free drug.[35,36] Moreover, we have recently discovered that by virtue of the bio-similarity between SQ and cholesterol (the natural load of lipoproteins), the SQGem bioconjugates were capable of spontaneously interacting and then being transported by plasma lipoproteins in the blood circulation, in particular via cholesterol-rich ones, both in vitro in human blood and in vivo in rodents, whereas the free drug did not interact with lipoproteins.[33] In the present study, whether the spontaneous interaction between SQGem NPs and LDLs (i.e., cholesterol-rich particles in humans) could mediate the targeting toward cancer cells with high LDLR activity has been investigated. We showed that the level of LDLRs positively affected the uptake and cytotoxicity of SQGem NPs in vitro, and the same behavior was observed also in vivo in tumor-bearing mice. These results provided evidence that the insertion of Gem into lipoproteins, driven by the SQ moiety, can be applied for indirect cancer cell targeting and improvement of the drug therapeutic profile.

RESULTS AND DISCUSSION

Preparation and Characterization of SQGem, ^{2}H-SQGem, and ^{3}H-SQGem NPs

The SQGem bioconjugate has been synthesized as previously described by chemical linkage of the 1,1',2-trisnorsqualenic acid onto the C-4 amino group of the Gem.[34] ^{2}H-SQGem was similarly prepared using hexadeutero-trisnorsqualenic acid, whereas ^{3}H-SQGem was obtained by coupling $5'$-^{3}H-Gem with 1,1',2-trisnorsqualenic acid. NPs were prepared by nanoprecipitation of the organic solution of SQGem in water and subsequent solvent evaporation. Deuterated (^{2}H-SQGem)[37] and tritiated (^{3}H-SQGem)[38] bioconjugates were used to track NPs and quantify their uptake (Figure 1A). Neither nanoparticle size nor polydispersity index was affected by the labeling procedures: size of nanoparticles was around 130 nm, displaying narrow size distribution (polydispersity index < 0.2) (Figure 1B).

SQGem and Gem Cytotoxicity and LDLR Expression in Cancer Cell Lines

The in vitro cytotoxicity of SQGem NPs and free Gem was assessed on human cancer cell lines using the 3-(4,5-dimethylthiazol-2-yl)-2,5-diphenyl tetrazolium bromide (MTT) viability assay. The choice of tested cell lines was based on: (1) the existing literature data concerning the correlation between the cholesterol uptake and the cancer progression, and/or (2) the clinical therapeutic indications for Gem.[39] Hence four different human cancer cell lines were chosen: lung cancer (A-549),[40,41] ovarian cancer (SK-OV-3),[42] and two breast cancer cell lines (MCF-7 and MDA-MB-231).[7,17] Cells were exposed to a range of different concentrations of SQGem NPs or free Gem for 72 hr; then the half maximal inhibitory concentration of cell proliferation (IC$_{50}$) was calculated. The IC$_{50}$ values measured for Gem on A-549, SK-OV-3, and MCF-7 cells were lower comparatively to SQGem NPs (Figures 2A–2C), in agreement with previous observations with other cell lines.[35,43] This is ascribed to the prodrug nature of SQGem, resulting in delayed cytotoxicity. An opposite behavior was instead observed with the MDA-MB-231 cells for which a 4-fold lower IC$_{50}$ value was observed with the SQGem NPs compared with the free drug (1.5 μM versus 6.8 μM) (Figure 2D). Among the four different cell lines, we had previously showed that the MDA-MB-231 displayed the highest expression of LDLRs.[33] Thus, the observed higher cytotoxicity of SQGem nanoparticles compared with the free drug, together with the overexpression of LDLRs, made this cell line an attractive tool to investigate the implication of LDLRs in SQGem uptake and pharmacological activity.

In Vitro and In Vivo SQGem Uptake in Breast Cancer Cells with Different LDLR Expression

The contribution of the LDLR in the cell uptake of SQGem NPs was further investigated on MDA-MB-231 and MCF-7 breast cancer cells, displaying respectively high and low levels of LDLR expression.[33] NP cell uptake and intracellular localization were visualized by confocal Raman microscopy, an emerging method for the analysis of therapeutics and their interactions with biological tissues.[44] Confocal Raman microscopy allows for chemically selective analysis, because different
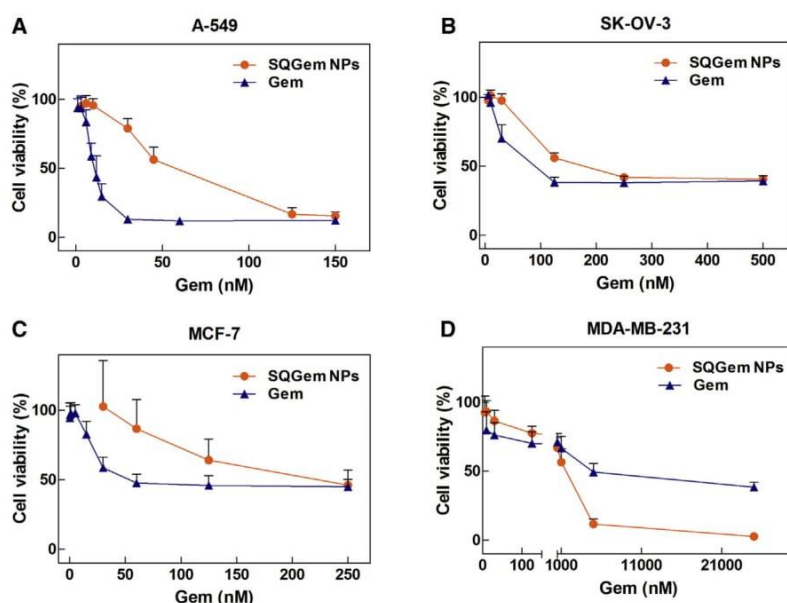
Figure 2. SQGem NPs and Gem Cytotoxicity

(A–D) Cell viability of (A) A-549, (B) SK-OV-3, (C) MCF-7, and (D) MDA-MB-231 cells treated with increasing concentrations of Gem as free drug or in the form of SQGem NPs for 72 hr at 37°C. Values represent mean ± SD.

cells with an inferior requirement for LDLs compared with cancer cells. Notably, these fibroblasts, similar to MCF-7 cells, displayed lower expression of LDLRs as compared with the MDA-MB-231 cells.[33] Incubation with ^{3}H-SQGem NPs at 37°C resulted in a higher radioactivity signal in MDA-MB-231 cells compared with MCF-7 and MRC-5 cells (Figure 5), thus confirming that a higher LDLR expression induced greater SQGem NP uptake. Such observation was in agreement with the results previously obtained in vivo on MDA-MB-231 and MCF-7 tumor-bearing mice fed a high-cholesterol diet in order to increase their level of circulating LDLs. Indeed, in xenografts originating from MDA-MB-231 cells (high LDLR expression), a 2-fold higher radioactivity signal was measured 6 hr post administration of a single dose of ^{3}H-SQGem NPs, compared with MCF-7 (low LDLR expression)-derived tumors.[33]

It has to be noted that, unlike the MCF-7 cells, the MDA-MB-231 cells satisfy their cholesterol needs mainly via uptake of circulating LDL particles, rather than by de novo cholesterol synthesis.[50,51] Such dependence on the LDL uptake was also supported by previous observations that human LDLs significantly increased the proliferation of the MDA-MB 231 cells[52] but not of the MCF-7 cells, in a dose-dependent manner.[53] Altogether, these data suggest that the specific metabolism of MDA-MB-231 cells may account for their higher uptake of SQGem NPs.

Additional studies have been performed on the MDA-MB-231 cell line by measuring the cell uptake of radiolabeled ^{3}H-SQGem NPs versus ^{3}H-Gem after 30 min, 2 hr, 4 hr, and 6 hr of incubation at 4°C and 37°C. The significantly higher uptake at 37°C, compared with 4°C (Figure 6A), clearly demonstrated that the cell capture of SQGem NPs was mainly obtained via an energy-dependent mechanism, which corroborated the hypothesis of a strong implication of LDLRs in nanoparticle uptake. Noteworthy is that the cell uptake of SQGem NPs was significantly higher compared with free Gem (Figure 6B), thus indicating that the cell internalization of this compound is rather mediated by transporters other than the LDLRs (e.g., nucleoside transporters).[54]

molecular structures scatter the laser light in different patterns. However, appropriate spectral assignment is frequently a challenge for cell imaging because each compartment (i.e., nucleus, cytoplasm, and intracellular lipid droplets) contributes to the overall Raman spectrum of the cell (Figure 3A), thus restraining differentiation of chemically similar compounds. The use of NPs resulting from the self-assembly of a deuterated SQGem bioconjugate (^{2}H-SQGem)[37] enabled differentiation of the endogenously similar Raman spectra of SQ-based NPs and intracellular lipid droplets (Figure 3B). Such deuterated SQGem NPs allowed for detection and visualization by confocal Raman microscopy even in the lipid-rich intracellular environment, based on the unique spectral bands of the deuterium isotope generated in the so-called silent region (around 2,200 cm^{-1}), in which no significant spectral contributions of other biomacromolecules are observed (Figure 3B).[45–49]

Confocal Raman microscopy images of both cell lines prior to NP incubation (control experiments) revealed that MDA-MB-231 cells were much more abundant in intracellular lipid droplets (cyan spots) than MCF-7 cells, thus indicating a difference in the lipid metabolism between the two cell lines (Figures 4A and 4B). Interestingly, these observations were in accordance with previous reports about the high lipid-accumulating character of MDA-MB-231 cells.[50] After 2 hr incubation with ^{2}H-SQGem NPs, a significant intracellular accumulation was observed in MDA-MB-231 cells (pink spots in Figure 4), whereas no NPs were detected in MCF-7 cells under the same conditions (Figures 4C and 4D), probably as a consequence of their lower LDLR expression.

Confocal Raman microscopy observations were confirmed by quantifying the uptake of tritiated SQGem NPs in these two breast cancer cell lines, as well as in MRC-5 fibroblasts chosen as a model of healthy

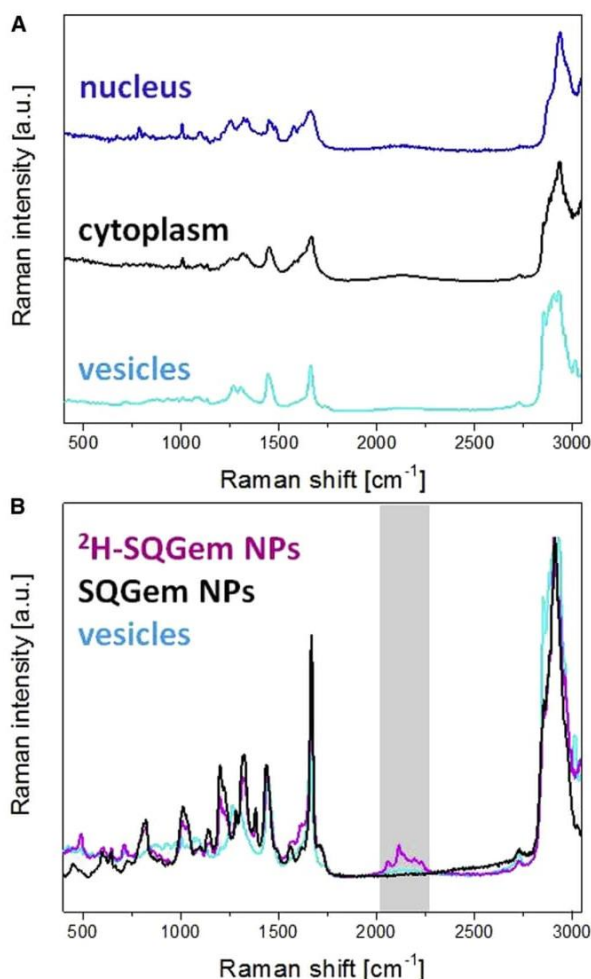### Influence of LDLR Activity and Expression on the Uptake in MDA-MB-231 Cells

Expression and availability of LDLRs on MDA-MB-231 cells have been tuned in order to further elucidate the involvement of LDLRs
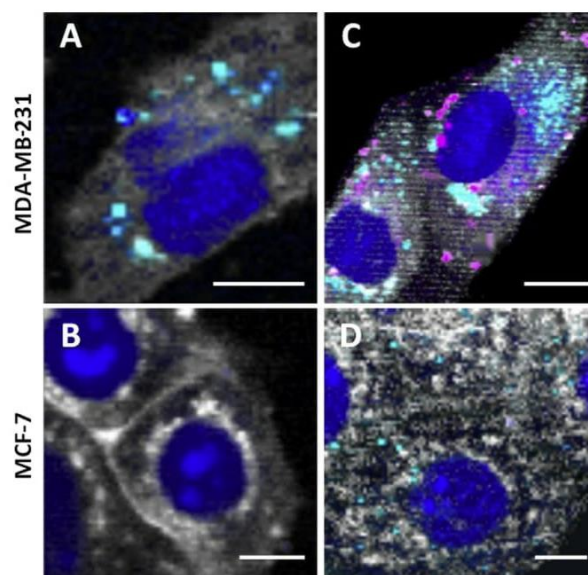
Figure 3. Raman Microscopy Spectra
(A) Single Raman spectra of nucleus, cytoplasm, and intracellular lipid droplets in MDA-MB-231 cells. (B) Raman spectra of lipid droplets, SQGem NPs, and ^{2}H-SQGem NPs. The region of interest is highlighted.

Figure 4. Confocal Raman Images of MDA-MB-231 and MCF-7 Breast Cancer Cell Lines Showing a Comparison of ^{2}H-SQGem NPs Uptake
(A and B) Representative images of non-treated MDA-MB-231 (A) and MCF-7 (B) cells (control). (C and D) MDA-MB-231 (C) and MCF-7 (D) cells incubated with NPs (77 μM) for 2 hr at 37°C. False-color Raman images were generated based on different scattering patterns of different cellular compartments. False colors visualize nucleus in dark blue, cytoplasm in white, lipid vesicles in cyan, and ^{2}H-SQGem in pink. Scale bars, 10 μm.

in the energy-dependent cell uptake of SQGem NPs. Because LDLs are the main source of exogenous cholesterol for the cell, the expression of LDLRs is normally regulated by the cellular demand of cholesterol.[55] Hence cholesterol-deprived cells cultivated in medium supplemented with lipoprotein (LP)-deficient serum (LPDS) would have an increased activity of LDLRs, whereas pre-saturation with an excess of LDLs would block the number of available LDLRs. Thus, the higher expression of LDLRs of MDA-MB-231 cells cultivated in a medium deficient in lipoproteins (LPDS-supplemented medium) has been confirmed by western blotting (Figure S1).

LDLR modifications clearly affected the cell uptake of ^{3}H-SQGem NPs. At any time point, the cell starvation with LPDS significantly increased ^{3}H-SQGem NPs cell uptake, whereas a competition with an excess of LDLs resulted in 2- to 3-fold reduction in the measured intracellular radioactivity signal (Figures 7A–7C, solid purple bars). In this study, SQGem NPs were diluted to the desired concentration with fetal bovine serum (FBS)-supplemented culture medium and incubated (30 min, 37°C) before addition to the cells, in order to allow the interaction between the SQGem bioconjugates and LPs present in the serum. These data confirmed the ability of LDL particles to mediate the SQGem NPs cellular uptake via the LDLRs. On the contrary, the uptake of free Gem remained unchanged regardless of the modification of LDLRs (Figures 7A–7C, solid blue bars), which was in agreement with the lack of interactions between free Gem and lipoproteins.[33] However, whether SQGem NPs could be cell-internalized via the LDLR without requiring the intervention of LDLs as intermediate carriers deserved to be further investigated. Thus, in order to investigate the capture of ^{3}H-SQGem NPs by MDA-MB-231 cells in the absence of any interaction between nanoparticles and lipoproteins, we performed an additional set of experiments according to the already used experimental conditions, except that SQGem NPs were diluted and preincubated with LPDS-supplemented medium, instead of FBS. Surprisingly, the cell uptake of ^{3}H-SQGem NPs (Figures 7A–7C, square pattern purple bars) was similar to that of nanoparticles preincubated with FBS-supplemented medium. On the other hand, the uptake of the free Gem was not affected by any of the experimental conditions (Figures 7A–7C, square pattern blue bars). Although these

www.moleculartherapy.org
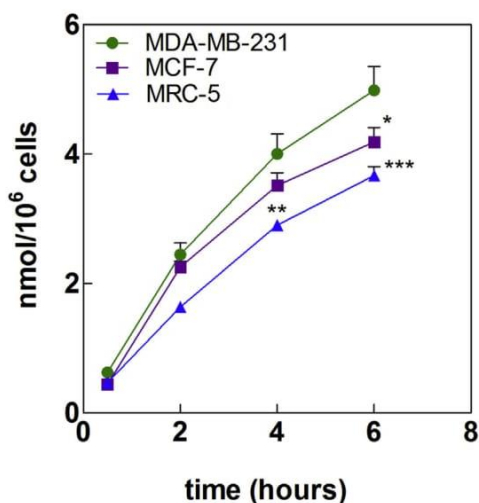
Figure 5. ^{3}H-SQGem NPs Uptake in MDA-MB-231, MCF-7, and MCR-5 Cells

Comparison of ^{3}H-SQGem NPs uptake after 30 min, 2 hr, 4 hr, and 6 hr incubation at 37°C. SQGem concentration: 10 μM. Results are expressed as nanomoles of Gem per million of cells. Data represent mean ± SEM (*p < 0.05; **p < 0.01; ***p < 0.001).

Figure 6. Uptake of ^{3}H-SQGem NPs and ^{3}H-Gem in the MDA-MB-231 Cell Line

(A) Comparison of ^{3}H-SQGem NPs (10 μM) uptake at 37°C and 4°C. (B) Comparison of ^{3}H-SQGem NPs (10 μM) and ^{3}H-Gem (10 μM) uptake at 37°C. Results are expressed as nanomoles of Gem per million cells. Bars represent mean ± SEM (**p < 0.01; ***p < 0.001; n = 3).

results suggested that the interaction of ^{3}H-SQGem NPs with LDLs was not mandatory for nanoparticle uptake via the LDLRs, it must be considered that the commercial LPDS used in this study contained still up to 5% of residual lipoproteins (as stated by the provider). Thus, it could not be excluded that this residual amount of lipoproteins (although low) might still mediate the cell uptake of the ^{3}H-SQGem NPs. Then, to completely ensure the absence of lipoproteins, a final experiment has been carried out by dilution and preincubation of SQGem NPs with the pure medium. In the total absence of LPs, there were clearly no differences concerning the uptake of ^{3}H-SQGem NPs by cells cultured in FBS- or LPDS-supplemented medium, although the latter overexpressed the LDLRs (Figure 7D, striped purple bars). These results confirmed that the establishment of preliminary interactions between SQ bioconjugates and lipoproteins was necessary to target LDL-accumulating cells such as MDA-MB-231.

Influence of the Diet on Circulating LDL Levels in Mice

Whether these results obtained in vitro could be transferred to in vivo animal tumor models deserved further investigation. However, the methodology to be used was not obvious, because important differences exist between the metabolism of lipids in humans and in rodents. In the former, the abundant LDL particle population carries about 75% of plasma cholesterol and represents the main source of cholesterol for peripheral tissues,[13] whereas in the latter, because of the lack of cholesteryl ester transfer from HDLs to LDLs and very low-density lipoproteins (VLDLs),[56] the amount of circulating plasma LDLs is almost negligible. To examine the role of the interaction of SQGem with LDLs and the LDLR-mediated uptake in vivo on xenografted tumor models, it was necessary to increase the amount of circulating LDLs in mice. Even though this increase could be achieved
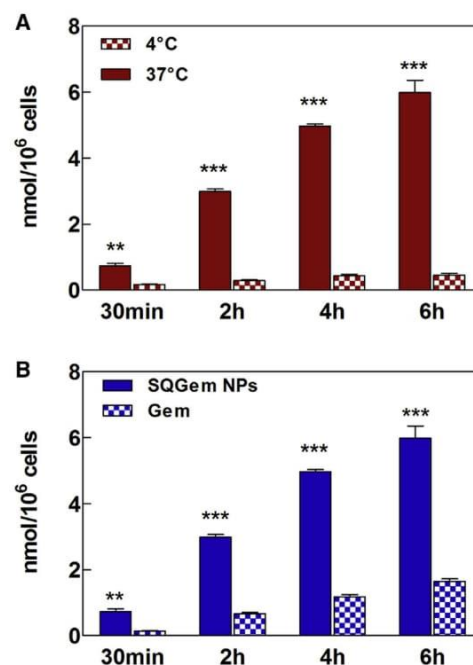
by simply using a diet with high cholesterol content, mice are known to be very resistant to elevated fat or cholesterol dietary intake and their response is highly strain dependent.[57] Accordingly, we have investigated the effect of a diet with high cholesterol content (2%) on three different immunodeficient mouse strains (SCID/beige, SCID/BALB/c, and Athymic nude) and compared the level of circulating LDLs with that of mice fed a chow diet with standard cholesterol (SC) content (<0.3%). Of note, the immunodeficient character was necessary to make these strains suitable for the development of human experimental tumors. The C57BL/6 strain was used as positive control because of its known sensitivity to a high-cholesterol diet.[58] Among the immunodeficient mice, only the athymic nude ones showed a clear increase (more than 2-fold) in LDL/VLDL circulating cholesterol level after 4 weeks on an high cholesterol diet (Figure S2). Accordingly, this strain was chosen for further studies.

In Vivo Anticancer Activity of SQGem NPs on MDA-MB-231 Tumor-Bearing Mice

Finally, we have investigated whether the SQGem/LDL interaction and the LDLR-mediated uptake could translate into increased in vivo anticancer activity on MDA-MB-231 tumor-bearing athymic mice fed a high cholesterol diet. This dietary intake started 4 weeks before
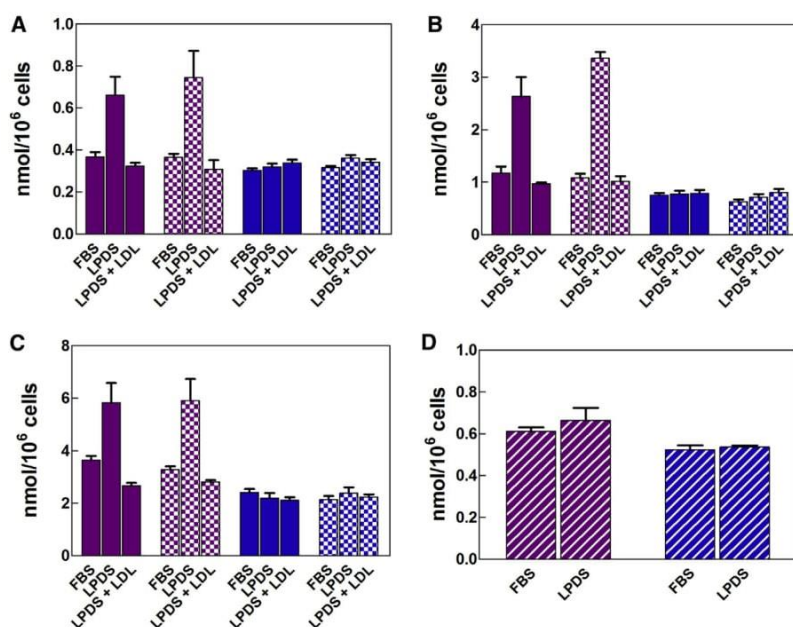
Figure 7. Cell Uptake of ^{3}H-SQGem NPs and ^{3}H-Gem as a Function of LDLR Expression and Availability

(A–C) MDA-MB-231 cells were cultured for 24 hr in medium supplemented with FBS, LPDS, or an excess of LDLs in LPDS-supplemented medium (LPDS + LDL) and then incubated with ^{3}H-SQGem NPs (10 μM) or ^{3}H-Gem (10 μM) for (A) 30 min, (B) 2 hr, or (C) 8 hr. Before addition to cells, ^{3}H-SQGem NPs and ^{3}H-Gem were diluted with FBS-supplemented medium (solid purple or blue bars, respectively) or LPDS-supplemented medium (square pattern purple or blue bars, respectively) and pre-incubated in these media for 30 min at 37°C. (D) MDA-MB-231 cells were cultured for 24 hr in medium supplemented with FBS or LPDS and then incubated with ^{3}H-SQGem NPs (10 μM) (striped purple bars) or ^{3}H-Gem (10 μM) (striped blue bars) for 30 min. Before addition to cells, ^{3}H-SQGem NPs and ^{3}H-Gem were diluted with pure medium and pre-incubated for 30 min at 37°C. Results are expressed as nanomoles of Gem per million cells. Bars represent mean ± SEM.

tumor induction. When tumors reached a volume of 100 mm³, mice were injected intravenously (days 0, 4, 8, and 14) with either SQGem NPs (10 mg/kg eq. Gem) or free Gem (10 mg/kg). Dextrose-treated mice were used as a control. Tumor growth was not affected by the treatment with the free Gem and overlapped the tumor progression in the control group. On the contrary, SQGem NPs induced a reduction in tumor volume ratio by 48% and 39% compared with dextrose and free Gem, respectively (Figure 8).

The superior in vivo anticancer activity of SQGem NPs over the free Gem is in agreement with the in vitro cytotoxicity results that showed that SQGem NPs inhibited the MDA-MB-231 cell growth at concentrations lower than did the free drug (Figure 2D). In vitro, IC$_{50}$ values also indicated a low sensitivity of this cell line to Gem, herein confirmed by the absence of any inhibitory effect of the free drug on the tumor progression. Nevertheless, in spite of this low inherent sensitivity to Gem, a significantly slower tumor growth was obtained when Gem was delivered in the form of SQ-based nanoparticles, probably as a consequence of the different mechanism of uptake and subsequent intracellular drug release. The obtained results clearly indicated the possibility that endogenous LDL particles can assist the targeting of the squalenoylated Gem toward the high LDLR-expressing MDA-MB-231 cells.

The high tendency of this tumor to accumulate LDL particles was confirmed by the dosage of the circulating LDL-cholesterol before and after the tumor induction. Indeed, even though the 4-week high cholesterol dietary intake resulted in a 2-fold increase in circulating LDL-cholesterol level, a significant reduction was measured 2 weeks after the grafting of the tumor cells (Figure S3), a trend that was not observed in healthy high cholesterol content diet-fed mice under the same experimental conditions, but without the tumor grafting. This observation is in accordance with numerous epidemiological studies that revealed a correlation between the reduction in circulating LDL level and cancer progression.

Conclusions

This study highlights that the strong affinity of SQ-Gem nanoparticles for circulating LDL confers an indirect targeting capability toward cancer cells with LDL-accumulating character, which results in significant anticancer efficacy, even in tumors with a low sensitivity to Gem. Although Gem is not the first-line treatment for breast cancer, the MDA-MB-231 breast cancer cell line used in this study enabled us to provide proof of concept of the feasibility of this "indirect" drug-targeting approach. Notably, it simply relies on spontaneous intravascular events and thus allows for overcoming the industrial hurdles in terms of isolation of human LDLs or synthesis of LDL-like particles. Importantly, we have previously demonstrated that the interaction with lipoproteins is not exclusive of SQGem but represents a more general concept common to different SQ derivatives. Accordingly, it opens an entirely new perspective, which may significantly advance the application of LDLs in drug delivery. Obviously, any clinical application would require taking into account the individual lipoprotein profile of each patient.

MATERIALS AND METHODS
### Materials
Gem hydrochloride was obtained from Sequoia Research Products, and 4-(N)-trisnorsqualenoyl-Gem (SQGem) was synthesized as previously reported.[34] ^{3}H-Gem hydrochloride was obtained from Moravek Biochemicals, whereas ^{3}H-SQGem and ^{2}H-SQGem were synthesized as described elsewhere.[33,37] Dexamethasone disodium phosphate was purchased from Fagron. Dextrose and cell culture

www.moleculartherapy.org
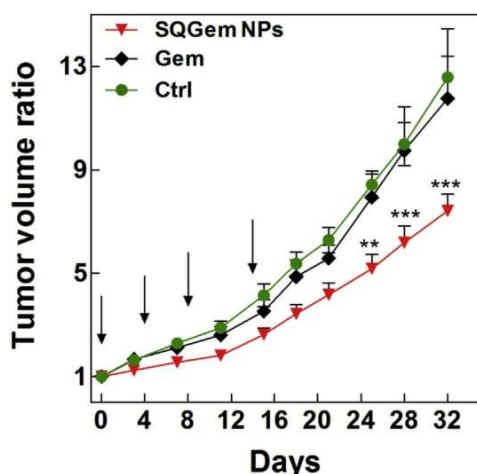
Figure 8. Tumor Growth Inhibition in MDA-MB-231 Tumor-Bearing Mice
All groups received four intravenous injections on days 0, 4, 8, and 14 in the lateral tail vein of: (1) SQGem NPs (10 mg/kg equivalent Gem), (2) Gem (10 mg/kg), or (3) dextrose 5% (control [Ctrl]). Tumor volume was regularly measured during the experimental period. The values represent mean ± SEM (n = 6). After 25 days, statistical analysis of tumor volume ratios showed superior antitumor efficacy of SQGem NPs compared with the other treatments (**p < 0.01; ***p < 0.001). Arrows point to treatment days.

media were obtained from Sigma-Aldrich. LDLs from human plasma were obtained from Thermo Fisher Scientific. Bidistilled MilliQ water was produced using a water purification system (Millipore).

Preparation and Characterization of SQGem Nanoparticles

SQGem nanoparticles (NPs) were prepared according to the nanoprecipitation technique. In brief, SQGem was dissolved in ethanol (2, 4, or 8 mg/mL) and then added drop by drop under magnetic stirring into 1 mL of MilliQ water (ethanol/water 0.5/1 v/v). Formation of NPs occurred spontaneously without addition of any surfactant. After solvent evaporation under reduced pressure, an aqueous suspension of SQGem NPs was obtained (final SQGem concentration 1, 2, or 4 mg/mL). For in vivo experiments, dextrose (5% w/v) was added to the final formulation. Mean particle size and polydispersity index were systematically determined after preparation by quasi-elastic light scattering at 25°C using a Malvern Zetasizer Nano ZS (Malvern Instrument). For deuterated and radiolabeled NPs, the deuterated (^{2}H-SQGem) or the tritiated bioconjugates (^{3}H-SQGem) were added into the ethanolic SQGem solution, and nanoparticles were then prepared as described above. Volume activity of radiolabeled NPs was 15.48 μCi/mL.

Cell Lines and Culture Conditions

Healthy human lung fibroblasts (MRC-5) and four human cancer cell lines (breast basal epithelial cells [MDA-MB-231 and MCF-7], ovarian adenocarcinoma cells [SK-OV-3], and adenocarcinoma alveolar basal epithelial cells [A-549]) were obtained from ATCC and maintained as recommended. In brief, MDA-MB-231 cells

were cultured in Leibovitz's L15 medium supplemented with 15% (v/v) FBS, glutamine (2 mM), and sodium hydrogen carbonate (20 mM). MCF-7 cells were grown in DMEM/Nutrient Mixture F-12 (DMEM-F12) supplemented with 10% (v/v) heat-inactivated (56°C, 30 min) FBS. SK-OV-3, A-549, and MRC-5 cells were cultured in McCoy's 5A, RPMI 1640, and Eagle's minimal essential medium (EMEM), respectively, supplemented with 10% (v/v) FBS. Penicillin (50 U/mL) and streptomycin (50 U/mL) (Lonza) were added to all media. Cells were maintained in a humid atmosphere at 37°C with 5% CO_2.

Cytotoxicity Assay

Cytotoxicity studies were performed using the MTT test. 100 μL of cell dispersion (3×10^4, 5×10^4, 5×10^4, and 1×10^5 cells/mL for A-549, SK-OV-3, MCF-7, and MDA-MB-231, respectively) was seeded in 96-well plates 24 hr before the treatment with serial dilutions of SQGem NPs or free Gem in culture media. After 72 hr incubation, 20 μL of a 5 mg/mL MTT (Sigma-Aldrich) solution in PBS was added to each well for 2 hr. Then, culture medium was removed and formazan crystals were dissolved in 200 μL of DMSO. Spectrophotometric measurements of the solubilized dye absorbance were performed on a microplate reader (LAB System Original Multiscan MS) at 570 nm. The cell viability for each treatment was calculated according to the ratio of the absorbance of the well containing treated cells versus the average absorbance of control wells (i.e., untreated cells). All experiments were repeated at least three times.

Role of Culture Medium on LDLR Expression

MDA-MB-231 cells were cultured for 24 hr in FBS or LPDS-supplemented medium. Then, cells were lysed in RIPA buffer (Sigma-Aldrich) supplemented with a phosphatases- and proteases-inhibitor cocktail (Sigma-Aldrich), vortexed, and centrifuged (15 min, 11,000 × g, 4°C). The concentration of extracted proteins was then measured using a colorimetric assay (Pierce BCA Protein Assay kit; Thermo Fisher Scientific). Equal amounts (30 μg) of proteins were incubated for 5 min at 99°C with Laemmli sample buffer supplemented with 5% β-mercaptoethanol (Bio-Rad) and then separated on SDS-polyacrylamide gels (Mini-Protean-TGX 4−15%; Bio-Rad). Separated proteins were further transferred to polyvinylidene difluoride (PVDF) membrane using a liquid transfer system (100 V, 45 min). After the blockage (5% dry milk suspension in 0.1% Tween 20 in Tris-buffered saline [TBS]), the membrane was first incubated for 2 hr at room temperature followed by an overnight incubation at 4°C with the primary antibody solution. The membrane was then washed 3 × 15 min in 0.1% Tween 20-TBS buffer and incubated for 1 hr with the secondary antibody solution. The following antibodies have been used in this study: rabbit monoclonal anti-LDLR antibody diluted 1/5,000 (ab52818; Abcam), mouse anti-β-actin antibody diluted 1/2,000 (AC-40; Sigma-Aldrich), goat anti-mouse secondary antibody conjugated to horseradish peroxidase diluted 1/4,000 (sc-2005; Santa Cruz Biotechnology), and goat anti-rabbit secondary antibody conjugated to horseradish peroxidase diluted 1/10,000 (sc-2004; Santa Cruz Biotechnology). Detection of chemiluminescence was performed using the Clarity Western ECL substrate (Bio-Rad Laboratories), and

images were captured by the ChemiBIS system from DNR Bioimaging Systems.

Visualization of the Cellular Uptake and Intracellular Localization by Confocal Raman Microscopy

Cellular uptake of deuterated squalenoyl nanoparticles (^{2}H-SQGem NPs) was performed using a confocal Raman microscope (WITec alpha 300R+; WITec). The excitation source was a 532 nm diode laser adjusted to a power of 30 mW and a 50 μm confocal pinhole rejecting signals from out-of-focus regions. A 63× immersion objective with an N.A. of 1.0 (Epiplan Neofluar; Zeiss) was applied for cellular uptake studies. A total of 50,000 cells/well (MDA-MB-231 and MCF-7) were seeded on calcium fluoride well plates 24 hr prior to the incubation with freshly prepared ^{2}H-SQGem NPs, opportunely diluted in cell culture medium, for 2 hr (final Gem concentration: 77 μM/well) at 37°C. At the end of the incubation period, cells were washed with phosphate buffer and fixed with 3% paraformaldehyde solution (30 min, at room temperature) prior to imaging. All acquired Raman spectral datasets were preprocessed by removing cosmic rays and by background signal reduction. Then, false-color Raman images were generated according to the different scattering patterns (unique Raman peaks) of the different cellular compartments. Chemometric post-processing of raw spectra is based on hierarchical cluster and basis analysis (WITec Project Plus software).

Evaluation of the Cellular Uptake by Liquid Scintillation Counting

For cellular uptake studies, MDA-MB-231, MCF-7, and MRC-5 cells (250,000 cells/well) were seeded in 12-well plates 24 hr prior to the incubation with ^{3}H-SQGem NPs or free ^{3}H-Gem diluted in culture medium (final Gem concentration/well: 10 μM, 0.1 μCi/mL) for 30 min, 2 hr, 4 hr, and 6 hr at 37°C or 4°C. At the end of the incubation period, cells were washed with 1 mL of PBS and then treated with 0.3 mL of 0.25% trypsin for 5 min at 37°C. The action of trypsin was stopped by adding 1 mL of culture medium, and the cellular suspension was centrifuged (200 × g, 5 min, 4°C), the supernatant discarded, and the cells dispersed in 1 mL of PBS. 10 μL of each cellular suspension was mixed with 10 μL of trypan blue (Sigma-Aldrich) for cell counting. The amount of cell-internalized ^{3}H-SQGem and ^{3}H-Gem was determined using a β-scintillation counter (Beckman Coulter LS6500). In brief, cell suspensions were first solubilized with 1 mL of Soluene-350 (PerkinElmer) at 50°C overnight prior to the addition of 10 mL of Hionic-Fluor scintillation cocktail (PerkinElmer). Finally, samples were vigorously vortexed for 1 min and kept aside for 2 hr prior to the counting.

Modification of the LDLR Activity and Evaluation of Cellular Uptake by Liquid Scintillation Counting and Flow Cytometry

Another set of experiments was performed to assess the influence of LDLR activity and/or expression on NP uptake. In this case, MDA-MB-231 cells (150,000 cells/well) in culture medium supplemented with FBS (control) or in lipoprotein-deficient serum (LPDS) (for LDLR modifications) were seeded in 24-well plates for 24 hr. Then, ^{3}H-SQGem NPs or free ^{3}H-Gem (both previously diluted in FBS or LPDS-supplemented culture medium or pure medium and preincu-

bated for 30 min at 37°C) were added to each well (final Gem concentration: 10 μM, 0.1 μCi/mL). Before the addition of ^{3}H-SQGem NPs or free ^{3}H-Gem preincubated 30 min in pure medium, cells were washed twice with PBS (1 mL) to ensure the complete removal of all serum components. Of note, the time point 30 min only was chosen in experiments in which pure medium has been used to limit the cell stress caused by non-physiological culture conditions.

For competition studies, cells cultured in LPDS-supplemented medium were preliminary incubated (30 min) with an excessive amount of LDLs (100 μg/mL). After 30 min, 2 hr, and 6 hr incubation, media were removed and cells were washed two times with 1% BSA-PBS (1 mL) and one time with PBS (1 mL) and then treated with 0.2 mL of 0.25% trypsin for 5 min at 37°C. The action of trypsin was stopped by adding 0.8 mL of culture medium, the cellular suspension was centrifuged (200 × g, 5 min, 4°C), supernatant was discarded, and cells were dispersed in 1 mL of PBS. 10 μL of the cellular suspension was then mixed with 10 μL of trypan blue (Sigma Aldrich) for cell counting. The amount of internalized ^{3}H-SQGem and ^{3}H-Gem was determined using a β-scintillation counter as previously described.

Animals

Four different strains of 4-week-old female mice (three immunodeficient [SCID BALB/c, SCID beige, and athymic nude] and one immunocompetent [C57BL/6]) were purchased from Envigo Laboratory. Animals were housed in an appropriate animal care facility during the experimental period. The experimental protocols were approved by the Animal Care Committee of the Université Paris-Sud in agreement with the principles of laboratory animal care and legislation in force in France.

Diet Influence

Four mice strains (at least nine mice each) over 4 weeks were fed either: (1) a chow diet containing a standard amount of cholesterol (<0.3%), or (2) a diet rich in cholesterol (2%) (TD.01383, Teklad diets; Envigo). At weeks 0, 2, and 4 after starting the diet intake, blood (0.2 mL) was collected by facial vein bleeding, and plasma was separated by centrifugation (1,300 × g, 15°C, 15 min). LDL/VLDL cholesterol levels in plasma were determined using the Abcam assay kit (ab65390) based on spectrophotometric cholesterol detection, according to the manufacturer's instructions. Mice were monitored regularly for body weight changes and health status.

In Vivo Anticancer Activity

The anticancer efficacy of SQGem NPs was evaluated on MDA-MB-231 tumor-bearing athymic nude mice fed a diet with high cholesterol content (TD.01383, Teklad diets; Envigo). Feeding started 4 weeks prior to tumor cells injection, and the diet was maintained for the entire duration of the experiment. 200 μL of MDA-MB-231 cell suspension in PBS (5×10^6 cells/mice) were injected subcutaneously into the upper portion of the right flank of mice. Tumors were allowed to grow until reaching a volume of ~100 mm^3 before initiating the treatment. Tumor length (a) and width (b) were measured with calipers,

www.moleculartherapy.org

and the tumor volume was calculated using the following equation: tumor volume (V) = (a × b²)/2. Tumor-bearing mice were randomly divided into three groups of at least six mice each. On days 0, 4, 8, and 14, mice received in the lateral tail vein four intravenous injections of either: (1) SQGem NPs at Gem equivalent dose of 10 mg/kg, (2) free Gem at 10 mg/kg, or (3) dextrose 5%. A pre-treatment with 5 mg/kg of dexamethasone was performed by intramuscular injection 4 hr before the treatment. Mice were monitored regularly for changes in tumor size, body weight, and health status. Mice were humanely sacrificed on day 32.

In order to evaluate whether tumor development could induce a modification in circulating LDL level, blood (200 μL) was collected from tumor-bearing mice, fed a high cholesterol content diet, by facial vein bleeding at weeks 0 (beginning of the experiment), 4 (after 4 weeks of feeding a cholesterol-rich diet), and 6 (2 weeks after tumor cells injection). As control, two groups of mice (not bearing the tumor) fed either a standard chow diet or a high-cholesterol-content diet were used. Blood samples were centrifuged (1300 × g, 15°C, 15 min), and LDL cholesterol plasma levels were measured using enzymatic essay (Laboratoire CERBA).

Statistical Analysis
All in vitro experiments were performed at least two times in duplicate or triplicate. For the in vivo experiments, each group counted at least six animals. Statistical analysis was performed with the Prism GraphPad 5.0 software. The significance was calculated using a two-way analysis of variance, followed by Bonferroni post-test.

SUPPLEMENTAL INFORMATION
Supplemental Information includes Supplemental Materials and Methods and three figures and can be found with this article online at http://dx.doi.org/10.1016/j.ymthe.2017.05.016.

AUTHOR CONTRIBUTIONS
P.C. and S.M. conceived and designed the research. D.S. designed and performed the nanoparticles preparation, the cellular studies, and the in vivo experiments. D.D. and E.B. developed and performed the SQGem and ²H-SQGem synthesis. G.P. and S.G.-A. developed and performed the radiolabeled compound synthesis. F.C. and M.R. helped with the cellular studies. M.W. and B.V. developed and performed the confocal Raman microscopy studies. P.C., S.M., D.S., D.D., M.W., and B.V. co-wrote the paper. All authors discussed the results and commented on the manuscript.

CONFLICTS OF INTEREST
The authors declare no conflict of interest.

REFERENCES
1. Hanahan, D., and Weinberg, R.A. (2011). Hallmarks of cancer: the next generation. Cell 144, 646–674.

2. Ho, Y.K., Smith, R.G., Brown, M.S., and Goldstein, J.L. (1978). Low-density lipoprotein (LDL) receptor activity in human acute myelogenous leukemia cells. Blood 52, 1099–1114.

3. Firestone, R.A. (1994). Low-density lipoprotein as a vehicle for targeting antitumor compounds to cancer cells. Bioconjug. Chem. 5, 105–113.

4. Vitols, S., Gahrton, G., Björkholm, M., and Peterson, C. (1985). Hypocholesterolaemia in malignancy due to elevated low-density-lipoprotein-receptor activity in tumour cells: evidence from studies in patients with leukaemia. Lancet 2, 1150–1154.

5. Al-Zoughbi, W., Huang, J., Paramasivan, G.S., Till, H., Pichler, M., Guertl-Lackner, B., and Hoefler, G. (2014). Tumor macroenvironment and metabolism. Semin. Oncol. 41, 281–295.

6. Siemianowicz, K., Gminski, J., Stajszczyk, M., Wojakowski, W., Goss, M., Machalski, M., Telega, A., Brulinski, K., and Magiera-Molendowska, H. (2000). Serum total cholesterol and triglycerides levels in patients with lung cancer. Int. J. Mol. Med. 5, 201–205.

7. Llaverias, G., Danilo, C., Mercier, I., Daumer, K., Capozza, F., Williams, T.M., Sotgia, F., Lisanti, M.P., and Frank, P.G. (2011). Role of cholesterol in the development and progression of breast cancer. Am. J. Pathol. 178, 402–412.

8. Alikhani, N., Ferguson, R.D., Novosyadlyy, R., Gallagher, E.J., Scheinman, E.J., Yakar, S., and LeRoith, D. (2013). Mammary tumor growth and pulmonary metastasis are enhanced in a hyperlipidemic mouse model. Oncogene 32, 961–967.

9. Zhuang, L., Kim, J., Adam, R.M., Solomon, K.R., and Freeman, M.R. (2005). Cholesterol targeting alters lipid raft composition and cell survival in prostate cancer cells and xenografts. J. Clin. Invest. 115, 959–968.

10. Silvente-Poirot, S., and Poirot, M. (2012). Cholesterol metabolism and cancer: the good, the bad and the ugly. Curr. Opin. Pharmacol. 12, 673–676.

11. Nelson, E.R., Chang, C.Y., and McDonnell, D.P. (2014). Cholesterol and breast cancer pathophysiology. Trends Endocrinol. Metab. 25, 649–655.

12. Kuzu, O.F., Noory, M.A., and Robertson, G.P. (2016). The role of cholesterol in cancer. Cancer Res. 76, 2063–2070.

13. Brown, M.S., and Goldstein, J.L. (1986). A receptor-mediated pathway for cholesterol homeostasis. Science 232, 34–47.

14. Vitols, S., Gahrton, G., Ost, A., and Peterson, C. (1984). Elevated low density lipoprotein receptor activity in leukemic cells with monocytic differentiation. Blood 63, 1186–1193.

15. Vitols, S., Angelin, B., Ericsson, S., Gahrton, G., Juliusson, G., Masquelier, M., Paul, C., Peterson, C., Rudling, M., Söderberg-Reid, K., et al. (1990). Uptake of low density lipoproteins by human leukemic cells in vivo: relation to plasma lipoprotein levels and possible relevance for selective chemotherapy. Proc. Natl. Acad. Sci. USA 87, 2598–2602.

16. Versluis, A.J., van Geel, P.J., Oppelaar, H., van Berkel, T.J., and Bijsterbosch, M.K. (1996). Receptor-mediated uptake of low-density lipoprotein by B16 melanoma cells in vitro and in vivo in mice. Br. J. Cancer 74, 525–532.

17. Rudling, M.J., Ståhle, L., Peterson, C.O., and Skoog, L. (1986). Content of low density lipoprotein receptors in breast cancer tissue related to survival of patients. Br. Med. J. (Clin. Res. Ed.) 292, 580–582.

18. Gal, D., Ohashi, M., MacDonald, P.C., Buchsbaum, H.J., and Simpson, E.R. (1981). Low-density lipoprotein as a potential vehicle for chemotherapeutic agents and radionucleotides in the management of gynecologic neoplasms. Am. J. Obstet. Gynecol. 139, 877–885.

82

19. Vitols, S. (1991). Uptake of low-density lipoprotein by malignant cells—possible therapeutic applications. Cancer Cells 3, 488–495.

20. Glickson, J.D., Lund-Katz, S., Zhou, R., Choi, H., Chen, I.-W., Li, H., Corbin, I., Popov, A.V., Cao, W., Song, L., et al. (2009). Lipoprotein nanoplatform for targeted delivery of diagnostic and therapeutic Aagents. In Oxygen Transport to Tissue XXX, P. Liss, P. Hansell, and D.F. Bruley, eds. (Springer US), pp. 227–239.

21. Van Antwerpen, R., and Gilkey, J.C. (1994). Cryo-electron microscopy reveals human low density lipoprotein substructure. J. Lipid Res. 35, 2223–2231.

22. Schumaker, V.N., and Adams, G.H. (1969). Circulating lipoproteins. Annu. Rev. Biochem. 38, 113–136.

23. Samadi-Baboli, M., Favre, G., Bernadou, J., Berg, D., and Soula, G. (1990). Comparative study of the incorporation of ellipticine-esters into low density lipoprotein (LDL) and selective cell uptake of drug–LDL complex via the LDL receptor pathway in vitro. Biochem. Pharmacol. 40, 203–212.

24. Koller-Lucae, S.K.M., Schott, H., and Schwendener, R.A. (1999). Low density lipoprotein and liposome mediated uptake and cytotoxic effect of N4-octadecyl-1-beta-D-arabinofuranosylcytosine in Daudi lymphoma cells. Br. J. Cancer 80, 1542–1549.

25. Vitols, S., Söderberg-Reid, K., Masquelier, M., Sjöström, B., and Peterson, C. (1990). Low density lipoprotein for delivery of a water-insoluble alkylating agent to malignant cells. In vitro and in vivo studies of a drug-lipoprotein complex. Br. J. Cancer 62, 724–729.

26. de Smidt, P.C., and van Berkel, T.J.C. (1990). Prolonged serum half-life of antineoplastic drugs by incorporation into the low density lipoprotein. Cancer Res. 50, 7476–7482.

27. Kader, A., and Pater, A. (2002). Loading anticancer drugs into HDL as well as LDL has little affect on properties of complexes and enhances cytotoxicity to human carcinoma cells. J. Control. Release 80, 29–44.

28. Lacko, A.G., Nair, M., Prokai, L., and McConathy, W.J. (2007). Prospects and challenges of the development of lipoprotein-based formulations for anti-cancer drugs. Expert Opin. Drug Deliv. 4, 665–675.

29. Rensen, P.C.N., de Vrueh, R.L.A., Kuiper, J., Bijsterbosch, M.K., Biessen, E.A.L., and van Berkel, T.J.C. (2001). Recombinant lipoproteins: lipoprotein-like lipid particles for drug targeting. Adv. Drug Deliv. Rev. 47, 251–276.

30. Ng, K.K., Lovell, J.F., and Zheng, G. (2011). Lipoprotein-inspired nanoparticles for cancer theranostics. Acc. Chem. Res. 44, 1105–1113.

31. Lackó, A.G., Stewart, D.R., McClain, R., Prókai, L., and McConathy, W.J. (2007). Recent developments and patenting of lipoprotein based formulations. Recent Pat. Drug Deliv. Formul. 1, 143–145.

32. Corbin, I.R., and Zheng, G. (2007). Mimicking nature's nanocarrier: synthetic low-density lipoprotein-like nanoparticles for cancer-drug delivery. Nanomedicine (Lond.) 2, 375–380.

33. Sobot, D., Mura, S., Yesylevskyy, S.O., Dalbin, L., Cayre, F., Bort, G., Mougin, J., Desmaële, D., Lepetre-Mouelhi, S., Pieters, G., et al. (2017). Conjugation of squalene to gemcitabine as unique approach exploiting endogenous lipoproteins for drug delivery. Nat. Commun., Published online May 30, 2017. http://dx.doi.org/10.1038/ncomms15678.

34. Couvreur, P., Stella, B., Reddy, L.H., Hillaireau, H., Dubernet, C., Desmaële, D., Lepêtre-Mouelhi, S., Rocco, F., Dereuddre-Bosquet, N., Clayette, P., et al. (2006). Squalenoyl nanomedicines as potential therapeutics. Nano Lett. 6, 2544–2548.

35. Reddy, L.H., Dubernet, C., Mouelhi, S.L., Marque, P.E., Desmaele, D., and Couvreur, P. (2007). A new nanomedicine of gemcitabine displays enhanced anticancer activity in sensitive and resistant leukemia types. J. Control. Release 124, 20–27.

36. Reddy, L.H., Marque, P.-E., Dubernet, C., Mouelhi, S.-L., Desmaële, D., and Couvreur, P. (2008). Preclinical toxicology (subacute and acute) and efficacy of a new squalenoyl gemcitabine anticancer nanomedicine. J. Pharmacol. Exp. Ther. 325, 484–490.

37. Buchy, E., Vukosavljevic, B., Windbergs, M., Sobot, D., Dejean, C., Mura, S., Couvreur, P., and Desmaële, D. (2016). Synthesis of a deuterated probe for the confocal Raman microscopy imaging of squalenoyl nanomedicines. Beilstein J. Org. Chem. 12, 1127–1135.

38. Reddy, L.H., Khoury, H., Paci, A., Deroussent, A., Ferreira, H., Dubernet, C., Declèves, X., Besnard, M., Chacun, H., Lepêtre-Mouelhi, S., et al. (2008). Squalenoylation favorably modifies the in vivo pharmacokinetics and biodistribution of gemcitabine in mice. Drug Metab. Dispos. 36, 1570–1577.

39. Hui, Y.F., and Reitz, J. (1997). Gemcitabine: a cytidine analogue active against solid tumors. Am. J. Health Syst. Pharm. 54, 162–170, quiz 197–198.

40. Vitols, S., Peterson, C., Larsson, O., Holm, P., and Åberg, B. (1992). Elevated uptake of low density lipoproteins by human lung cancer tissue in vivo. Cancer Res. 52, 6244–6247.

41. Gueddari, N., Favre, G., Hachem, H., Marek, E., Le Gaillard, F., and Soula, G. (1993). Evidence for up-regulated low density lipoprotein receptor in human lung adenocarcinoma cell line A549. Biochimie 75, 811–819.

42. Filipowska, D., Filipowski, T., Morelowska, B., Kazanowska, W., Laudanski, T., Lapinjoki, S., Akerlund, M., and Breeze, A. (1992). Treatment of cancer patients with a low-density-lipoprotein delivery vehicle containing a cytotoxic drug. Cancer Chemother. Pharmacol. 29, 396–400.

43. Bildstein, L., Dubernet, C., Marsaud, V., Chacun, H., Nicolas, V., Gueutin, C., Sarasin, A., Bénech, H., Lepêtre-Mouelhi, S., Desmaële, D., and Couvreur, P. (2010). Transmembrane diffusion of gemcitabine by a nanoparticulate squalenoyl prodrug: an original drug delivery pathway. J. Control. Release 147, 163–170.

44. Kann, B., Offerhaus, H.L., Windbergs, M., and Otto, C. (2015). Raman microscopy for cellular investigations—From single cell imaging to drug carrier uptake visualization. Adv. Drug Deliv. Rev. 89, 71–90.

45. Stiebing, C., Matthäus, C., Krafft, C., Keller, A.-A., Weber, K., Lorkowski, S., and Popp, J. (2014). Complexity of fatty acid distribution inside human macrophages on single cell level using Raman micro-spectroscopy. Anal. Bioanal. Chem. 406, 7037–7046.

46. Matthäus, C., Krafft, C., Dietzek, B., Brehm, B.R., Lorkowski, S., and Popp, J. (2012). Noninvasive imaging of intracellular lipid metabolism in macrophages by Raman microscopy in combination with stable isotopic labeling. Anal. Chem. 84, 8549–8556.

47. Chernenko, T., Sawant, R.R., Miljkovic, M., Quintero, L., Diem, M., and Torchilin, V. (2012). Raman microscopy for noninvasive imaging of pharmaceutical nanocarriers: intracellular distribution of cationic liposomes of different composition. Mol. Pharm. 9, 930–936.

48. van Manen, H.-J., Lenferink, A., and Otto, C. (2008). Noninvasive imaging of protein metabolic labeling in single human cells using stable isotopes and Raman microscopy. Anal. Chem. 80, 9576–9582.

49. Matthäus, C., Kale, A., Chernenko, T., Torchilin, V., and Diem, M. (2008). New ways of imaging uptake and intracellular fate of liposomal drug carrier systems inside individual cells, based on Raman microscopy. Mol. Pharm. 5, 287–293.

50. Antalis, C.J., Arnold, T., Rasool, T., Lee, B., Buhman, K.K., and Siddiqui, R.A. (2010). High ACAT1 expression in estrogen receptor negative basal-like breast cancer cells is associated with LDL-induced proliferation. Breast Cancer Res. Treat. 122, 661–670.

51. Antalis, C.J., Uchida, A., Buhman, K.K., and Siddiqui, R.A. (2011). Migration of MDA-MB-231 breast cancer cells depends on the availability of exogenous lipids and cholesterol esterification. Clin. Exp. Metastasis 28, 733–741.

52. Rodrigues dos Santos, C.R., Domingues, G., Matias, I., Matos, J., Fonseca, I., de Almeida, J.M., and Dias, S. (2014). LDL-cholesterol signaling induces breast cancer proliferation and invasion. Lipids Health Dis. 13, 16.

53. Rotheneder, M., and Kostner, G.M. (1989). Effects of low- and high-density lipoproteins on the proliferation of human breast cancer cells in vitro: differences between hormone-dependent and hormone-independent cell lines. Int. J. Cancer 43, 875–879.

54. Damaraju, V.L., Damaraju, S., Young, J.D., Baldwin, S.A., Mackey, J., Sawyer, M.B., and Cass, C.E. (2003). Nucleoside anticancer drugs: the role of nucleoside transporters in resistance to cancer chemotherapy. Oncogene 22, 7524–7536.

55. Ho, Y.K., Brown, S., Bilheimer, D.W., and Goldstein, J.L. (1976). Regulation of low density lipoprotein receptor activity in freshly isolated human lymphocytes. J. Clin. Invest. 58, 1465–1474.

56. Camus, M.C., Chapman, M.J., Forgez, P., and Laplaud, P.M. (1983). Distribution and characterization of the serum lipoproteins and apoproteins in the mouse, Mus musculus. J. Lipid Res. 24, 1210–1228.

57. Nishina, P.M., Wang, J., Toyofuku, W., Kuypers, F.A., Ishida, B.Y., and Paigen, B. (1993). Atherosclerosis and plasma and liver lipids in nine inbred strains of mice. Lipids 28, 599–605.

58. Paigen, B., Morrow, A., Brandon, C., Mitchell, D., and Holmes, P. (1985). Variation in susceptibility to atherosclerosis among inbred strains of mice. Atherosclerosis 57, 65–73.

6   References

1.   Raman CV, Krishnan KS. A new type of secondary radiation. Nature. 1928;121:501-502.

2.   Kann B, Offerhaus HL, Windbergs M, Otto C. Raman microscopy for cellular investigations - From single cell imaging to drug carrier uptake visualization. Adv Drug Deliv Rev. 2015.

3.   Placzek G, Lawrence Radiation L. The Rayleigh and Raman scattering. Livermore, Calif.: Livermore Radiation Laboratory, University of California; 1962.

4.   Matthäus C, Kale A, Chernenko T, Torchilin V, Diem M. New Ways of Imaging Uptake and Intracellular Fate of Liposomal Drug Carrier Systems inside Individual Cells, Based on Raman Microscopy. Mol Pharm. 2008;5(2):287-93.

5.   van Manen H-J, Lenferink A, Otto C. Noninvasive Imaging of Protein Metabolic Labeling in Single Human Cells Using Stable Isotopes and Raman Microscopy. Anal Chem. 2008;80(24):9576-82.

6.   Chernenko T, Sawant RR, Miljkovic M, Quintero L, Diem M, Torchilin V. Raman Microscopy for Noninvasive Imaging of Pharmaceutical Nanocarriers: Intracellular Distribution of Cationic Liposomes of Different Composition. Mol Pharm. 2012;9(4):930-6.

7.   Matthaus C, Krafft C, Dietzek B, Brehm BR, Lorkowski S, Popp J. Noninvasive imaging of intracellular lipid metabolism in macrophages by Raman microscopy in combination with stable isotopic labeling. Anal Chem. 2012;84(20):8549-56.

8.   Stiebing C, Matthaus C, Krafft C, Keller AA, Weber K, Lorkowski S, et al. Complexity of fatty acid distribution inside human macrophages on single cell level using Raman micro-spectroscopy. Anal Bioanal Chem. 2014;406(27):7037-46.

9.   Wang A, Haskin LA, Lane AL, Wdowiak TJ, Squyres SW, Wilson RJ, et al. Development of the Mars microbeam Raman spectrometer (MMRS). Journal of Geophysical Research: Planets. 2003;108(E1):n/a-n/a.

10.   Pelletier MJ. Quantitative analysis using Raman spectrometry. Appl Spectrosc. 2003;57(1):20A-42A.

11.   Kann B, Windbergs M. Chemical imaging of drug delivery systems with structured surfaces-a combined analytical approach of confocal raman microscopy and optical profilometry. The AAPS journal. 2013;15(2):505-10.

12.   Smith E, Dent G. Resonance Raman Scattering. Modern Raman Spectroscopy – A Practical Approach: John Wiley & Sons, Ltd; 2005. p. 93-112.

13.   Long DA. Vibrational Resonance Raman Scattering. The Raman Effect: John Wiley & Sons, Ltd; 2002. p. 221-70.

14.   Stiles PL, Dieringer JA, Shah NC, Van Duyne RP. Surface-enhanced Raman spectroscopy. Annual review of analytical chemistry (Palo Alto, Calif). 2008;1:601-26.

15.   Verma P. Tip-Enhanced Raman Spectroscopy: Technique and Recent Advances. Chem Rev. 2017;117(9):6447-66.

16.   Cheng J-X, Xie XS. Coherent Anti-Stokes Raman Scattering Microscopy: Instrumentation, Theory, and Applications. The Journal of Physical Chemistry B. 2004;108(3):827-40.

17.   Müller M, Zumbusch A. Coherent anti-Stokes Raman Scattering Microscopy. Chemphyschem. 2007;8(15):2156-70.

18.   Evans CL, Xie XS. Coherent anti-stokes Raman scattering microscopy: chemical imaging for biology and medicine. Annual review of analytical chemistry (Palo Alto, Calif). 2008;1:883-909.

19.   Chao-Yu Chung JB, Potma EO. Biomolecular Imaging with Coherent Nonlinear Vibrational Microscopy. Annu Rev Phys Chem. 2013;64(1):77-99.

20.   Zumbusch A, Langbein W, Borri P. Nonlinear vibrational microscopy applied to lipid biology. Prog Lipid Res. 2013;52(4):615-32.

21.   Evans CL, Potma EO, Puoris'haag M, Cote D, Lin CP, Xie XS. Chemical imaging of tissue in vivo with video-rate coherent anti-Stokes Raman scattering microscopy. Proc Natl Acad Sci U S A. 2005;102(46):16807-12.

22.   Lei M, Winterhalder M, Selm R, Zumbusch A. Video-rate wide-field coherent anti-Stokes Raman scattering microscopy with collinear nonphase-matching illumination. J Biomed Opt. 2011;16(2):021102.

23.   Saar BG, Freudiger CW, Reichman J, Stanley CM, Holtom GR, Xie XS. Video-Rate Molecular Imaging in Vivo with Stimulated Raman Scattering. Science. 2010;330(6009):1368-70.

24.   Burkacky O, Zumbusch A, Brackmann C, Enejder A. Dual-pump coherent anti-Stokes-Raman scattering microscopy. Opt Lett. 2006;31(24):3656-8.

25.   Müller M, Schins JM. Imaging the Thermodynamic State of Lipid Membranes with Multiplex CARS Microscopy. The Journal of Physical Chemistry B. 2002;106(14):3715-23.

26.   Cheng J-x, Volkmer A, Book LD, Xie XS. Multiplex Coherent Anti-Stokes Raman Scattering Microspectroscopy and Study of Lipid Vesicles. The Journal of Physical Chemistry B. 2002;106(34):8493-8.

27.   Selm R, Winterhalder M, Zumbusch A, Krauss G, Hanke T, Sell A, et al. Ultrabroadband background-free coherent anti-Stokes Raman scattering microscopy based on a compact Er:fiber laser system. Opt Lett. 2010;35(19):3282-4.

28.   Fu D, Lu F-K, Zhang X, Freudiger C, Pernik DR, Holtom G, et al. Quantitative Chemical Imaging with Multiplex Stimulated Raman Scattering Microscopy. J Am Chem Soc. 2012;134(8):3623-6.

29.   Nagayama M, Uchida T, Gohara K. Temporal and spatial variations of lipid droplets during adipocyte division and differentiation. J Lipid Res. 2007;48(1):9-18.

30.   Paudel A, Raijada D, Rantanen J. Raman spectroscopy in pharmaceutical product design. Adv Drug Deliv Rev. 2015.

31.   Lee AY, Erdemir D, Myerson AS. Crystal polymorphism in chemical process development. Annual review of chemical and biomolecular engineering. 2011;2:259-80.

32.   Chemburkar SR, Bauer J, Deming K, Spiwek H, Patel K, Morris J, et al. Dealing with the Impact of Ritonavir Polymorphs on the Late Stages of Bulk Drug Process Development. Organic Process Research & Development. 2000;4(5):413-7.

33.   Meyer MC, Straughn AB, Jarvi EJ, Wood GC, Pelsor FR, Shah VP. The bioinequivalence of carbamazepine tablets with a history of clinical failures. Pharm Res. 1992;9(12):1612-6.

34.   Pfund LY, Matzger AJ. Towards Exhaustive and Automated High-Throughput Screening for Crystalline Polymorphs. ACS Combinatorial Science. 2014;16(7):309-13.

35.   Láng P, Kiss V, Ambrus R, Farkas G, Szabó-Révész P, Aigner Z, et al. Polymorph screening of an active material. J Pharm Biomed Anal. 2013;84:177-83.

36.   Peterson ML, Morissette SL, McNulty C, Goldsweig A, Shaw P, LeQuesne M, et al. Iterative high-throughput polymorphism studies on acetaminophen and an experimentally derived structure for form III. J Am Chem Soc. 2002;124(37):10958-9.

37.   Hédoux A, Guinet Y, Descamps M. The contribution of Raman spectroscopy to the analysis of phase transformations in pharmaceutical compounds. Int J Pharm. 2011;417(1):17-31.

38.   Hedoux A, Guinet Y, Paccou L, Danede F, Derollez P. Polymorphic transformation of anhydrous caffeine upon grinding and hydrostatic pressurizing analyzed by low-frequency raman spectroscopy. J Pharm Sci. 2013;102(1):162-70.

39.   Sardo M, Amado AM, Ribeiro-Claro PJA. Pseudopolymorphic transitions of niclosamide monitored by Raman spectroscopy. J Raman Spectrosc. 2008;39(12):1915-24.

40.   Tian F, Zeitler JA, Strachan CJ, Saville DJ, Gordon KC, Rades T. Characterizing the conversion kinetics of carbamazepine polymorphs to the dihydrate in aqueous suspension using Raman spectroscopy. J Pharm Biomed Anal. 2006;40(2):271-80.

41.   Lee K-S, Kim K-J, Ulrich J. In Situ Monitoring of Cocrystallization of Salicylic Acid–4,4'-Dipyridyl in Solution Using Raman Spectroscopy. Crystal Growth & Design. 2014;14(6):2893-9.

42.   Rodríguez-Hornedo N, Nehm SJ, Seefeldt KF, Pagán-Torres Y, Falkiewicz CJ. Reaction Crystallization of Pharmaceutical Molecular Complexes. Mol Pharm. 2006;3(3):362-7.

43.   Sacré P-Y, Lebrun P, Chavez P-F, Bleye CD, Netchacovitch L, Rozet E, et al. A new criterion to assess distributional homogeneity in hyperspectral images of solid pharmaceutical dosage forms. Anal Chim Acta. 2014;818(Supplement C):7-14.

44.   Kuriyama A, Ozaki Y. Assessment of active pharmaceutical ingredient particle size in tablets by Raman chemical imaging validated using polystyrene microsphere size standards. AAPS PharmSciTech. 2014;15(2):375-87.

45.   Puncochova K, Vukosavljevic B, Hanus J, Beranek J, Windbergs M, Stepanek F. Non-invasive insight into the release mechanisms of a poorly soluble drug from amorphous solid dispersions by confocal Raman microscopy. Eur J Pharm Biopharm. 2016;101:119-25.

46.   Taylor LS, Langkilde FW, Zografi G. Fourier transform Raman spectroscopic study of the interaction of water vapor with amorphous polymers. J Pharm Sci. 2001;90(7):888-901.

47.   Scoutaris N, Alexander MR, Gellert PR, Roberts CJ. Inkjet printing as a novel medicine formulation technique. J Control Release. 2011;156(2):179-85.

48.   Beck RCR, Chaves PS, Goyanes A, Vukosavljevic B, Buanz A, Windbergs M, et al. 3D printed tablets loaded with polymeric nanocapsules: An innovative approach to produce customized drug delivery systems. Int J Pharm. 2017;528(1):268-79.

49.   Choi DH, Kim KH, Park JS, Jeong SH, Park K. Evaluation of drug delivery profiles in geometric three-layered tablets with various mechanical properties, in vitro–in vivo drug release, and Raman imaging. J Controlled Release. 2013;172(3):763-72.

50.   Vukosavljevic B, De Kinder L, Siepmann J, Muschert S, Windbergs M. Novel insights into controlled drug release from coated pellets by confocal Raman microscopy. J Raman Spectrosc. 2016;47(7):757-62.

51.   Fussell AL, Kleinebudde P, Herek J, Strachan CJ, Offerhaus HL. Coherent anti-Stokes Raman Scattering (CARS) Microscopy Visualizes Pharmaceutical Tablets During Dissolution. Journal of Visualized Experiments : JoVE. 2014(89):51847.

52.   Jurna M, Windbergs M, Strachan CJ, Hartsuiker L, Otto C, Kleinebudde P, et al. Coherent anti-Stokes Raman Scattering Microscopy to Monitor Drug Dissolution in Different Oral Pharmaceutical Tablets. Journal of Innovative Optical Health Sciences. 2009;02(01):37-43.

53.   Windbergs M, Jurna M, Offerhaus HL, Herek JL, Kleinebudde P, Strachan CJ. Chemical imaging of oral solid dosage forms and changes upon dissolution using coherent anti-Stokes Raman scattering microscopy. Anal Chem. 2009;81(6):2085-91.

54.   Belu A, Mahoney C, Wormuth K. Chemical imaging of drug eluting coatings: combining surface analysis and confocal Raman microscopy. J Control Release. 2008;126(2):111-21.

55.   Biggs KB, Balss KM, Maryanoff CA. Pore networks and polymer rearrangement on a drug-eluting stent as revealed by correlated confocal Raman and atomic force microscopy. Langmuir. 2012;28(21):8238-43.

56.   Wartewig S, Neubert RHH. Pharmaceutical applications of Mid-IR and Raman spectroscopy. Adv Drug Del Rev. 2005;57(8):1144-70.

57.   Breitkreitz MC, Sabin GP, Polla G, Poppi RJ. Characterization of semi-solid Self-Emulsifying Drug Delivery Systems (SEDDS) of atorvastatin calcium by Raman image spectroscopy and chemometrics. J Pharm Biomed Anal. 2013;73:3-12.

58.   Schaefer JJ, Ma C, Harris JM. Confocal Raman Microscopy Probing of Temperature-Controlled Release from Individual, Optically-Trapped Phospholipid Vesicles. Anal Chem. 2012;84(21):9505-12.

59.   Stillhart C, Imanidis G, Griffin BT, Kuentz M. Biopharmaceutical modeling of drug supersaturation during lipid-based formulation digestion considering an absorption sink. Pharm Res. 2014;31(12):3426-44.

60.   Schoenherr C, Haefele T, Paulus K, Francese G. Confocal Raman microscopy to probe content uniformity of a lipid based powder for inhalation: a quality by design approach. Eur J Pharm Sci. 2009;38(1):47-54.

61.   Wang H, Boraey MA, Williams L, Lechuga-Ballesteros D, Vehring R. Low-frequency shift dispersive Raman spectroscopy for the analysis of respirable dosage forms. Int J Pharm. 2014;469(1):197-205.

62.   Theophilus A, Moore A, Prime D, Rossomanno S, Whitcher B, Chrystyn H. Co-deposition of salmeterol and fluticasone propionate by a combination inhaler. Int J Pharm. 2006;313(1-2):14-22.

63.   Fussell AL, Grasmeijer F, Frijlink HW, de Boer AH, Offerhaus HL. CARS microscopy as a tool for studying the distribution of micronised drugs in adhesive mixtures for inhalation. J Raman Spectrosc. 2014;45(7):495-500.

64.   Rantanen J. Process analytical applications of Raman spectroscopy. J Pharm Pharmacol. 2007;59(2):171-7.

65.   Cornel J, Lindenberg C, Mazzotti M. Quantitative Application of in Situ ATR-FTIR and Raman Spectroscopy in Crystallization Processes. Ind Eng Chem Res. 2008;47(14):4870-82.

66.   Nagy ZK, Fevotte G, Kramer H, Simon LL. Recent advances in the monitoring, modelling and control of crystallization systems. Chem Eng Res Des. 2013;91(10):1903-22.

67.   Pataki H, Csontos I, Nagy ZK, Vajna B, Molnar M, Katona L, et al. Implementation of Raman Signal Feedback to Perform Controlled Crystallization of Carvedilol. Organic Process Research & Development. 2013;17(3):493-9.

68.   Li Y-T, Qu L-L, Li D-W, Song Q-X, Fathi F, Long Y-T. Rapid and sensitive in-situ detection of polar antibiotics in water using a disposable Ag–graphene sensor based on electrophoretic preconcentration and surface-enhanced Raman spectroscopy. Biosensors Bioelectron. 2013;43(Supplement C):94-100.

69.   Clarke SJ, Littleford RE, Smith WE, Goodacre R. Rapid monitoring of antibiotics using Raman and surface enhanced Raman spectroscopy. Analyst. 2005;130(7):1019-26.

70.   De Beer T, Burggraeve A, Fonteyne M, Saerens L, Remon JP, Vervaet C. Near infrared and Raman spectroscopy for the in-process monitoring of pharmaceutical production processes. Int J Pharm. 2011;417(1-2):32-47.

71.   De Beer TRM, Bodson C, Dejaegher B, Walczak B, Vercruysse P, Burggraeve A, et al. Raman spectroscopy as a process analytical technology (PAT) tool for the in-line monitoring and understanding of a powder blending process. J Pharm Biomed Anal. 2008;48(3):772-9.

72.   Poutiainen S, Pajander J, Savolainen A, Ketolainen J, Jarvinen K. Evolution of granule structure and drug content during fluidized bed granulation by X-ray microtomography and confocal Raman spectroscopy. J Pharm Sci. 2011;100(12):5254-69.

73.   Wikström H, Marsac PJ, Taylor LS. In-line monitoring of hydrate formation during wet granulation using Raman spectroscopy. J Pharm Sci. 2005;94(1):209-19.

74.   Knop K, Kleinebudde P. PAT-tools for process control in pharmaceutical film coating applications. Int J Pharm. 2013;457(2):527-36.

75.   Wirges M, Funke A, Serno P, Knop K, Kleinebudde P. Development and in-line validation of a Process Analytical Technology to facilitate the scale up of coating processes. J Pharm Biomed Anal. 2013;78-79:57-64.

76.   Bogomolov A, Engler M, Melichar M, Wigmore A. In-line analysis of a fluid bed pellet coating process using a combination of near infrared and Raman spectroscopy. J Chemometrics. 2010;24(7-8):544-57.

77.   Saerens L, Dierickx L, Lenain B, Vervaet C, Remon JP, De Beer T. Raman spectroscopy for the in-line polymer-drug quantification and solid state characterization during a pharmaceutical hot-melt extrusion process. Eur J Pharm Biopharm. 2011;77(1):158-63.

78.   Saerens L, Ghanam D, Raemdonck C, Francois K, Manz J, Krüger R, et al. In-line solid state prediction during pharmaceutical hot-melt extrusion in a 12mm twin screw extruder using Raman spectroscopy. Eur J Pharm Biopharm. 2014;87(3):606-15.

79.   Hedoux A, Paccou L, Achir S, Guinet Y. In situ monitoring of proteins during lyophilization using micro-Raman spectroscopy: a description of structural changes induced by dehydration. J Pharm Sci. 2012;101(7):2316-26.

80.   de Waard H, De Beer T, Hinrichs WL, Vervaet C, Remon JP, Frijlink HW. Controlled crystallization of the lipophilic drug fenofibrate during freeze-drying: elucidation of the mechanism by in-line Raman spectroscopy. The AAPS journal. 2010;12(4):569-75.

81.   De Beer TRM, Allesø M, Goethals F, Coppens A, Vander Heyden Y, Lopez De Diego H, et al. Implementation of a Process Analytical Technology System in a Freeze-Drying Process Using Raman Spectroscopy for In-Line Process Monitoring. Anal Chem. 2007;79(21):7992-8003.

82.   de Veij M, Vandenabeele P, De Beer T, Remon JP, Moens L. Reference database of Raman spectra of pharmaceutical excipients. J Raman Spectrosc. 2009;40(3):297-307.

83.   Wikstrom H, Romero-Torres S, Wongweragiat S, Williams JA, Grant ER, Taylor LS. On-line content uniformity determination of tablets using low-resolution Raman spectroscopy. Appl Spectrosc. 2006;60(6):672-81.

84.   Burley JC, Alkhalil A, Bloomfield M, Matousek P. Transmission Raman spectroscopy for quality control in model cocrystal tablets. Analyst. 2012;137(13):3052-7.

85.   De Bleye C, Sacré PY, Dumont E, Netchacovitch L, Chavez PF, Piel G, et al. Development of a quantitative approach using surface-enhanced Raman chemical imaging: First step for the determination of an impurity in a pharmaceutical model. J Pharm Biomed Anal. 2014;90(Supplement C):111-8.

86.   Ricci C, Nyadong L, Yang F, Fernandez FM, Brown CD, Newton PN, et al. Assessment of hand-held Raman instrumentation for in situ screening for potentially counterfeit artesunate antimalarial tablets by FT-Raman spectroscopy and direct ionization mass spectrometry. Anal Chim Acta. 2008;623(2):178-86.

87.   Bloomfield M, Andrews D, Loeffen P, Tombling C, York T, Matousek P. Non-invasive identification of incoming raw pharmaceutical materials using Spatially Offset Raman Spectroscopy. J Pharm Biomed Anal. 2013;76(Supplement C):65-9.

88.   Kogermann K, Aaltonen J, Strachan CJ, Pollanen K, Heinamaki J, Yliruusi J, et al. Establishing quantitative in-line analysis of multiple solid-state transformations during dehydration. J Pharm Sci. 2008;97(11):4983-99.

89.   Greco K, Bergman TL, Bogner R. Design and characterization of a laminar flow-through dissolution apparatus: Comparison of hydrodynamic conditions to those of common dissolution techniques. Pharm Dev Technol. 2011;16(1):75-87.

90.   Windbergs M, Haaser M, McGoverin CM, Gordon KC, Kleinebudde P, Strachan CJ. Investigating the relationship between drug distribution in solid lipid matrices and dissolution behaviour using Raman spectroscopy and mapping. J Pharm Sci. 2010;99(3):1464-75.

91.   Windbergs M, Jurna M, Offerhaus HL, Herek JL, Kleinebudde P, Strachan CJ. Chemical Imaging of Oral Solid Dosage Forms and Changes upon Dissolution Using Coherent Anti-Stokes Raman Scattering Microscopy. Anal Chem. 2009;81(6):2085-91.

92.   Huser T, Chan J. Raman spectroscopy for physiological investigations of tissues and cells. Adv Drug Del Rev. 2015;89:57-70.

93.   Puppels GJ, de Mul FF, Otto C, Greve J, Robert-Nicoud M, Arndt-Jovin DJ, et al. Studying single living cells and chromosomes by confocal Raman microspectroscopy. Nature. 1990;347(6290):301-3.

94.   Schie IW, Huser T. Label-free analysis of cellular biochemistry by Raman spectroscopy and microscopy. Comprehensive Physiology. 2013;3(2):941-56.

95.   Chan JW, Taylor DS, Zwerdling T, Lane SM, Ihara K, Huser T. Micro-Raman Spectroscopy Detects Individual Neoplastic and Normal Hematopoietic Cells. Biophys J. 2006;90(2):648-56.

96.   Neugebauer U, Clement JH, Bocklitz T, Krafft C, Popp J. Identification and differentiation of single cells from peripheral blood by Raman spectroscopic imaging. Journal of biophotonics. 2010;3(8-9):579-87.

97.   Notingher I, Bisson I, Bishop AE, Randle WL, Polak JMP, Hench LL. In Situ Spectral Monitoring of mRNA Translation in Embryonic Stem Cells during Differentiation in Vitro. Anal Chem. 2004;76(11):3185-93.

98.   Chan JW, Lieu DK, Huser T, Li RA. Label-free separation of human embryonic stem cells and their cardiac derivatives using Raman spectroscopy. Anal Chem. 2009;81(4):1324-31.

99.   Dochow S, Krafft C, Neugebauer U, Bocklitz T, Henkel T, Mayer G, et al. Tumour cell identification by means of Raman spectroscopy in combination with optical traps and microfluidic environments. Lab on a chip. 2011;11(8):1484-90.

100.   Dochow S, Beleites C, Henkel T, Mayer G, Albert J, Clement J, et al. Quartz microfluidic chip for tumour cell identification by Raman spectroscopy in combination with optical traps. Anal Bioanal Chem. 2013;405(8):2743-6.

101.   Huser T, Orme CA, Hollars CW, Corzett MH, Balhorn R. Raman spectroscopy of DNA packaging in individual human sperm cells distinguishes normal from abnormal cells. Journal of biophotonics. 2009;2(5):322-32.

102.   Wood BR, Hammer L, Davis L, McNaughton D. Raman microspectroscopy and imaging provides insights into heme aggregation and denaturation within human erythrocytes. J Biomed Opt. 2005;10(1):14005.

103.   Wood BR, Caspers P, Puppels GJ, Pandiancherri S, McNaughton D. Resonance Raman spectroscopy of red blood cells using near-infrared laser excitation. Anal Bioanal Chem. 2007;387(5):1691-703.

104.   Liu R, Mao Z, Matthews DL, Li CS, Chan JW, Satake N. Novel single-cell functional analysis of red blood cells using laser tweezers Raman spectroscopy: application for sickle cell disease. Exp Hematol. 2013;41(7):656-61 e1.

105.   Peng L, Wang G, Liao W, Yao H, Huang S, Li YQ. Intracellular ethanol accumulation in yeast cells during aerobic fermentation: a Raman spectroscopic exploration. Lett Appl Microbiol. 2010;51(6):632-8.

106.   Yamakoshi H, Dodo K, Okada M, Ando J, Palonpon A, Fujita K, et al. Imaging of EdU, an Alkyne-Tagged Cell Proliferation Probe, by Raman Microscopy. J Am Chem Soc. 2011;133(16):6102-5.

107.   Yamakoshi H, Dodo K, Palonpon A, Ando J, Fujita K, Kawata S, et al. Alkyne-Tag Raman Imaging for Visualization of Mobile Small Molecules in Live Cells. J Am Chem Soc. 2012;134(51):20681-9.

108.   Cooper MA. Non-optical screening platforms: the next wave in label-free screening? Drug Discov Today. 2006;11(23):1068-74.

109.   Xi B, Yu N, Wang X, Xu X, Abassi YA. The application of cell-based label-free technology in drug discovery. Biotechnology journal. 2008;3(4):484-95.

110.   Saha A, Yakovlev VV. Towards a rational drug design: Raman micro-spectroscopy analysis of prostate cancer cells treated with an aqueous extract of Nerium Oleander. J Raman Spectrosc. 2009;40(11):1459-60.

111.   Yao H, Tao Z, Ai M, Peng L, Wang G, He B, et al. Raman spectroscopic analysis of apoptosis of single human gastric cancer cells. Vib Spectrosc. 2009;50(2):193-7.

112.   Owen CA, Selvakumaran J, Notingher I, Jell G, Hench LL, Stevens MM. In vitro toxicology evaluation of pharmaceuticals using Raman micro-spectroscopy. J Cell Biochem. 2006;99(1):178-86.

113.   Zoladek A, Pascut FC, Patel P, Notingher I. Non-invasive time-course imaging of apoptotic cells by confocal Raman micro-spectroscopy. J Raman Spectrosc. 2011;42(3):251-8.

114.   Nawaz H, Bonnier F, Meade AD, Lyng FM, Byrne HJ. Comparison of subcellular responses for the evaluation and prediction of the chemotherapeutic response to cisplatin in lung adenocarcinoma using Raman spectroscopy. Analyst. 2011;136(12):2450-63.

115.   Davis BM, Hemphill AJ, Cebeci Maltaş D, Zipper MA, Wang P, Ben-Amotz D. Multivariate Hyperspectral Raman Imaging Using Compressive Detection. Anal Chem. 2011;83(13):5086-92.

116.   Smith ZJ, Strombom S, Wachsmann-Hogiu S. Multivariate optical computing using a digital micromirror device for fluorescence and Raman spectroscopy. Opt Express. 2011;19(18):16950-62.

117.   Zhang D, Wang P, Slipchenko MN, Ben-Amotz D, Weiner AM, Cheng J-X. Quantitative Vibrational Imaging by Hyperspectral Stimulated Raman Scattering Microscopy and Multivariate Curve Resolution Analysis. Anal Chem. 2013;85(1):98-106.

118.   Chernenko T, Sawant RR, Miljkovic M, Quintero L, Diem M, Torchilin V. Raman microscopy for noninvasive imaging of pharmaceutical nanocarriers: intracellular distribution of cationic liposomes of different composition. Mol Pharm. 2012;9(4):930-6.

119.   Dorney J, Bonnier F, Garcia A, Casey A, Chambers G, Byrne HJ. Identifying and localizing intracellular nanoparticles using Raman spectroscopy. Analyst. 2012;137(5):1111-9.

120.   Sobot D, Mura S, Rouquette M, Vukosavljevic B, Cayre F, Buchy E, et al. Circulating Lipoproteins: A Trojan Horse Guiding Squalenoylated Drugs to LDL-Accumulating Cancer Cells. Mol Ther.25(7):1596-605.

121.   Chan JW, Esposito AP, Talley CE, Hollars CW, Lane SM, Huser T. Reagentless identification of single bacterial spores in aqueous solution by confocal laser tweezers Raman spectroscopy. Anal Chem. 2004;76(3):599-603.

122.   Kong L, Zhang P, Setlow P, Li Y-q. Characterization of Bacterial Spore Germination Using Integrated Phase Contrast Microscopy, Raman Spectroscopy, and Optical Tweezers. Anal Chem. 2010;82(9):3840-7.

123.   Zhang P, Garner W, Yi X, Yu J, Li YQ, Setlow P. Factors affecting variability in time between addition of nutrient germinants and rapid dipicolinic acid release during germination of spores of Bacillus species. J Bacteriol. 2010;192(14):3608-19.

124.   Maquelin K, Choo-Smith L-Pi, van Vreeswijk T, Endtz HP, Smith B, Bennett R, et al. Raman Spectroscopic Method for Identification of Clinically Relevant Microorganisms Growing on Solid Culture Medium. Anal Chem. 2000;72(1):12-9.

125.   Willemse-Erix DF, Scholtes-Timmerman MJ, Jachtenberg JW, van Leeuwen WB, Horst-Kreft D, Bakker Schut TC, et al. Optical fingerprinting in bacterial epidemiology: Raman spectroscopy as a real-time typing method. J Clin Microbiol. 2009;47(3):652-9.

126.   Chan JW, Winhold H, Corzett MH, Ulloa JM, Cosman M, Balhorn R, et al. Monitoring dynamic protein expression in living E. coli. Bacterial cells by laser tweezers Raman spectroscopy. Cytometry Part A : the journal of the International Society for Analytical Cytology. 2007;71(7):468-74.

127.   Munchberg U, Rosch P, Bauer M, Popp J. Raman spectroscopic identification of single bacterial cells under antibiotic influence. Anal Bioanal Chem. 2014;406(13):3041-50.

128.   Moritz TJ, Polage CR, Taylor DS, Krol DM, Lane SM, Chan JW. Evaluation of Escherichia coli cell response to antibiotic treatment by use of Raman spectroscopy with laser tweezers. J Clin Microbiol. 2010;48(11):4287-90.

129.   Smith GP, McGoverin CM, Fraser SJ, Gordon KC. Raman imaging of drug delivery systems. Adv Drug Deliv Rev. 2015.

130.   Breitenbach J, Schrof W, Neumann J. Confocal Raman-Spectroscopy: Analytical Approach to Solid Dispersions and Mapping of Drugs. Pharm Res. 1999;16(7):1109-13.

131.   Vajna B, Pataki H, Nagy Z, Farkas I, Marosi G. Characterization of melt extruded and conventional Isoptin formulations using Raman chemical imaging and chemometrics. Int J Pharm. 2011;419(1–2):107-13.

132.   Nagy ZK, Balogh A, Vajna B, Farkas A, Patyi G, Kramarics A, et al. Comparison of electrospun and extruded soluplus®-based solid dosage forms of improved dissolution. J Pharm Sci. 2012;101(1):322-32.

133.   Tres F, Treacher K, Booth J, Hughes LP, Wren SAC, Aylott JW, et al. Real time Raman imaging to understand dissolution performance of amorphous solid dispersions. J Controlled Release. 2014;188:53-60.

134.   Balss KM, Long FH, Veselov V, Orana A, Akerman-Revis E, Papandreou G, et al. Multivariate Analysis Applied to the Study of Spatial Distributions Found in Drug-Eluting Stent Coatings by Confocal Raman Microscopy. Anal Chem. 2008;80(13):4853-9.

135.   Dong J, Foley JD, Frethem CD, Hoerr RA, Matuszewski MJ, Puskas JE, et al. Multimodal Dynamic Imaging of Therapeutic Biomedical Coatings in Aqueous Medium. Langmuir. 2009;25(10):5442-5.

136.   Biggs KB, Balss KM, Maryanoff CA. Pore Networks and Polymer Rearrangement on a Drug-Eluting Stent as Revealed by Correlated Confocal Raman and Atomic Force Microscopy. Langmuir. 2012;28(21):8238-43.

137.   Doub W, Adams W, Spencer J, Buhse L, Nelson M, Treado P. Raman Chemical Imaging for Ingredient-specific Particle Size Characterization of Aqueous Suspension Nasal Spray Formulations: A Progress Report. Pharm Res. 2007;24(5):934-45.

138.   Widjaja E, Lee WL, Loo SCJ. Application of Raman Microscopy to Biodegradable Double-Walled Microspheres. Anal Chem. 2010;82(4):1277-82.

139.   Rizi K, Green RJ, Khutoryanskaya O, Donaldson M, Williams AC. Mechanisms of burst release from pH-responsive polymeric microparticles. J Pharm Pharmacol. 2011;63(9):1141-55.

140. Henson MJ, Zhang L. Drug Characterization in Low Dosage Pharmaceutical Tablets Using Raman Microscopic Mapping. Appl Spectrosc. 2006;60(11):1247-55.

141. Slobodan. An In-Depth Analysis of Raman and Near-Infrared Chemical Images of Common Pharmaceutical Tablets. Appl Spectrosc. 2007;61(3):239-50.

142. Slipchenko MN, Chen H, Ely DR, Jung Y, Carvajal MT, Cheng JX. Vibrational imaging of tablets by epi-detected stimulated Raman scattering microscopy. Analyst. 2010;135(10):2613-9.

143. Planz V, Seif S, Atchison JS, Vukosavljevic B, Sparenberg L, Kroner E, et al. Three-dimensional hierarchical cultivation of human skin cells on bio-adaptive hybrid fibers. Integr Biol (Camb). 2016;8(7):775-84.

144. Nordgård CT, Nonstad U, Olderøy MØ, Espevik T, Draget KI. Alterations in Mucus Barrier Function and Matrix Structure Induced by Guluronate Oligomers. Biomacromolecules. 2014;15(6):2294-300.

145. Daum N, Kuehn A, Hein S, Schaefer UF, Huwer H, Lehr CM. Isolation, cultivation, and application of human alveolar epithelial cells. Methods Mol Biol. 2012;806:31-42.

146. Perez-Gil J, Weaver TE. Pulmonary surfactant pathophysiology: current models and open questions. Physiology (Bethesda). 2010;25(3):132-41.

147. Vukosavljevic B, Murgia X, Schwarzkopf K, Schaefer UF, Lehr C-M, Windbergs M. Tracing molecular and structural changes upon mucolysis with N-acetyl cysteine in human airway mucus. Int J Pharm.

148. Couvreur P, Stella B, Reddy LH, Hillaireau H, Dubernet C, Desmaële D, et al. Squalenoyl Nanomedicines as Potential Therapeutics. Nano Lett. 2006;6(11):2544-8.

149. Sobot D, Mura S, Yesylevskyy SO, Dalbin L, Cayre F, Bort G, et al. Conjugation of squalene to gemcitabine as unique approach exploiting endogenous lipoproteins for drug delivery. 2017;8:15678.

150. Buchy E, Vukosavljevic B, Windbergs M, Sobot D, Dejean C, Mura S, et al. Synthesis of a deuterated probe for the confocal Raman microscopy imaging of squalenoyl nanomedicines. Beilstein Journal of Organic Chemistry. 2016;12:1127-35.

7 List of Scientific Publications

Articles published in international peer-reviewed journals:

B. Vukosavljevic, L. De Kinder, J. Siepmann, S. Muschert, M. Windbergs; Novel insights into controlled drug release from coated pellets by confocal Raman microscopy. *J. Raman Spectrosc.* 2016, 47:757-762.

K. Puncochova*, **B. Vukosavljevic***, J. Hanus, J. Beranek, M. Windbergs, F. Stepanek; Non-invasive insight into the release mechanisms of a poorly soluble drug from amorphous solid dispersions by confocal Raman microscopy. *Eur. J. Pharm. Biopharm.* 2016, 101:119-25.
* These authors contributed equally to this work.

V. Planz, S. Seif, J.C. Atchison, **B. Vukosavljevic**, L. Sparenberg, E. Kroner, M. Windbergs; Three-dimensional hierarchical cultivation of human skin cells on bio-adaptive hybrid fibers. *Integr. Biol*. 2016, 8(7):775-84.

E. Buchy, **B. Vukosavljevic**, M. Windbergs, D. Sobot, C. Dejean, S. Mura, P. Couvreur, D. Desmaele; Synthesis of a deuterated probe for the confocal Raman microscopy imaging of squalenoyl nanomedicines. *Beilstein J. Org. Chem.* 2016, 12:1127-1135.

F. Graef, **B. Vukosavljevic**, J.P Michael, M. Wirth, O. Ries, C. De Rossi, M. Windbergs, V. Rosilio, C. Ducho, S. Gordon, C.M. Lehr; The bacterial cell envelope as delimiter of anti-infective bioavailability – An in vitro permeation model of the Gram-negative bacterial inner membrane. *J. Contol. Release* 2016; 243:214-224.

D. Sobot, S. Mura, M. Rouquette, **B. Vukosavljevic**, F. Cayre, E. Buchy, G. Pieters, M. Windbergs, D. Desmaele, P. Couvreur; Circulating lipoprotein: a Trojan horse guiding squalenoylated drugs to LDL-accumulating cancer cells. *Mol. Ther.* 2017; 25(7):1596-1605.

R.C.R. Beck, P.S. Chaves, A. Goyanes, **B. Vukosavljevic**, A. Buanz, M. Windbergs, A.W. Basit, S. Gaisford; 3D printed tablets loaded with polymeric nanocapsules: An innovative approach to produce customized drug delivery systems. *Int. J. Pharm.* 2017; 528: 268-279.

B. Vukosavljevic*, X. Murgia*, K. Schwarzkopf, U.F. Schaefer, C.M. Lehr, M. Windbergs; Tracing molecular and structural changes upon mucolysis with N-acetyl cysteine in human airway mucus. *Int. J. Pharm.* 2017, 533: 373–376.
* These authors contributed equally to this work.

D. F. de Andrade, **B. Vukosavljevic**, E. V. Benvenutti, A. R. Pohlmann, S.S. Guterres, M. Windbergs, R. Beck; Redispersible spray-dried lipid-core nanocapsules intended for oral delivery: the influence of the particle number on redispersibility. Pharm. Develop Tech. 2017, DOI:10.1080/10837450.2017.1400559.

B. Vukosavljevic, M. Hittinger, H. Hachmeister, C. Pilger, X. Murgia, M. Gepp, L. Gentile, H. Huwer, N. Schneider-Daum, T. Huser, C.M. Lehr, M. Windbergs. Vibrational spectroscopic imaging and live cell video microscopy for studying differentiation of primary human alveolar epithelial cells, in reply.

8 Acknowledgments

I would like to thank many great people who taught, helped and supported me in the last few years! The list is long, as the way to the end was challenging, so I would like to mention a few people in person.

First of all, my supervisors.

I owe a special gratitude to Prof. Maike Windbergs, person who I learned a lot from, put my best forward and enabled me to finalize this piece of work. Your enthusiasm when I arrive to your office with another (maybe silly) idea kept my motivation and after many abstracts, papers, posters and presentations, I realized a decrease in the amount of red color after your corrections. This proves you did a great job.

Thank you, Prof. Claus-Michael Lehr, for supporting and welcoming me in your research group. HIPS was a great environment for me combining excellent working conditions and fun, and I was always happy to come to the lab.

Special thanks I owe to my group colleagues. Lutz and Birthe for accepting me in the team and teaching me about Raman; Salem, Viktoria, Jing and Nathalie for all the scientific help and great time while growing up together.

My brothers, Xabi and Khiet deserve a special line. You made my time in Saarbrucken, far away from home, and I am very grateful for meeting you. I hope for many more "Canosa" times to come! Next to them, many thanks to the whole DDEL group, old and new PhD students, as well as Sarah, Karin, Petra, Chiara and Jana.

I am also very grateful to the German Academic Exchange Service (DAAD) who enabled me to pay a research visit to Prof. Lohninger and his team at TU Vienna. I learned a lot and had a great time with you! Special thanks I owe to Prof. Huser, Christian and Henning for warmly welcoming me to the Institute of Biomolecular Photonics in Bielefeld and introducing me the CARS. Many thanks to all the other collaboration partners and friends.

I would like to thank Prof. Jung for reviewing my thesis and all my graduation committee members for their willingness to accompany me throughout this final step of my PhD time.

Last but not least, I would not have come this far without the unreserved support and encouragement of my family and girlfriend.

Мама, Мина, бака Братислава и бака Славка, моје дивне даме, можете се осећати главним ауторима овог малог рада, а ја најсрећнијим сином, братом и унуком, јер без ваше подршке не бих ово изгурао. Тата, знам да си ту иако ниси, и да си поносан. Хвала Вам није довољно рећи!

Piccina mia, Ghent must be the luckiest city and me the luckiest man in the world. Thank you for endless support, scientific discussions, love and hugs. We can move things together. One thesis - checked, one more to go. Grazie di tutto!

Thank you all! Хвала свима!